A NOVEL POWDER METALLURGY TECHNIQUE FOR PRODUCING ARTIFICIAL PINNING CENTERS IN Nb-Ti SUPERCONDUCTORS

by

PAUL D. JABLONSKI

A thesis submitted in partial fulfillment of the
requirements for the degree of

Doctor of Philosophy
(Metallurgical Engineering)

at the
UNIVERSITY OF WISCONSIN-MADISON
1994

A NOVEL POWDER METALLURGY TECHNIQUE FOR PRODUCING ARTIFICIAL PINNING CENTERS IN Nb-Ti SUPERCONDUCTORS

Paul D. Jablonski

Under the supervision of Professor David C. Larbalestier

at the University of Wisconsin-Madison

This thesis demonstrates a novel powder metallurgy process which avoids the thermodynamic and kinetic phase limitations of conventional Nb-Ti superconductors by employing mixtures of powder metals to produce a two phase microstructure of greater second phase fraction than can be obtained by conventional processing. The originality of the process has been recognized by the award of a U.S. Patent (5,226,947). A major advantage of this invention is that it permits nanometer-scale structures with a small strain process (strains of about 13 are required to reach peak critical current density). This thesis reports on conductors of Nb-55 weight percent Ti containing 0-40 volume percent Nb second phase, roughly double what is obtainable in conventional Nb-47 weight percent Ti. A detailed microstructural characterization was performed on these conductors. The critical current density at five tesla was found to optimize when the Nb ribbons were 14-30 nanometers in thickness. The critical current densities were greatly enhanced at low fields, for exam-

ple, the critical current density at one tesla increases to over 15,000 amps per millimeter squared with the addition of 40 volume percent Nb second phase. The high field critical current density shows smaller enhancements.

Acknowledgements

I would like to thank my advisor, Prof. David Larbalestier, for all his help and guidance throughout the years, but especially for having put his trust in me. I would also like to thank all of David's former students, who have contributed to the development of the group in terms of techniques, equipment and knowledge. I am eternally grateful to Dr. Peter Lee for the TEM on the conductors in this thesis. Having done a small amount of TEM myself, I can truthfully report that Peter is a miracle worker. Thanks is also due to Bill Starch for maintaining the fabrication shop that I spent most of my time in, and to Lloyd Lincoln for putting up with all my urgent requests for extrusion cans. Alex Squitieri has done an excellent job in maintaining the J_c rack during my years in the group such that I could essentially walk up and use it any time and not have to worry whether or not it would work.

Over the years I have benefited from many discussions and interactions with other members of the group including Jim McKinnell, Tom Willis, Lance Cooley, Rob Heussner, Alex Gurevich, and George Stejic. I was also lucky to be able to work with some very bright undergraduates including Craig Christopherson, Jon Ponty, David Ohman and Jesse Marquardt.

This thesis would likely have been very different if David had not decided to purchase the hydrostatic extrusion press. This showed a tremendous amount of trust in me and for this I will be eternally grateful. I would like to thank Frank Fox, the manufacturer of the extrusion press; he was always willing to give advice on how I might improve my extrusion process. I would like to thank Peter Roberts and Ina Donahue of Nuclear Metals for donating the Nb-55wt%Ti powder used for matrix material for this thesis. I would also like to thank Barry Gray of Amray for the FESEM work. And thanks to David Smathers for the interstitial chemistry analysis on the final composites.

Finally, I would like to thank my family for all their support over the years. I would especially like to thank my father, Joe Jablonski, for giving me the very best gift a father could: at a very young age, my father told me that I could be anything I wanted to be. Most of all I would like to thank my wife Jean for all her love and understanding through the past years.

Contents

List of Figures

List of Tables

Chapter 1

Developing High Critical Current Densities in Nb-Ti Based Alloys

1.1 Conventional Nb-Ti: Current State of the Art

Niobium-Titanium alloys remain the most widely used superconductors. Applications range from small laboratory magnets (bore ~50mm, length ~250mm), to MRI magnets (bore ~1m, length ~2.5m), to large high energy physics magnets (bore ~50mm, length ~20m) used for particle accelerators. This leadership position continues in spite of the existence of many alternative materials with higher critical temperature (T_c) and upper critical field (B_{c_2}), such as the A-15 compounds (chiefly Nb_3Sn) and more recently the high T_c cuprate superconductors (chiefly the Bi-Sr-Ca-Cu-O compounds). The main reason for the wide use of Nb-Ti is its relative ease of fabrication and use, and its technologically useful T_c, B_{c_2} and J_c (critical current density).

1.1.1 Regarding Superconductivity

The superconducting phase transition can be defined by a critical temperature and field (T_c and H_c). There are two categories of superconductors which are known as Type I (e.g., Pb) and Type II (e.g., Nb, Nb-Ti, and Pb alloys). Type I superconductors are characterized by the complete expulsion of magnetic flux except for a thin layer at the surface over which the field decays over the length of the penetration depth λ [71]. At low fields, Type II superconductors behave as Type I superconductors expelling the external flux. However, at some intermediate field, H_{c_1}, flux enters the sample in the form of fluxons, thus creating a new, two-phase normal and superconducting state (the so-called mixed state). While a Type I superconductor can only carry supercurrent on the surface, a Type II superconductor in the mixed state carries supercurrents throughout the bulk; thus, much higher overall current densities may be achieved.

The transition temperature and the upper critical field are essentially set by the alloy composition, while J_c is established by the interaction of fluxons with the microstructure. Fluxons can be viewed as small tubes of magnetic flux from which the superconducting matrix is shielded by a circulating supercurrent which decays over the length λ. Thus their structure is vortex-like. The flux in the normal core is quantized in units $\phi_o = 2.07 \times 10^{-15} Wb$. The fluxon core radius is that of the interaction distance between Cooper electron pairs: the coherence length ξ. Fluxons repel each other, thereby establishing a field-dependent triangular flux line lattice (FLL) characterized by a lattice parameter ($a_o = 1.07\sqrt{\phi/B}$). Typically a few nanometers in diameter, their size scales with temperature ($\xi \propto 1/(1-t)^{0.5}$, $t = T/T_c$) and their number density scales with field. Since the separation of vortices is $<< \lambda$ at fields much above H_{c_1}, the field is only partially expelled from the mixed state of a Type II superconductor.

Because the core of the fluxon is normal (i.e., not superconducting), the system energy can be lowered if a fluxon core occupies a normal or poorly superconducting region. Thus to create a superconductor capable of large current densities, it is advantageous to form a two phase microstructure consisting of a continuous superconducting matrix in which discrete normal phases are dispersed. In conventional Nb-Ti this normal second phase is α-Ti. It is formed during a precipitation heat treatment and is then deformed into nanometer thick ribbons by wire drawing.

In Type II superconductors, the appearance of a voltage is generally not an indication that the sample has gone normal; rather it is the result of the movement of fluxons under the influence of the Lorentz force ($\mathbf{F}_L = \mathbf{J} \times \mathbf{B}$). When a fluxon moves, the $\dot{B}$ creates an electric field. The self heating produced by the dissipation may ultimately destroy the supercurrents. Hence flux pinning by material inhomogeneities is crucial to developing a high critical current density.

1.1.2 Optimizing Conventional Nb-Ti

As one might imagine, the development of a "conventional" high critical current density Nb-Ti conductor [93, 120, 118] is a complex process (Figures 1.1 and 1.2). It has been found[64] that heat treatment is best deferred until a true strain[a] of about 5. At smaller strains the microstructure consists of dislocation tangles and subgrains; thus intergranular precipitation of Widmanstätten α-Ti is favored[80]. These precipitates harden the alloy considerably, making further wire drawing difficult, if not impossible. Once

---

[a] True strain is defined as $\epsilon = ln(A_i/A_f)$ where the A's refer to the initial and final areas, respectively. Strain and true strain will be used interchangeably in this document.

a cold work strain of 4-6 has been put into the alloy, the dislocation subgrain structure develops into high angle grain boundaries and intergranular defects such as dislocation tangles are minimized. During the initial stages of the first heat treatment a thin (~1nm) film of α -Ti precipitates on the grain boundaries, typically with very little incubation time (e.g., 3h/300°C, Figures 1.2 and 1.3). After 30-50 hours the α -Ti breaks out of the grain boundaries, producing approximately equiaxed (in transverse cross-section) precipitates which are 100-300nm in diameter and some 3-5 times longer (Figures 1.2 and 1.3). The first heat treatment produces ~5-10 vol% α -Ti; generally three heat treatments are used, and these produce about 20vol% second phase needed for high J_c. These heat treatments are generally 40-80h at 375-420°C. They are separated by a cold drawing strain of about one which serves to produce a new grain structure into which fresh precipitate can be nucleated. A strain of about 5-7 is required after the final heat treatment in order to refine the α -Ti precipitates into 1-2nm thick ribbons which typify an optimized microstructure[61] (Figures 1.2 and 1.3). Thus a total strain of about 12 is required to fully develop a high current density conductor (Figure 1.1).

Commercial Nb-Ti alloys typically lie in the range of 44-50wt% Ti which bounds the peak in B_{c_2} (about 11T). Most attempts to optimize this alloy have been made near the Nb-46.5wt%Ti composition. While alloys which

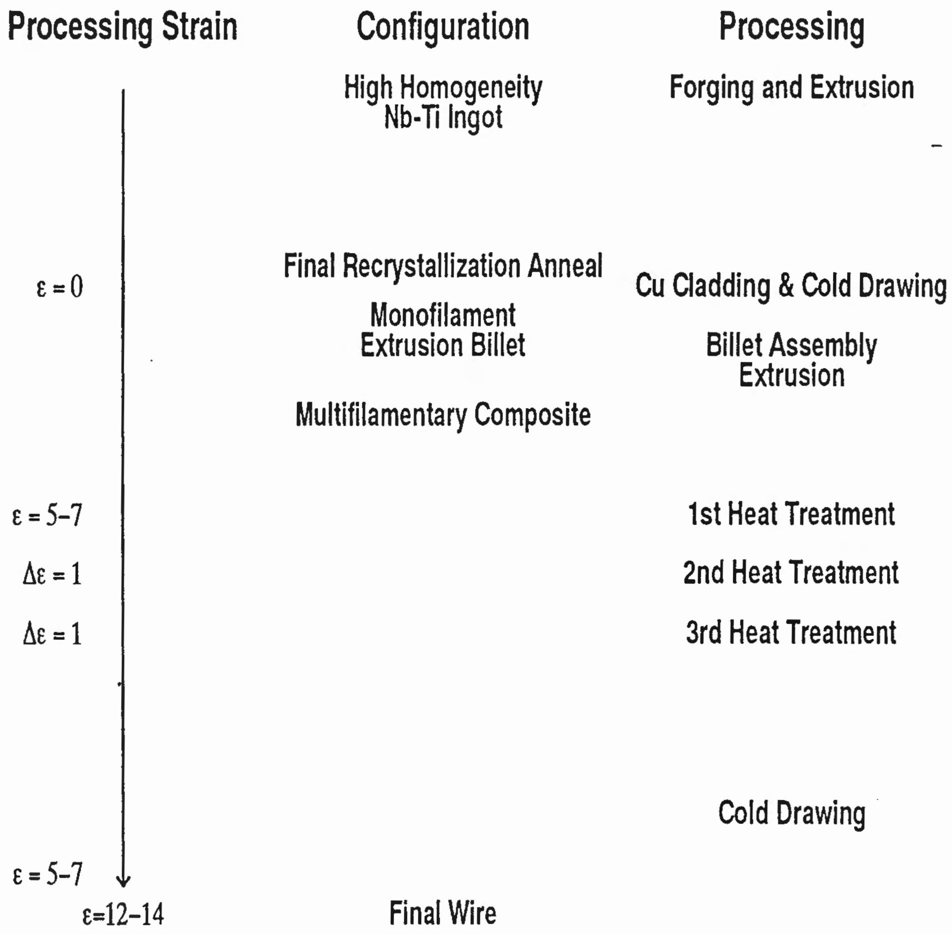

Figure 1.1: Overview of the process typically applied to conventional Nb-Ti superconductors.

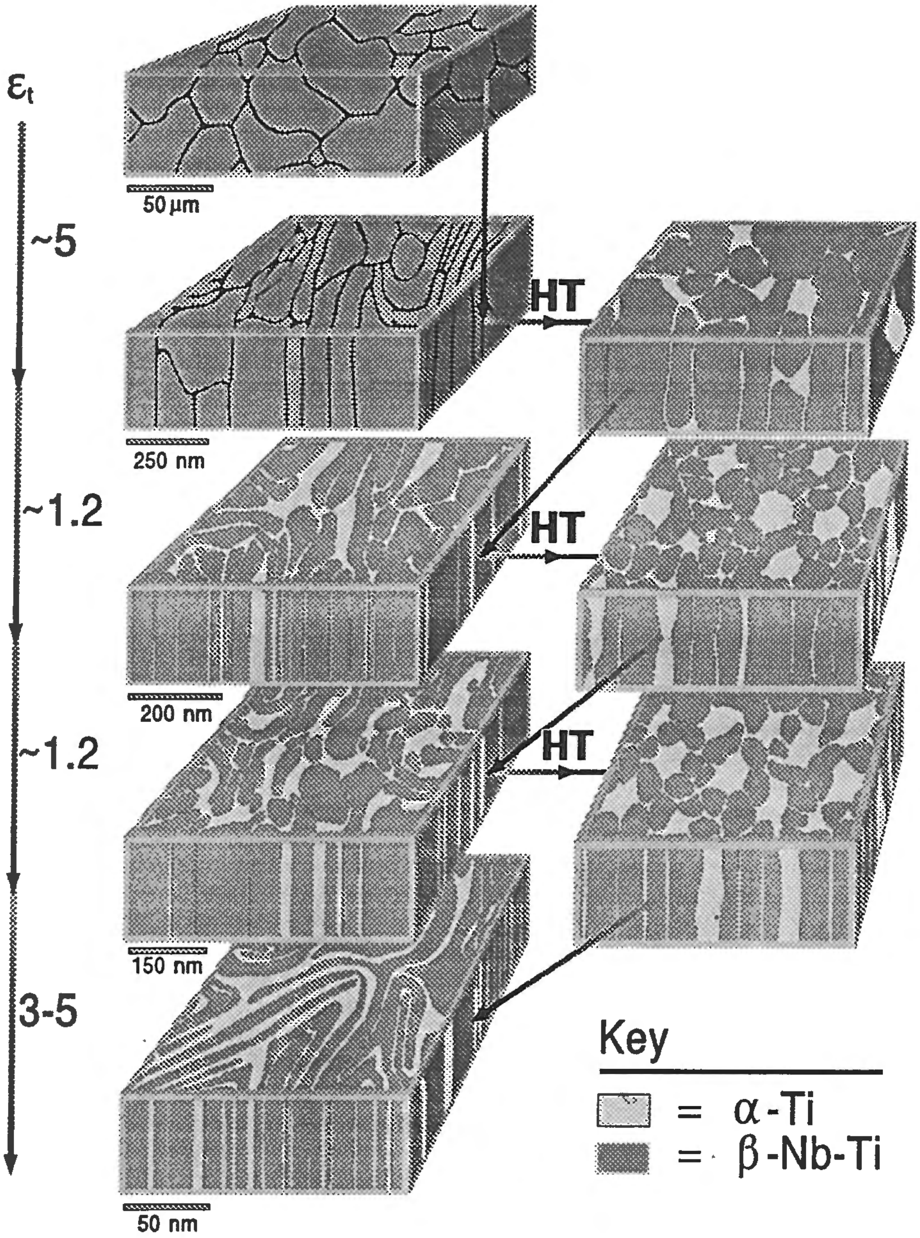

Figure 1.2: Schematic view showing the microstructural development in conventional Nb-Ti through the application of a series of heat treatments and deformation cycles. (Courtesy of Dr. P. J. Lee).

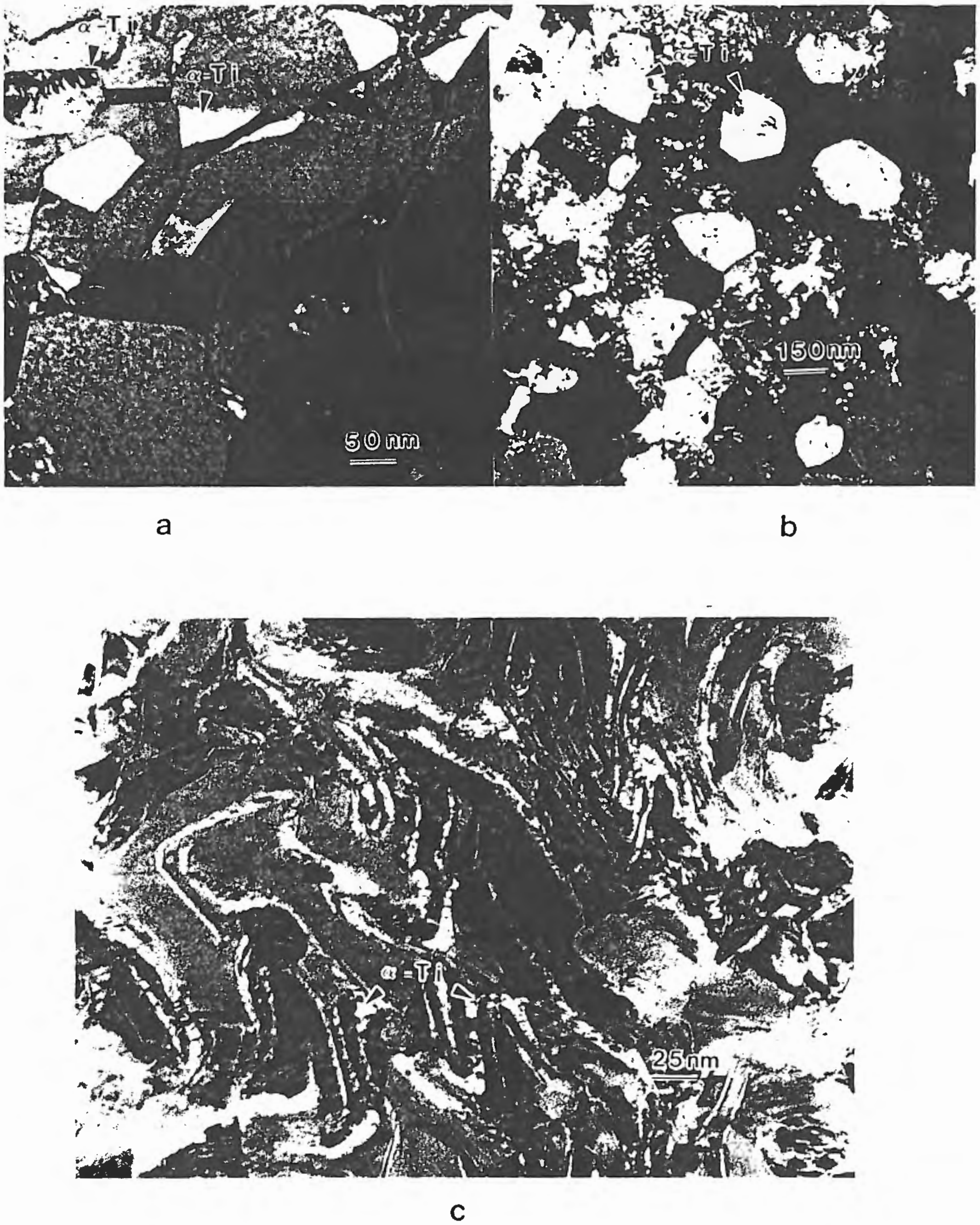

Figure 1.3: Transmission electron micrographs showing the microstructural development in conventional Nb-Ti through the application of a series of heat treatments and deformation cycles. Post first heat treatment (a), post third heat treatment (b), and near final size (c). (Courtesy of Dr. P. J. Lee).

contain more than 50wt%Ti can produce more α -Ti, they are difficult to process into wires[80], and the decrease in B_{c_2} and T_c result in a reduced J_c, especially at higher fields.

The present best J_c(5T) in a round wire[b] is 3700A/mm^2 [69] in a conductor which contained about 19 vol% α -Ti precipitates. Lee, McKinnell and Larbalestier [64] observed that J_{ct} is proportional to the volume percent of α -Ti precipitates (Figure 1.4). Thus, it would appear that further improvements in J_c could be obtained by simply increasing the amount of α-Ti. Unfortunately, 20-25vol% α -Ti precipitate is the maximum which has been developed in the high B_{c_2} Nb-47wt%Ti alloy.

To further stimulate the interest in higher volume percent second phase, Stejic et al.[106] performed flux pinning calculations on a model microstructure consisting of slabs of Nb46.5wt%Ti and α -Ti. Their key result is a prediction that maximum flux pinning will be obtained with about 40 vol% α -Ti with a thickness of $\sim \xi$ and a separation of about 1.6ξ. They further calculated that maximum flux pinning in a slab array consisting of 20 vol% α-Ti will occur when the Ti slab thickness is about 0.45ξ, the slabs being separated by about 1.8ξ. This agrees reasonably well with the results of Meingast, Lee, and Larbalestier [83] ($t_{Ti} \sim 0.2-0.4\xi$ and separation $\sim 0.6-1.2\xi$).

---

[b] Experiments [16] with rolled wires have shown that the current density may be doubled by rolling to align the microstructure with the flat face of the tape. However, the gain in J_c is at the expense of J_c normal to the alignment direction.

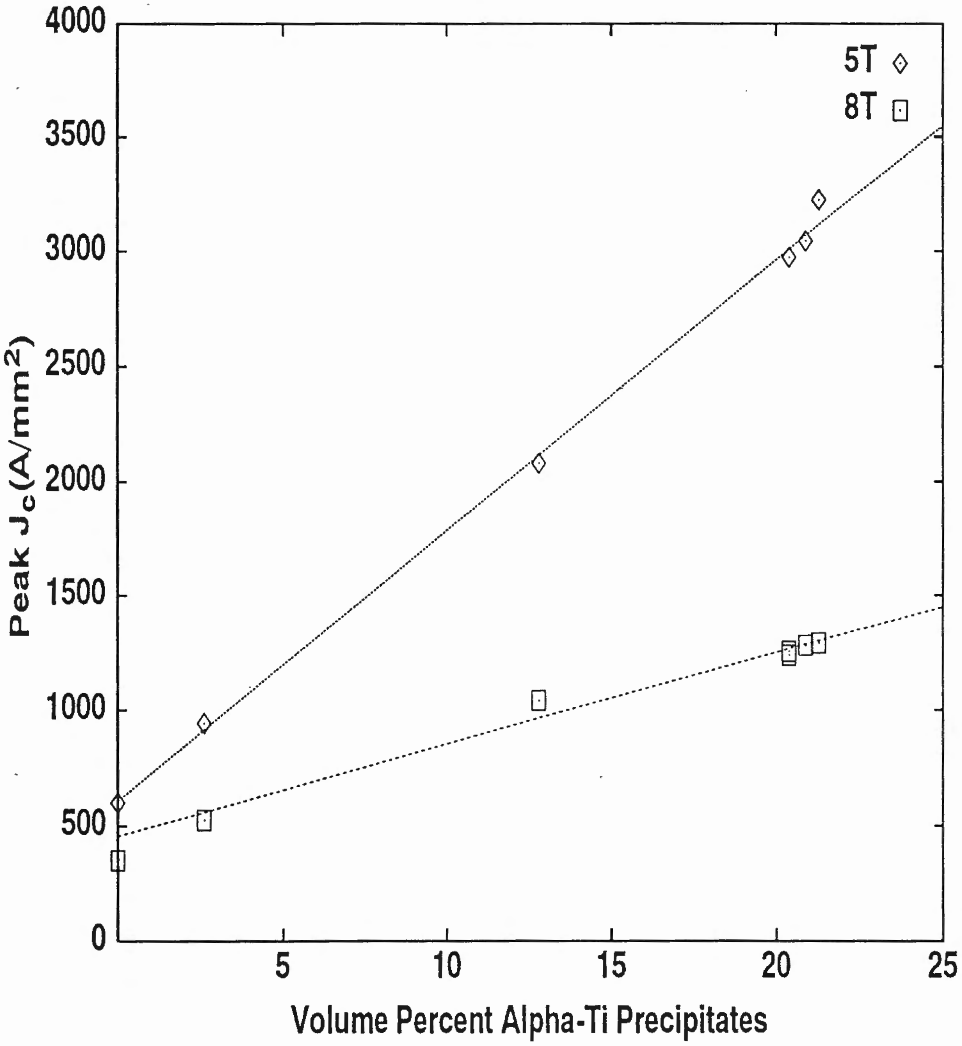

Figure 1.4: Peak J_c (5T) versus Cross section volume percent α -Ti. (Data taken from Lee et al. [65] and Warnes et al. [116]).

One might expect optimum flux pinning properties when $t_{Ti} \sim 2\xi$, and the precipitates separated by about the flux line lattice parameter a_o (4.4ξ, at 5T and 4.2K). However, while the α -Ti precipitates are normal when large compared to ξ, significant proximity effect coupling occurs[81] when they are of a size comparable to the coherence length ($\sim$ 5nm). Inducing superconductivity into these normal precipitates increases the energy of the system[77]. Thus an additional reduction in energy is obtained when a fluxon sits on a proximity-coupled precipitate, thereby "uncoupling" it. Similar calculations [107], made by substituting Nb for the slabs of Ti predicted a peak F_p at about 50 vol% Nb and for an optimum size and separation of order ξ. Thus experiment and theory both point to higher volume percent second phase as a way to achieve higher current density. Achieving this requires novel processing methods.

1.2 APC Conductors

In order to overcome the volume percent limitations inherent in conventionally processed niobium-titanium, several investigators [23, 56, 98, 99, 123, 124] have attempted to introduce the second phase artificially (thus these conductors are described as artificial pinning center (APC) conductors). The first of these conductors was reported in 1985 by Dorofejev et al. of the Kurchatov Institute of Atomic Energy, Moscow [23]. Their composites incorporated normal metal rods in the superconducting matrix during billet assembly (Figure 1.5). This work stimulated efforts by Larbalestier's group [56] and at Intermagnetics General Corporation [124]. The latter conductor was essentially an inside-out version of the earlier work in which superconducting rods were placed in normal metal tubes, several of which were bundled together and extruded to form a new composite filament. Another innovative variation was developed by Matsumoto et al. [75] where sheets of Nb-Ti and normal metal were clad together, cut into small squares, canned, extruded and then drawn into wire (quite similar to a Nb_3Al process described by Saito et al. [97], Figure 1.6). Seuntjens and Larbalestier [98] showed that a two phase microstructure could be formed by incorporating an insoluble substance during controlled melting. Recently, Scanlan et al. of Lawrence Berkeley Labs and Rudziak et al. of Supercon Corporation collaborated on a jelly roll design where sheets of Nb and Ti are formed into a roll (Figure 1.7) and reacted and processed such that a strong artificial pinning microstructure was formed in the final product[99]. Thus by the early 1990's, several processing techniques had been employed to develop APC microstructures.

To date none of these composites have been as successful as initially hoped. For example, the melt processing technique is limited to mutually insoluble alloy options which in turn limits processability and perhaps the

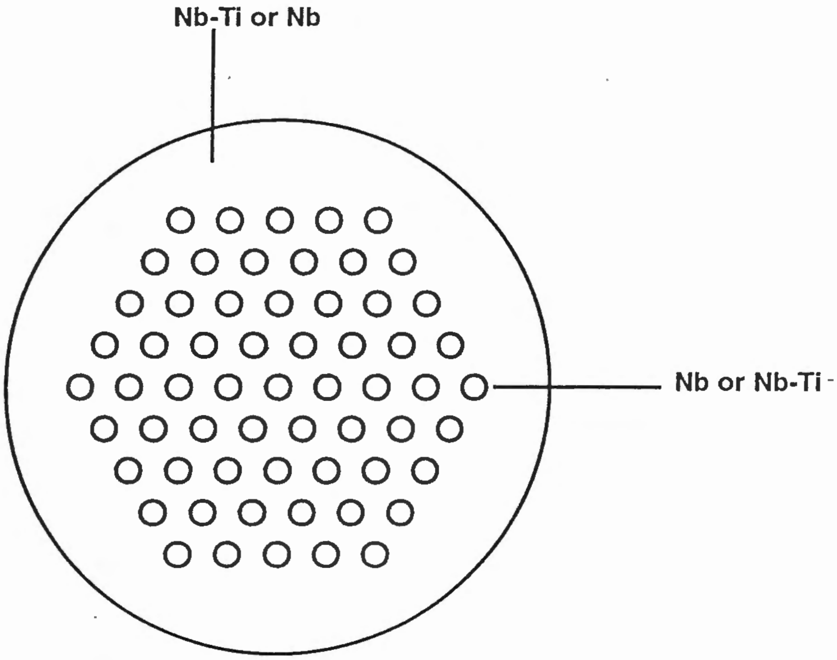

Figure 1.5: Schematic showing the APC design favored by many investigators: normal (Nb) pinning center rods in a superconducting (Nb-Ti) matrix or superconducting (Nb-Ti) rods in a pinning center (Nb) matrix.

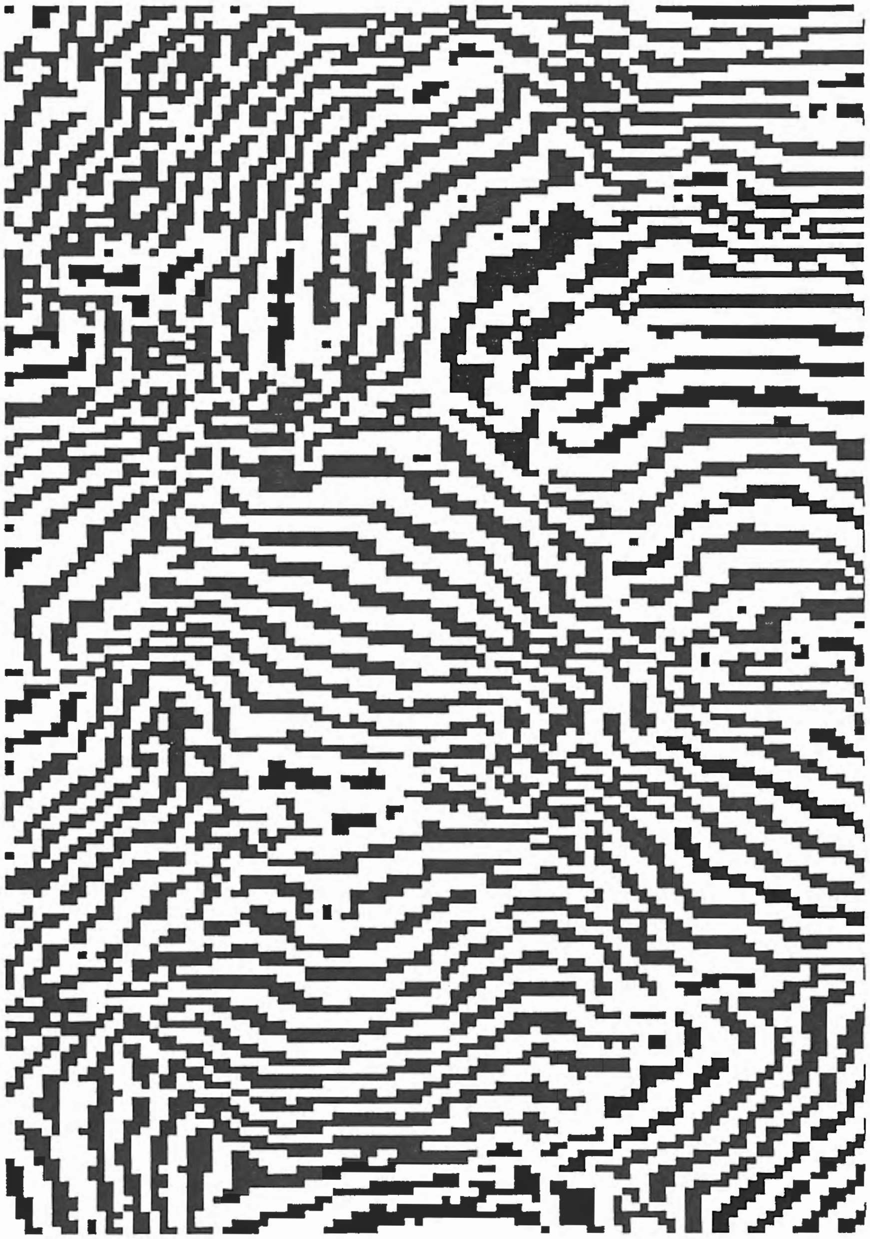

Figure 1.6: Schematic showing the typical clad-chip APC microstructure. The light phase is superconducting and the dark is the pinning center.

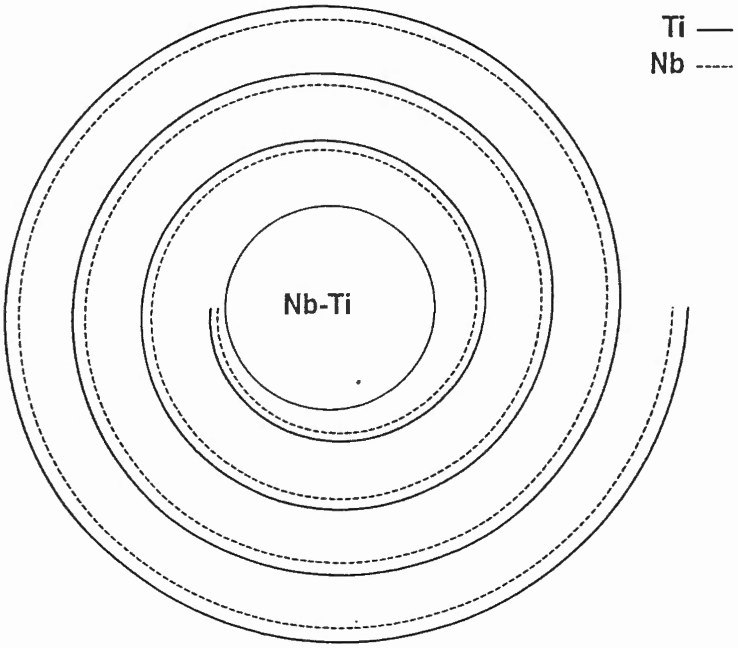

Figure 1.7: Schematic showing the Berkeley/Supercon jelly roll APC design.

superconducting properties as well. In the mechanically assembled composites, handling considerations require that the second phase be quite large at assembly (typically >2-3mm diameter). The difficulty is that the composite then requires a large amount of strain in order to reduce the second phase to a size comparable to the coherence length (ξ) which is about 5nm at 4.2K; therefore, strains on the order of 30 are required for a typical hand assembled APC conductor, versus about 12-16 to optimize conventional Nb-Ti. In fact, most attempts at developing APC conductors have experienced some fabrication problems, largely as a result of the amount of mechanical deformation required. The maximum strain obtainable from a single extrusion and drawing sequence is ~12, thus multiple extrusions are required (typically 3-4) which increases the costs and drastically decreases the yield due to end effect losses (see Chapter 2). However, if the initial size of the second phase is on the order of tens of microns, then the strain needed is only on the order of 12-14 and some of these difficulties should be reduced. Powder Metallurgy (PM) is one way to introduce a micron-sized second phase. In addition, powder metallurgy allows for a flexibility in second phase size distribution, volume fraction and chemistry that is not available with the other techniques. Powder metallurgy fabrication of artificial pinning center composites represents the core of this thesis. To the author's knowledge, this is the first work to present PM-produced Nb-Ti alloys with an artificially introduced second phase.

1.3 The PM APC Approach

The flexibility of the powder approach to artificial pinning center fabrication is considerable. This thesis describes the process for making powder metallurgy composites for which a patent has been granted[49], and the properties of the composites made from it. The process development proceeded with attention to three major aspects:

a. PM billet making: The making of a PM based two phase composite of powders capable of being deformed to large strains;

b. Composite wire fabrication: The construction of mono- and multifilamentary superconductor/copper stabilizer wire composites capable of large drawing strains;

c. Microstructural development: The ultimate goal is a finely subdivided nanostructure that produces a uniform distribution of strong flux pinning centers.

A flow chart showing the major steps of the process is found in Figure 1.8. From this overview, it should be clear that most of the main steps in the process impact two or even all of the major aspects of process development

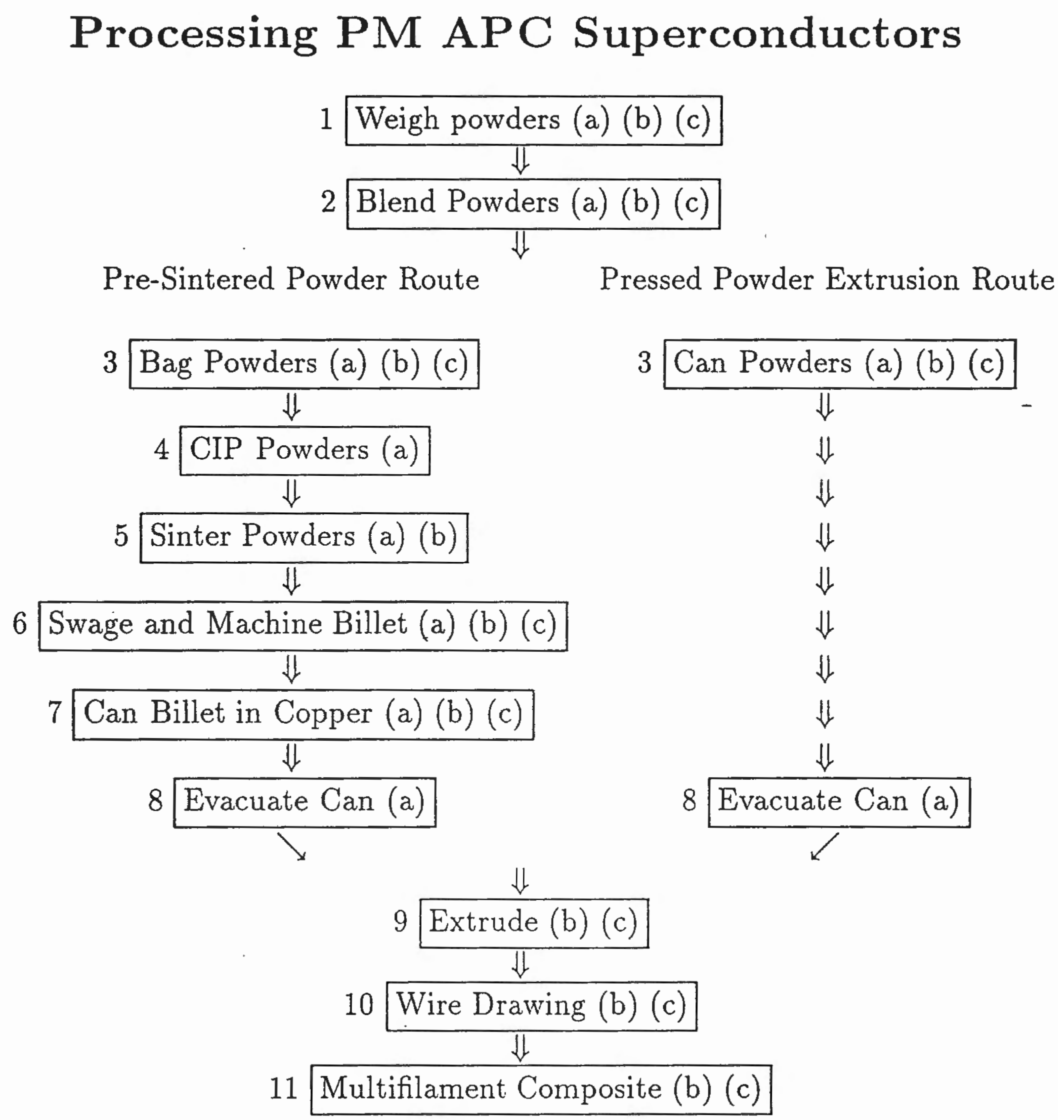

The above impact on:
(a) PM billet making
(b) Composite wire fabrication
(c) Microstructural development

Figure 1.8: Flow chart showing the major steps in producing a multifilamentary composite from metal powders. The significant aspects of composite fabrication that each step is expected to impact are indicated: (a) PM billet making, (b) composite wire fabrication, (c) microstructural development. Further details are found in Chapters 1 through 4.

outlined above. Underlying the whole process is the essential requirement that the PM billet must be fabricable into wire. This requires that it sustain strains of ~12-14 to refine the two phase PM dispersion into a nanostructure. Thus ductility is a critical factor. Full density processing and low hardness were two of the major goals of many of the initial pre-extrusion experiments (see next section). Unfortunately, these processing goals can be at odds with each other. For example, the sintering rate increases as the particle size decreases, but on the other hand, contamination from adsorbed surface gases is greater for smaller particles (steps 1-6, Figure 1.8). This can be a significant problem, because the base alloy is a β-titanium alloy which is readily hardened by H, C, N, and O interstitials. It will be shown (see Chapter 2) that the concentration of interstitials due to surface contamination (e.g., W_o, weight fraction oxygen) can be approximated by:

$$W_o \sim \frac{6 t_o \rho_o}{d_{Nb} \rho_{Nb}} \tag{1.1}$$

when the adsorbed gas layer thickness (t_o) is small in comparison to particle diameter (d_{Nb}). ρ_o and ρ_{Nb} are the densities of liquid (i.e., close packed) oxygen and solid niobium respectively. Thus surface contamination becomes comparable to the bulk interstitial impurity level when the particle size is $\sim 1\mu m$ or less. It is believed that surface contamination leading to excessive hardening is avoided by using larger size ($\sim 45\mu m$) powders (step 1, Figure

1.8).

The ductility and hardness of the superconductor becomes very important when it is sheathed in copper for wire drawing (steps 8-10, Figure 1.8). Unfortunately, while the copper deforms uniformly, the deformation in the BCC phase superconductor is initially highly localized, consisting of bands of deformed material surrounded by undeformed regions [111, 112] (see Chapter 5). Experiments ([45, 48]) were conducted to evaluate the influence of texture, grain size, hardness ratio and relative wall thickness of the copper stabilizer. The filament shape stability and the drawability of the wire were monitored. These experiments showed that reduced Nb-Ti and Nb powder grain size and increased pre-strain (i.e., texture development), as well as better hardness matching between the Cu sheath and Nb-Ti/Nb core, all led to a more uniform wire cross-section. Thus the critical parameters for the development of a PM APC superconductor were established in a series of scoping experiment composites.

1.4 An Overview of PM Extrusion Technology

Hydrostatic extrusion was found to be a valuable tool in the development of these PM composites. Unfortunately, there was little relevant literature which could be used to guide the development. In a recent review, Roberts and Ferguson[94] of Nuclear Metals (a pioneer in the field of extrusion of metal powders) stated that no published work existed on hydrostatic extrusion of metal powders. A significant literature on conventional extrusion of powders exists but most of this is on aluminum based[14, 91, 94, 100, 101, 102, 103, 125] or superalloy/tool steel based materials [85, 94]. Unfortunately neither of these groups of materials adequately models the mechanical response of Cu/PM–Nb-Ti/Nb composites because they either avoid the canning of the powder in the softer Cu or neglect the effects of the can material. What distinguishes powder extrusion from ingot extrusion is that interparticle bonds are formed, broken and reformed as the porosity is eliminated. Duszczyk [24, 125] attempted to incorporate these considerations in an upper bound calculation while Sheppard et al. used a dislocation creep model [102, 103]. The results of both of these treatments can be represented in a simplified form in which the extrusion pressure (P, normalized by the flow stress) is given by:

$$\frac{P}{\sigma} = a\ln(R) + b \tag{1.2}$$

where b is attributed to redundant deformation (e.g., the formation and fracture of interparticle bonds which is independent of the amount of reduction), a represents a measure of the homogeneous work of deformation and R is the reduction ratio; a and b can be determined by experiment. In cast materials the ratio of b/a is ~0.07 while in PM materials b/a is ~1-2. Thus the amount of redundant deformation in PM materials can be significant and is useful in improving the bond strength in the extruded solid mass. This redundant work has been found to be a function of particle size such that b increases as particle size decreases[100]. Further discussions on powder processing and extrusion are found in Chapter 2.

1.5 Summary

The maximum current density obtained in conventional Nb-Ti superconductors has remained at about 3700 A/mm^2 (5T, 4.2K) since ~1985. This performance limit appears to be a consequence of the inability of traditional thermal and mechanical processing to produce more than 20-25 vol% of second phase fluxon pinning centers. In fact, Lee et al.[65] showed that J_c is linearly related to the volume fraction of α -Ti, while Stejic et al. [106] predicted maximum J_c for an alloy containing 40-50 vol% pins. Thus further increases in J_c appear to be tied to the ability to develop a higher volume fraction of pinning centers. Although a higher volume fraction of second phase has been achieved by using high Ti alloys [79], J_c suffers because the superconducting alloy compositions have lower H_{c_2} and T_c. In regard to APC conductors, various alternative fabrication routes have been attempted: normal metal rods in a superconducting matrix [56, 123], normal metal tubes around superconducting rods [124], a metal cladding and chipping process [75], an in-situ casting approach [98] and a jelly roll process [99]. A new powder metallurgy approach is described in this thesis. This process is believed to have many advantages, including reducing fabrication strain and better control over the second phase chemistry.

Chapter 2

The Fabrication of Superconducting Composites

In this chapter we will review the basic steps taken to fabricate "long" lengths (10's of meters) of superconducting PM Nb-Ti/Cu composites. Many of the processes are similar to conventional Nb-Ti fabrication. These will be discussed only briefly so that the main emphasis can be given to the unique contributions of this thesis.

2.1 Generic Composite Fabrication Issues

Much of this section addresses fabrication issues pertinent to all ductile metallic composites.

2.1.1 Extrusion Procedures

Most low temperature superconductors are extruded as part of the mono- or multifilament composite fabrication process because extrusion can produce long lengths economically. Typically direct extrusion is utilized (Figure 2.1), a process in which the billet is loaded into a high pressure chamber and forced through a die with a ram. Thus the ram moves relative to the billet, chamber and die. Alternatively, the rear (breech) of the chamber is sealed with a breech plug and the die is backed with a hollow tube called a die stem. In this configuration the die moves relative to the billet and chamber. This variant is called "reverse" extrusion (Figure 2.2). The main advantage of reverse extrusion is that the billet/chamber wall friction is greatly reduced. The friction "hill" of direct extrusion can be significant, easily doubling the peak pressure associated with the extrusion process (Figure 2.3). Since a 25-30cm diameter press will have an extrusion force capability of 3000-5000 tonnes, the frictional force has a significant capital cost input. Thus by utilizing reverse extrusion, essentially all of the system mechanical requirements can be reduced given the same extrusion requirements. In spite of these advantages, direct extrusion presses are much more common than reverse extrusion presses.

Perhaps the main disadvantage of reverse extrusion is the hollow die stem

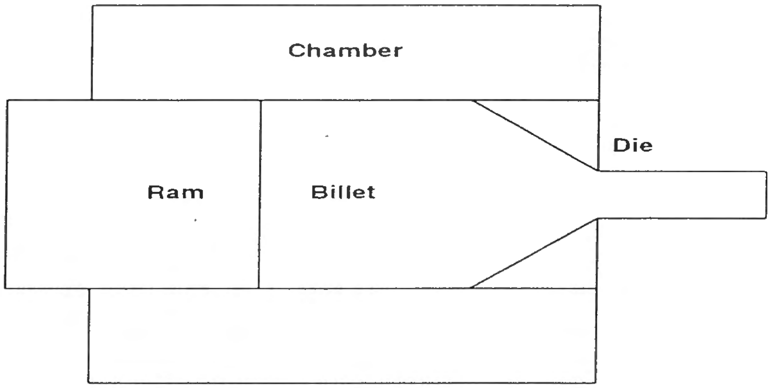

Figure 2.1: Schematic cut away view showing the direct extrusion process.

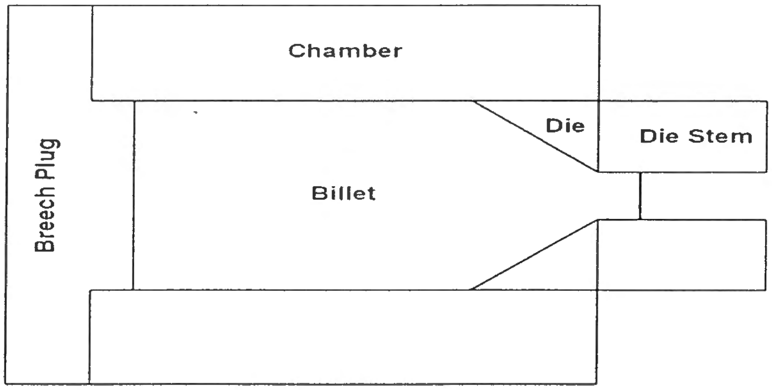

Figure 2.2: Schematic cut away view showing the reverse extrusion process.

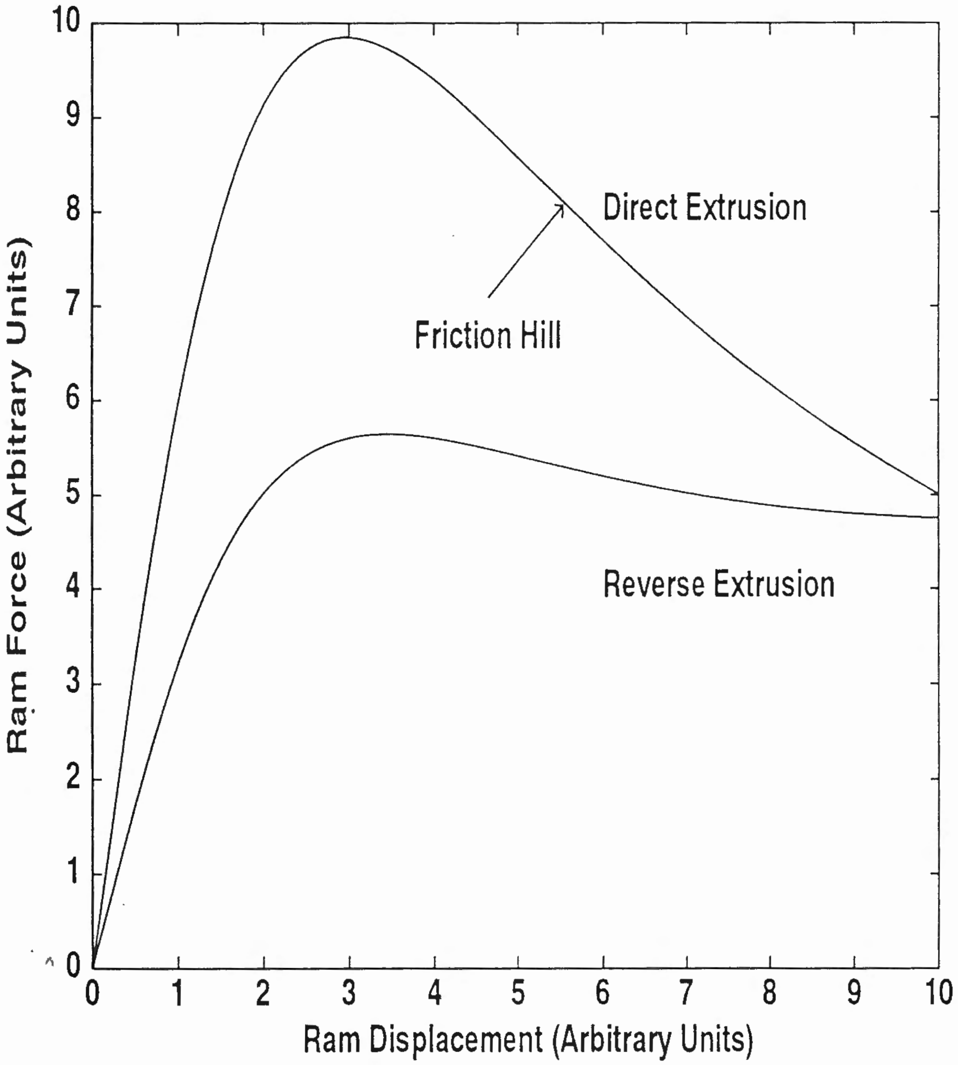

Figure 2.3: Extrusion pressure vs. ram displacement is shown schematically. Note the differences for direct reverse extrusion (hydrostatic extrusion is similar in pressure/displacement to reverse extrusion).

requirement. For maximum strength the die stem must be closely matched to the die size. Thus several die stems are required in order to produce a range of reduction ratios. This adds to equipment and production costs, somewhat reducing the savings gained from the smaller force requirements.

An even more efficient technique is hydrostatic extrusion (Figure 2.4). In this approach the pressure is applied to the billet by a fluid, hence this process is called hydrostatic extrusion[11, 95]. There are several advantages to hydrostatic extrusion. Hydrostatic pressure raises the shear to principal stress ratio in the deformation zone, thus enhancing the plastic flow. A second advantage is that almost no chamber friction is developed, except perhaps between the die and billet. Thus less energy is wasted through friction, allowing for greater reductions in area in the extruded part. A third advantage for composite billets is that the hydrostatic pressure compacts the composite billet just prior to extrusion. This is in direct contrast to conventional extrusion where the billet expands (upsets) to fill the chamber when the ram contacts the billet. Compaction then occurs subsequently as the material passes through the die.

There are many important details to the extrusion process, for example die angle and lubricant. Quantitative approaches to extrusion are discussed in Avitzur[4] and Dieter[22]. Unfortunately the number of variables is considerable and quantitative values of parameters entering the theory of extrusion

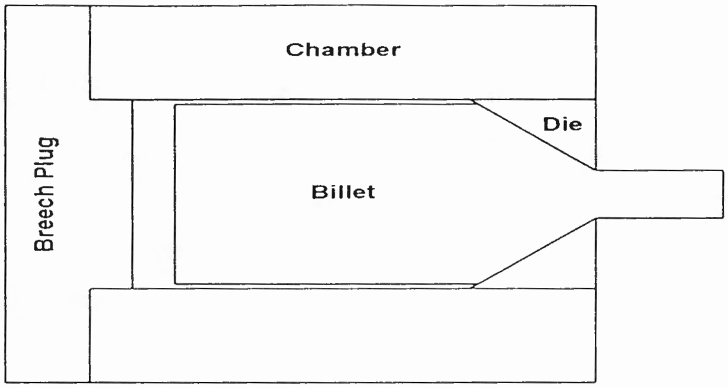

Figure 2.4: Schematic cut away view showing the hydrostatic extrusion process.

are generally quite uncertain. Thus correct extrusion conditions are usually found by a combination of the upper and lower extremes of temperature and reduction combined with actual experience. The compendium of extrusion data quoted by Collings[15] is specific to Nb-Ti/Cu composites and provided useful background information.

Typical Reduction Ratios

Reduction ratios are set by material and equipment considerations. For example, typical reduction ratios ($R = A_o/A_f$, where A_o is the billet cross sectional area and A_f is the extruded product cross sectional area) on aluminum can reach several thousand, while high strength materials like steels or superalloys are generally limited to reductions of less than 10. Typical industrial extrusion presses are ~0.3 to 1m long and ~2 to 30cm diameter. Typical ratios for conventional extrusion of Nb-Ti/Cu composites are 16 to 25. Hydrostatic extrusion of Nb-Ti can reach reductions of ~50. Extrusion ratios and temperatures are generally determined by the pressure limitations of the presses used. Thus Nb-Ti/Cu composites in the U.S. are normally extruded as 25-30cm diameter billets in direct extrusion presses having extrusion force capabilites of 3000-5500 tonnes. Breakthrough forces required to start extrusion are normally limited to ~80% of the maximum press capacity, thus limiting the temperature to a minimum of ~575°C. Avoiding Cu-Ti reactions[59] places an upper temperature limit of ~620°C, thus constraining conventional Nb-Ti extrusion to a narrow temperature range. Hydrostatic extrusion permits the temperature to be reduced to ~400-450°C, completely eliminating Cu/Nb-Ti reaction problems. However the largest hydrostatic extrusion presses are <20cm in diameter, and none of these ASEA-built presses exist in the U.S.

A final consideration in extrusion is the need to retain cold work during fabrication[67, 92] so that the α -Ti precipitation process is not disrupted. Thus the billet should not be extruded to too small a size so that the minimum wire drawing strain of ~7 is available (Figure 1.1). A final wire size of ~0.5mm to 0.75mm sets the extrusion product diameter to ~17mm to 25mm.

Extrusion Forces

An estimate of the extrusion force is needed prior to attempting to extrude a composite billet of some new design. In conventional extrusion, the extrusion force can be estimated by

$$F = KA_o \ln(R) + b \tag{2.1}$$

(which is similar to eqn. 1.2) where F is the ram force, K is the deformation resistance of the billet, A_o is the billet cross sectional area, R is the reduction ratio and b is a constant near 1 which can be ignored in many cases (b again represents the redundant deformation which is insignificant in nearly fully dense materials such as conventional composite billets). For a typical extrusion, $K \sim 3 - 4 \times \sigma_f$ where σ_f is the material flow stress at the extrusion temperature. For composites, σ_f can be estimated using the rule of mixtures, thus giving an estimate of the extrusion force.

2.1.2 Wire Drawing

Once a billet has been extruded it will normally require further drawing to reach the desired cross section and/or to refine the microstructure. This section will serve to overview some of the basic considerations involved in wire drawing. A discussion of some of the drawing equations will be postponed until Chapter 4 where they serve to define some of the process refinements made on the PM conductors.

Reduction of Area

Wire drawing is similar to extrusion, except that there is an additional traction force on the front of the material (i.e., the wire is in tension due to the drawing force). Thus sufficient work hardening must occur during drawing in order to support the reduction ratio, friction, and redundant deformation of wire drawing. If this strength gain during passage through the die is insufficient, the wire will fracture, even if it is defect free (see Chapter 4). A further consideration is that the front of the wire (the point) must be reduced to a size which will easily fit through the die so that it may be gripped by the drawing ram. Experiments in our lab have empirically established the minimum point area to be $\sim 0.85 A_e$ (where A_e is the die exit cross sectional area) when drawing Nb-Ti/Cu composites ~20% reduction in area per die pass.

2.2 The Patented PM process

What follows is a detailed description of the PM Nb-Ti APC composite fabrication process. While many of the processing steps may appear to be self-evident, they were in fact developed through careful consideration of powder processing theories with special attention given to all aspects which could impact on the flux pinning strength of the final size microstructure. At the heart of the process is a dichotomy. On the one hand, sufficient diffusion must occur in order to produce strong interparticle bonds. On the other hand, Nb-Ti/Nb interparticle diffusion must be limited in order to retain the two phase microstructure required for strong flux pinning *even though the Nb-Ti and Nb phases are fully soluble at all the heat treatment temperatures used in this thesis.* Included is a discussion of the precautions taken to ensure that the wires are drawable through to their final size at which the desired nanostructure is obtained.

2.2.1 Powder Handling

Powder handling underlies all subsequent processing steps. Unless the powder is blended and compacted properly and with minimal contamination, it is likely that fracture will occur at a later stage.

Powder Contamination Issues

Contaminants can be in the form of solids: a) substitutional solid solution, b) particulates (metallic or oxide) mixed with the base powder, or c) particulates (metallic or oxide) contained as inclusions in the base powder particles; or in the form of "gas" contaminants: a) interstitial (base powder) impurities dissolved in the powder or b) gaseous contaminants adsorbed on the powder surface. The distinction between impurity particles mixed in with the powder or impurities included within the powder particles is important because individual foreign particles are much easier to identify and remove than are inclusions within the base powder. The concentration of contaminants is initially set by the powder manufacturer; thus clean powder manufacture is an essential first requirement of the PM APC process. We paid attention to both types of contaminants.

Admixed foreign particles which are larger than the average base powder can be removed by hand from small quantities of powder or alternatively, they can be removed by sieving the powder. Particles which are smaller than the base powder can also be sieved providing the particles do not cling to the base powder. Foreign powders which are of the same size as the base powder can be removed by a number of processes including magnetic and air separation if the particles have the proper physical property distinction from the base powder[9]. Fortunately none of these techniques were required for this thesis.

Surface contamination is best avoided by maintaining an inert gas atmosphere in contact with the powder surface. This was done whenever possible. Unfortunately, sintering conditions which give rise to efficient densification (see the next section) generally tend to increase levels of interstitial contaminants. Even at vacuum levels of 10^{-5} Pa, a monolayer of gas molecules (mostly water) is expected to be on the powder particles. This has particularly negative implications for smaller particles because their large surface-to-volume ratio implies more interstitial contaminants. An estimate of the contamination level and thus the effect of particle size can be made by considering a spherical niobium particle of diameter d_{Nb}, with a layer of oxygen of some thickness t_o, and ρ_o and ρ_{Nb} the respective densities. The weight fraction of oxygen is given by:

$$W_o = \frac{V_o\rho_o}{V_{Nb}\rho_{Nb} + V_o\rho_o} \tag{2.2}$$

or more simply:

$$W_o \sim \frac{V_o}{V_{Nb}\frac{\rho_{Nb}}{\rho_o}} \tag{2.3}$$

when the volume of oxygen is not large (certainly the situation considered here). Substituting for the volumes of the Nb sphere and oxygen shell into Equation 2.3 and dropping terms containing t^n when n is higher than one simplifies the expression further:

$$W_o \sim \frac{6t\rho_o}{d_{Nb}\rho_{Nb}} \tag{2.4}$$

Thus the weight fraction of oxygen is directly proportional to the layer thickness and inversely proportional to the particle thickness, i.e., halving the thickness or doubling the particle size halves the weight fraction of oxygen.

If we assume that a monolayer of close packed oxygen (we will use the density of liquid oxygen to estimate the density of the oxygen layer, ρ_o) is on a $50\mu m$ diameter spherical Nb particle, we find that it adds less than 2ppm to the overall oxygen content. However, if the Nb particle diameter were $\sim 0.5\mu m$, the additional oxygen would be ~200ppm, given the same thickness layer. The significance of these impurity levels can be assessed by comparison to the properties of ingot Nb-Ti alloy. Superconductor grade Nb-47wt%Ti has an interstitial impurity content of <800ppm, while rivet grade Nb-55wt%Ti is additionally hardened by permitting the interstitial to raise to ~1600ppm. We wished to minimize the additional hardening due to adsorbed gas. In this respect we considered the surface contamination to become significant when the particles are submicron, because this size raises the oxygen content to a few hundred ppm, comparable to typical bulk oxygen contents. In addition, the driving force for contamination is much higher for the smaller particles because of the higher surface energy (Equation 2.5). Thus while a smaller particle size leads to better sintering kinetics, it also produces more contamination in the final product. In addition, an increase in sintering temperature is expected to increase specimen reactivity by increasing the driving force for the reaction (i.e., a higher ΔG of reaction), as well as by increasing the reaction rate (chiefly by increasing the diffusivity and solubility of interstitials). Thus any powder metallurgy billet making scheme must balance sintering kinetics against reactivity and contamination considerations.

Powder Blending Considerations

The production of a uniform blend of two or more powders is, in principle, simple but it can be difficult to implement in practice . If the powders are nearly identical, like orange and white golf balls, then a completely random distribution would exist when the powders were fully mixed. However, powdered metals typically have various shapes, ranging from spherical to irregular, have differing surface roughness and may have very different densities. These differences complicate the mixing process. In addition, once mixed, powder mixtures can settle. They will tend to unmix if large density differences exist and they are handled improperly (see below).

Powder blending was accomplished in a clear cylindrical vessel filled ~1/3 to 2/3 full. Once the powders were loaded, the vessel was rotated endwise in order to remove gross scale segregation. Once this was accomplished (usually 3-4 rotations) the vessel was rotated axially ~5-10 minutes for charges to ~700g or several minutes past any evidence of nonuniform distributions. The proper rotation speed is one which allows the powders to shear past the underlying layers. This eventually allows all particles to come into contact with each other. Irregularities in the powder particle layers will tend to trap some of the particles in new positions. This provides the thorough mixing desired. Once the powder is blended uniformly, subsequent handling should be minimized. It is best to blend the powder just before use to avoid any settling (most buildings have low level vibrations which can cause particle separation).

For the earliest experiments, angular powder particles of Nb and Nb-Ti made by the hydride-grind-dehydride (HGD) process were used. These angular powders ~45-75μm in diameter held together when pressed. However, powder cleanliness issues forced a switch to Plasma Rotating Electrode Process (PREP) powder (Chapter 3) which was spherical. Unfortunately, this change led to several problems. For example, the PREP powder mixtures would not hold their pressed shape; i.e., they had no green strength (see below). In addition, the powders would tend to un-mix if handled aggressively (see below and Chapter 3). These difficulties were overcome by pressing the blended powders directly into the extrusion can thus minimizing handling (see below).

Cold Isostatic Pressing

As mentioned in Chapter 1, Figure 1.8, there are two billet fabrication routes: presintered billet and powder extrusion. Here we discuss the presintered route. There are many ways to fabricate a powder preform, all of which essentially involve producing a powder compact with some "green" strength due to interparticle welds and particle interlocking. To develop sufficient green strength for the billet to be handled, we found that the particles need to be irregular rather than spherical in shape. The irregular particle shape provides point-like contact between particles which produce local "cold welds" upon pressing. In addition, irregular particles tend to interlock, providing additional strength to the compact.

It was found that the most convenient way to shape fifty to a few hundred grams of powder into a form which could be processed into wire was to load the properly mixed powder into a cylindrical vessel and apply hydrostatic pressure via a cold isostatic press (CIP). Square-ended cylindrical rubber tubes with one end closed (a CIP bag) of various diameters were used to press billets. The tube walls were about 1mm thick. It was found that they could be handled with relative ease and reused several times.

A typical sintered billet fabrication process involved the following steps. The CIP bag was prepared by wiping clean with methanol inside and out. A piece of aluminum foil was used to line the tube to minimize friction between the tube wall and the powder, thereby minimizing powder separation during filling. The aluminum foil also kept the open end of the bag free of powder, which provided a much better seal prior to pressing (see below). The tube was stood upright (supported by an appropriately sized cylinder when necessary) and the powder mixture was poured inside. After remov-

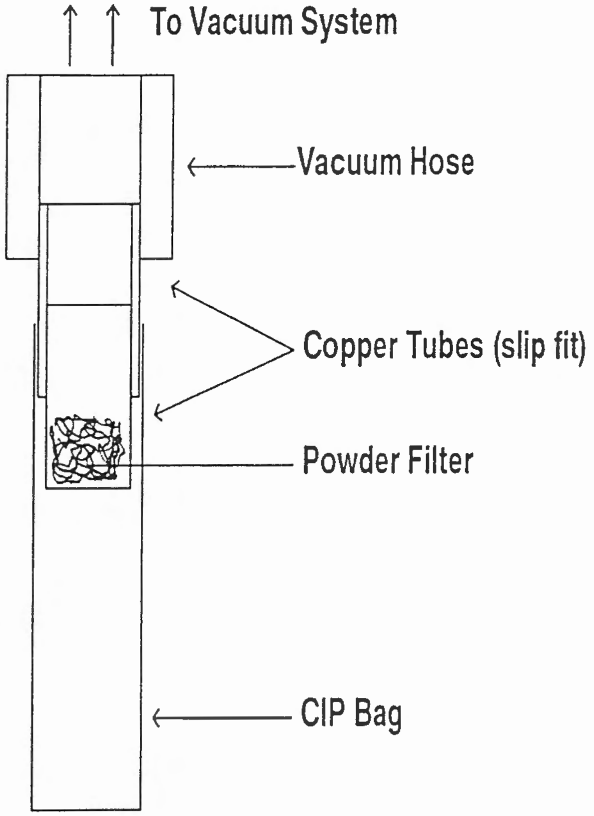

Figure 2.5: Cutaway view of a fixturing device which allows rough pumping powder mixtures in a rubber CIP bag prior to cold pressing is shown. Special features include the powder trapping filter and the inner tube which can be slid inside the outer tube to provide collapsed bag area which can be sealed to maintain a vacuum and prevent contamination with fluid during pressing.

ing the aluminum foil, the powder was degassed by a mechanical roughing pump to a vacuum of ~10Pa using the fixturing device shown schematically in Figure 2.5. There were several advantages to degassing at this stage. For example, loose powders are easier to degas than a pressed billet, and once degassed as powder, the pressed billet tended to pump down easier. In addition, degassing before pressing provided cleaner powder surfaces, potentially providing a higher green strength and a higher purity sintered billet. When degassed, the powder preform also became rigid, providing some additional control over the pressed billet shape. Once the powders were properly degassed, the interior tube was pushed into the outer tube on the fixturing device (Figure 2.5) and the newly collapsed portion of the rubber tube was twisted and secured with rubber bands. This typically maintained the vacuum while the remaining end of the tube was released from the fixturing device and bundled and secured with additional rubber bands. If the tube lost its rigidity, it was deemed to be insufficiently sealed and was repumped and resecured. Before instituting this procedure several billets were lost due to ingress of CIP fluid during subsequent pressing. Thus the pre-evacuation of powders served as a security measure to avoid contamination with CIP fluid. Once the open end of the bag was secured, the outside was lightly dusted with zinc stearate (a dry lubricant) and inserted into a loosely fitting tube. The bag and tube arrangement were suspended from a wire inside the

CIP and pressed to ~50ksi (the maximum pressure of our unit). By placing the CIP bag into a tube the billet tended to develop a straight cylindrical shape. The billet was removed from the bag by gently peeling the bag away, while being careful not to exceed the limited green strength of the billet.

2.2.2 Billet Handling

Sintering

The driving force for sintering is the reduction in surface energy of finely subdivided metal powders. This surface energy is given by

$$E = \frac{\gamma\Omega}{kT}\left(\frac{1}{R_1} + \frac{1}{R_2}\right) \tag{2.5}$$

where γ is the surface energy, Ω is the atomic volume, R_1 and R_2 are the particle radii of curvature, and kT has its usual meaning. The early stages of sintering can be described[25, 73] by

$$\left(\frac{X}{R}\right)^n = \left(\frac{\beta t}{R}\right)^m \tag{2.6}$$

where X is the neck radius, R is the powder radius (assumed to be monodispersive), t is the isothermal sintering time, n and m are determined by the transport mechanism and the particle size (respectively), and β contains the remaining material and geometric dependencies. A useful summary of sintering constants for a number of densification mechanisms is found in Table

Table 2.1: Coefficient Values [30] for the Initial Stages of Sintering, Eqn. 2.6.

Mechanism	n	m	β
plastic flow	2	1	$9\pi\gamma b D_v/(kT)$
evaporation-condensation	3	1	$(3P\gamma/\rho^2)(\pi/2)^{0.5}(M/kT)^{1.5}$
volume diffusion	5	3	$8D_v\gamma\Omega/(kT)$
grain boundary diffusion	6	4	$20\delta D_{gb}\gamma\Omega/(kT)$
surface diffusion	7	4	$56D_s\gamma\Omega^{1.33}/(kT)$

2.1. It should be clear by examining Equation 2.6 and Table 2.1 that, for the majority of the sintering mechanisms, the densification rate increases exponentially with increasing temperature. As already noted, the sintering rate is very sensitive to particle size (especially for surface or grain boundary diffusion); smaller particles allow for more rapid sintering.

Sintering improved the mechanical strength of the green billet but our desire to improve its strength was at odds with the desire to keep the Nb particles unalloyed. Thus the sintering temperature had to be chosen so as to produce sufficient diffusion to improve the strength of the billet (largely through the growth of the neck radius X), while not compromising the two phase structure needed for artificial flux pinning. We estimated the diffusion distances in the pinning center and matrix materials where $x = \sqrt{Dt}$ with D

taken from the diffusion data on Nb and Ti diffusion in Nb-Ti compiled by Moffat[86]. It was predicted that for 1h at 1175°C, $x = 40nm$ into Nb while $x = 4\mu m$ into Nb-Ti. Thus this thermal cycle fulfilled the minimum contamination requirement. It was found that a 3h/1175°C sintering treatment was required to provide sufficient bond strength to further process billets (while still providing minimum Nb contamination).

Both Nb and Ti are very reactive at the 1175°C sintering temperature, thus special precautions were taken to maintain billet quality. The billets were wrapped tightly with high purity Nb foil. Nb foil end caps were then attached to provide total encapsulation. After wrapping, the billet was inserted into a quartz tube. Quartz was selected because of its ease of workability and inert nature. Along with the billet, several pieces of hafnium metal, also wrapped in Nb foil, were inserted into the quartz before evacuating to $< 10^{-5}$Pa which typically took overnight. The vessel was backfilled with $\sim$50kPa argon gas before sealing in order to minimize the evaporation of Ti inside the vessel during sintering. Titanium can devitrify quartz, which will fracture during cooling through one of the many phase transformations in the crystalline Si-O system. After sealing the quartz, the hafnium pieces were heated to red heat in order to react them with any residual reactive gases inside the vessel prior to sintering. A cover gas of argon was maintained on the outside of the quartz during sintering so as to provide an equal oxygen activity on both sides of the quartz thus preventing oxygen from diffusing in. After sintering, the billet was air cooled while still in the quartz.

Swaging and Machining

Swaging is a process that is somewhat analogous to drawing except that the die is halved or quartered. This design allows the die to be iteritively opened and closed upon the workpiece, thereby reducing the diameter. The dies are generally rotated to accomplish the opening and closing and to minimize flashing, i.e., the "extruding" of surface material into the die seams.

After sintering the billet was swaged. Swaging reduced the billet diameter, straightened the billet and helped reduce the residual porosity. Swaging was not without difficulty, however, since the as-sintered billets were neither perfectly round nor straight, and their as-sintered surface was rough. Since swaging is a fairly aggressive process, some billets broke. The crack formation mechanism can be understood by considering a spherical pore (Figure 2.6). When an external radial pressure is applied to the ingot, a compressive force results on the pore in the radial direction while a tensile force is produced in the axial direction. In addition, there is a billet/die friction which results in a torsional shear stress. This shear stress is a critical factor controlling the crack formation/propagation, as all the cracks observed spiral around the diameter of the billet to some extent. The surface friction is

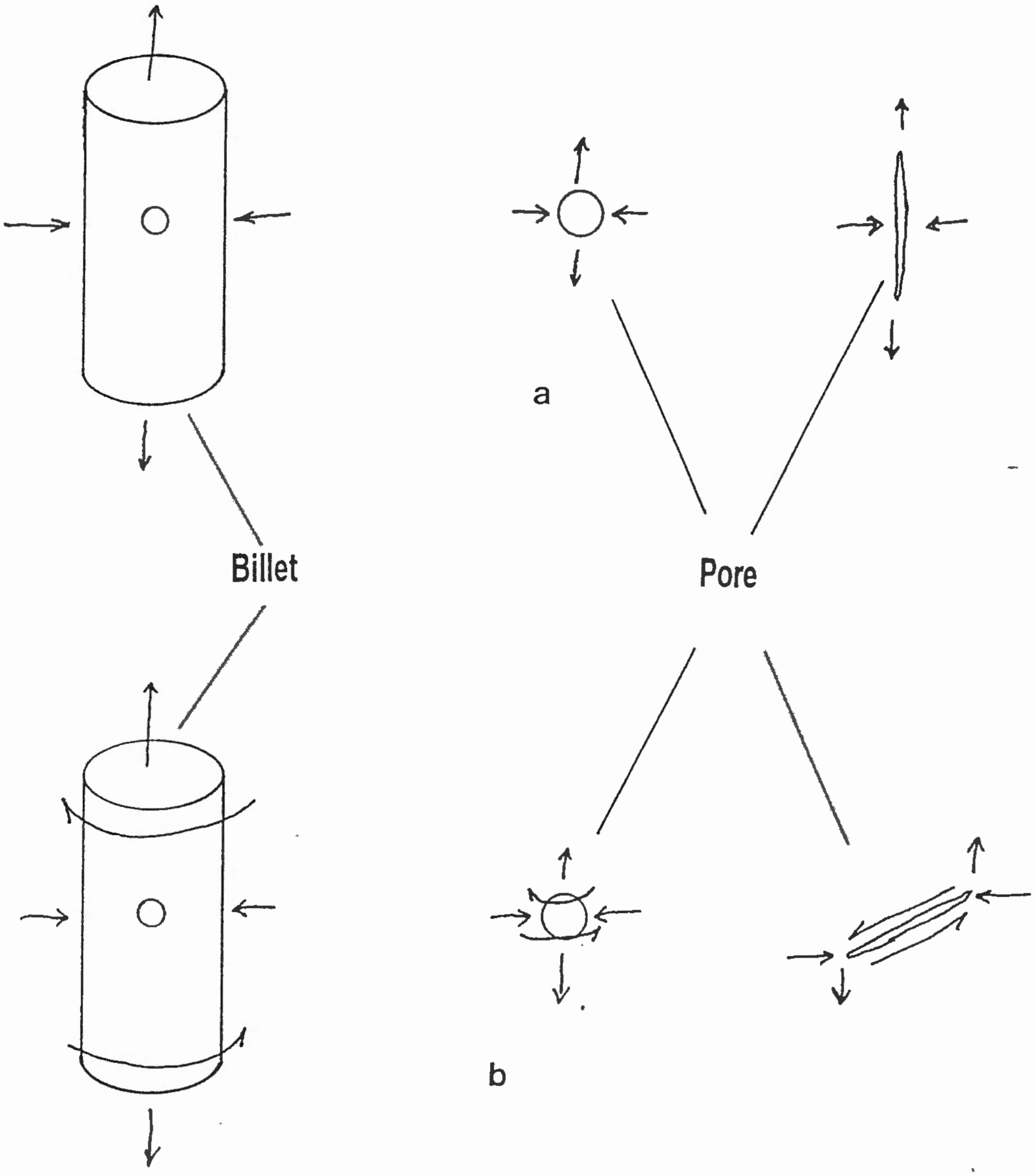

Figure 2.6: Schematic of the deformation that occurs during swaging. In (a), friction is neglected. Note that while the action of the swage dies is compressive, there is a resolved tensile force also. In (b), friction is considered. Note that depending upon the magnitude of the frictional forces, the orientation of the closed pore may change. Note also that the torsional stresses coincide with the observed surface cracks.

related to the feed rate, strain, surface velocity, and surface roughness. The material surrounding the pore must undergo strains on the order of one or more upon closing, while the surrounding material is essentially unstrained, because most of the deformation is accommodated by the region surrounding the pore. The net result is that a closed pore incorporates highly work hardened material surrounded by only slightly strained material. Furthermore, the pore walls are not metallurgically bonded and therefore cannot transmit stress or strain efficiently. We reduced the shear stress on the closed pores and thus the tendency to form radial cracks by allowing the billet to rotate at a slightly slower speed than the swaging dies. When allowed to rotate at the same speed, it was found that "flashes" of surface metal were formed. Swaging was halted when a significant number of longitudinal surface cracks appeared (radial cracks were avoided by allowing the billet to rotate). At this point another thermal treatment (2h/1175°C) was given in order to diffusion bond the pores closed during swaging and thus impart additional mechanical strength. This cycle of swaging and heat treating was repeated (typically 2-3 cycles) until there was no observable residual porosity by light metallographic examination of polished cross sections. This state corresponded to one in which the rod was then drawable.

Once swaged, the presintered extrusion billet was machined to improve the surface finish, as well as for better dimensional control. In order to minimize contamination during machining, no cutting fluid was used; instead flowing argon was used as a cover gas and coolant on the billet. In addition, a slow machining speed was used to minimize heat build-up in the billet.

2.2.3 Sheathing, Round Drawing, and Hexagonal Drawing

Several of the early conductors were processed into wire without extruding. These were densified by a series of swaging and heat treatments. Once a rod was fully dense, it was sheathed in copper and drawn into wire. Here some difficulties were encountered. Swaging produced a fairly smooth and uniform rod. While a smooth surface is desirable for filament uniformity in the final product, it negatively impacts the ability of the rod to bond with the copper sheath. The first 15cm on sheathed and drawn composites were typically lost to breaks because of poor bonding. Some improvements were obtained by "warm" drawing the composite through several dies in repeated succession without letting it cool too much between die passes. Thus the composite was warmed by the "cold work" of wire drawing which apparently was sufficient to improve the interface bonding.

It was found that it was important to maintain alignment of the die, ram and composite during wire drawing. Good alignment provided the lowest drawing force and produced uniform axial symmetric reduction which is very important, especially in the case of a multifilamentary wire. In addition, die/wire misalignment tended to debond these composites which led to further wire drawing difficulties.

Whenever a composite was drawn through a hexagonal die, the wire was handled straight at all times. The optimum area reduction was found to be 20%. At larger reductions the wire would break, and at smaller reductions the full hexagonal shape would not be formed. The corners of the die were given special considerations. Multifilamentary composites made from hexagonal stacks with very round corners tended to have distorted, star shaped filaments, apparently because the material flowed to fill the voids at the corners. However, if the corners were too sharp, the drawing force tended to exceed the fracture force and the wire broke. Thus a compromise was required. Wire hexagon quality required constant attention because the corners of the die tended to collect debris, thus rounding the product corners. In addition, at least one defective hexagonal die was found. This die put a spiral in the hexagon drawn wire, suggesting that one side flowed faster than the other. When a "new" die was selected, a test piece of copper was drawn through the die first and examined for quality. Once the wire was hexagon drawn, it was kept straight until cut into equal length pieces for stacking into a multifilamentary composite.

2.2.4 Extrusion Billet Assembly, Evacuation and Seal-off

The fabrication process from cold isostatic pressing through sheathing and drawing is very lengthy and complex. There are many opportunities for mistakes resulting in the composite breaking up during wire drawing. However, if the billet or powders can be formed into a fully dense monofilament by extrusion, the process becomes much simpler and the chances for success are increased. During the course of this thesis we purchased a hydrostatic extrusion press from Naples Research and Manufacturing, Inc. and developed a process to form fully dense monofilaments from sintered billets and compacted powders (see process outline, Figure 1.8).

The extrusion cans were fabricated from UNS C10100 copper. Most of the can bodies were made from 15.9mm OD by 12.7mm ID by 75mm length tubing while the nose-cone and end caps were machined from bar. A copper tube was welded to the back side of the nose-cone to permit pumpdown of the assembled billet (Figure 2.7). All welding was done in an inert gas glove box. While the pumpdown tube was welded to the nose-cone by hand, the can itself was welded in the fixturing device shown in Figure 2.7. First the endcap was secured to the can. Then the assembly was placed on the copper supports and secured to the drive tube. The endcap was extended ~10-15mm beyond the

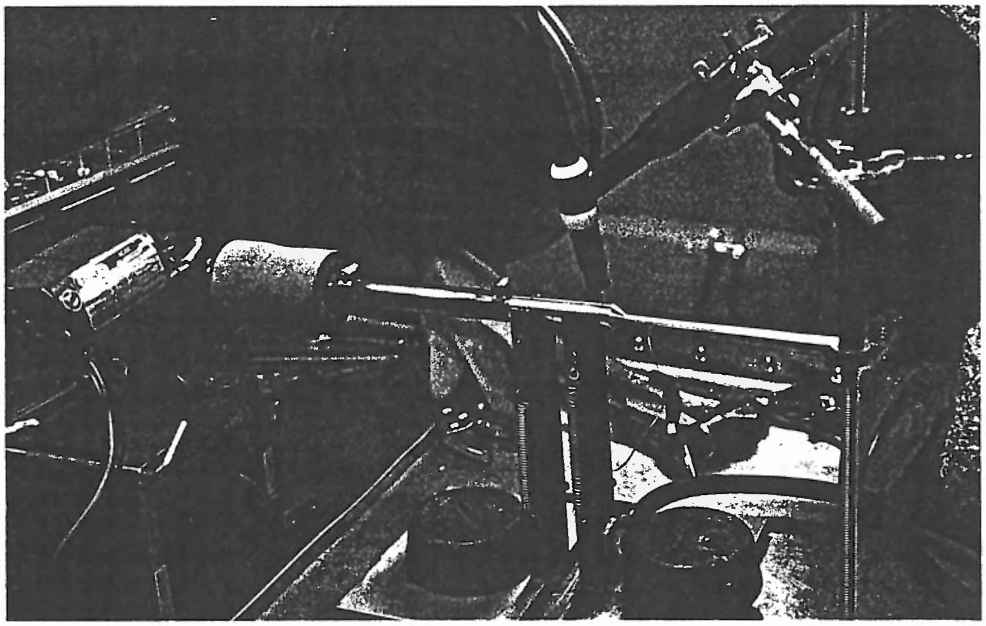

Figure 2.7: An extrusion billet is shown in the copper supports and drive mechanism which are used to weld the billets circumferentially prior to extrusion.

outer support to avoid excess heat outflow through the outer support. The cap was tack-welded into place in 2-3 locations while the tube was stationary. Once tacked in place, a weld bead was run around the entire seam by first starting a weld pool while the billet was stationary and then rotating at ~4-8 RPM while the weld pool was still molten. The rotation speed and current required adjustment during welding, typically towards faster rotation and lower current as welding proceeded. The nose-cone was welded after loading the billet into the can in a similar manner. However, it generally needed to be held in place during tack welding and required more current because it was more massive than the endcap. Additional steps were taken to help prevent contamination of the billet. One such precaution was to design the billet (or powder height) and can such that the billet did not extend beyond the outer copper support during welding. This copper support acted as a heat sink and helped limit the billet temperature during welding to below ~500°C. Also, a series of copper disks and Nb-Ti sheets were stacked to fill the void space from the end of the billet to the back of the nose-cone. This sandwich acted both as a getter and as a heat resistor to minimize heat flow to the billet. All the extrusion billets for this thesis were fabricated in a manner similar to this.

After welding, the billet was evacuated to $< 10^{-5}$Pa and temporarily sealed by cold forging ~50-100mm section of the pumpout tube, the final seal being made by welding over the seam. The flattened tube was swaged to ~2.5mm dia. to avoid interfering with the extrusion die (see below).

As outlined in Figure 1.8, an alternative processing route for the PREP powder was to fabricate a monofilament by extruding the as-mixed powder in a copper can. These conductors were fabricated by first pressing the blended powders in the can to prevent powder separation (see Chapter 3) and to increase the initial billet density. This latter point is especially important in order to avoid an irregular extruded filament due to an irregular collapsed billet. Also, it was found that, if the void space was excessive, the billet could collapse to the point that there was insufficient fluid to provide the hydrostatic pressure. In this case the billet stalled and extrusion ceased. It was found that uniaxially pressing the powders in the can under ~10-15ksi was usually sufficient to prevent these problems. Powders were pressed in the can, both with and without an external supporting sleeve. If no sleeve was used, the can tended to barrel during pressing; the original diameter was restored by pressing the can in a collet of appropriate size (a method which could also be used to straighten a slightly buckled billet). If an external sleeve was used to support the can, these problems were avoided. However, uniaxially pressing long lengths of powder results in a density gradient along the length of the billet. This density gradient would result in a variable core diameter along the length of the product. To avoid this, the powder was pressed in small ~5g increments whenever the outer support was used.

2.2.5 Extrusion

The step by step operation of the extrusion press can be found in the operation manual for the machine. What follows are the most important considerations taken in the extrusion of the billets for this thesis.

There are many ways to obtain the hydrostatic pressure required for extrusion. Our machine builds the pressure by decreasing the volume in the chamber by movement of the die stem, similar to reverse extrusion (Figures 2.2 and 2.4). A finite volume of fluid is loaded in the chamber just prior to extruding. Thus it was important to reduce the amount of void space in the extrusion billet to less than that of the extrusion fluid volume. Once the void space is minimized the remaining void space is estimated, and the billet length was adjusted to provide extra extrusion fluid to take up the void space produced when the billet collapsed. Observations of stalled billets suggested that complete void space closure occurred prior to extrusion. While some allowance for extra extrusion fluid was made, this technique was not always successful, especially when the amount of fluid required was large (whenever the volume change was equivalent to a length change >12mm). Apparently this occurred when the chamber did not seal immediately. For example, if the pumpout tube deflected the billet from the die centerline, the chamber tended to leak fluid from the die until the breach plug nudged the billet back to center. This was sometimes avoided by pretesting the die on the billet and swaging the pumpout tube down to ~2mm. A compound angle on the billet nose-cone (e.g., 35 and 40 degree half angles) also helped to seal the billet with the die (37.5 degree half angle).

Billet preheat was accomplished either in an external furnace or in-situ with the preheated chamber. All of the composites described in this thesis were preheated to ~250-300°C, either externally or in the chamber. Some development billets were preheated externally to as high as 650°C. This was done in a tube furnace under flowing argon while the billet was in a stainless steel loading tool. The lower preheat temperature was used because it allowed extrusion to the desired reductions (R~16-25) and minimized the potential for reaction between Cu and Ti. All preheats were for 15-20min. which was sufficient to equilibrate the billet to temperature. The time from loading to extrusion was less than 1 minute for the externally preheated billets. Once the billet was extruded, it was immediately water quenched to avoid precipitation of undesired second phases.

2.2.6 Multifilament Designs

In order to obtain the nanometer scale two phase microstructure, a strain of about 12-14 needed to be applied to the conductor. The maximum strain available from one extrusion and drawing process (from the initial 15.9mm to 80μm dia. final sized monofilament) is about 10.5; thus an additional processing step was needed. Typically in processing conventional Nb-Ti superconductors, the monofilament is drawn through a hexagonal die and cut into short lengths of wire. These hexagonal monofilaments are bundled into a close packed array and inserted into an extrusion can. We have adapted this process to our conductors by hexagonal drawing to 1.1mm across flats (AF) and bundling 91 filaments into a 15.9mm OD × 12.7mm ID copper extrusion can (Figure 2.8). Just as with the powder extrusion billets, it is important to minimize the void space. Thus flat copper shim stock roughly 0.4mm × 5mm × billet length was beveled to better fit the can and inserted along the flats of the filament bundle. This extra copper provided a good packing density. The subsequent second extrusion added ~5 to the available strain space.

An alternative process was developed to provide a monofilament after the second extrusion. The first extrusion monofilament was wire drawn to produce a Nb-Ti/Nb core diameter of ~1mm. After sectioning into short lengths, the copper was etched away to reveal the bare Nb-Ti/Nb composite core. Sections of these were bundled and extruded similar to the multifilamentary bundle, except that since there was no copper between the filaments, the filaments bonded to each other during extrusion to form a new monofila-

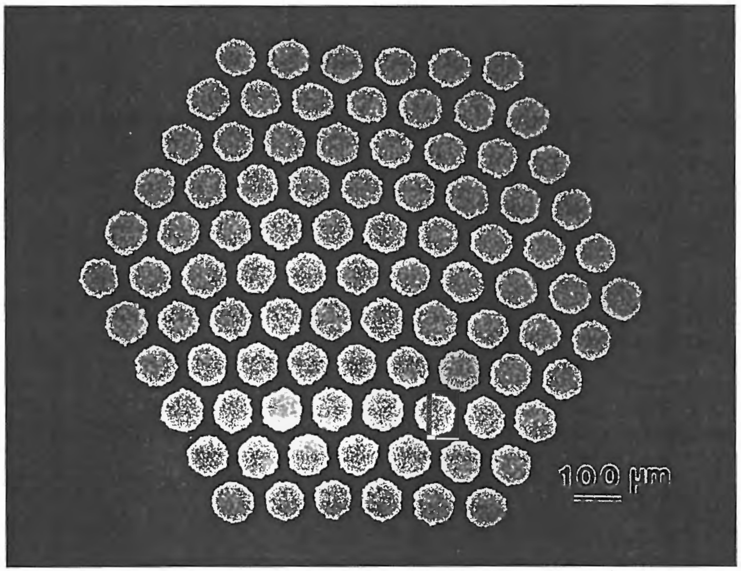

Figure 2.8: Micrograph showing the multifilamentary design used to produce 91 filament conductors.

ment (Figure 2.9). Some special considerations with this composite included approximating a round rather than a hexagon-shaped core to reduce the redundant work during extrusion. This was accomplished by substituting half hexagon copper pieces at the corners of the bundle. Thus a 91 filament core contained 85 superconducting pieces plus 6 half hex copper pieces. Also, since the round filaments did not stack as tightly as the hexagon drawn monofilaments, it was necessary to load the bundle in a custom machined can ~16.5mm × 10mm (i.e., a size that closely matches that of the bundle). The larger can diameter was useful since the can was precollapsed by placing it in a rubber CIP bag and pressing to ~35ksi. This pressing procedure eliminated much of the excess void space prior to extrusion.

Although much care was taken in producing these billets, both of these designs had "end effects" as did the initial monofilament. End effects are front and back sections of the wire which do not have the same geometry as the rest of the composite as a result of unstable flow at the beginning and end of extrusion. Nothing could be done to prevent these end effects from forming; thus they were cut from the composite by incrementally sectioning until a stable composite core diameter was obtained. Subsequently, standard wire drawing procedures were used to fabricate the composite to the desired size.

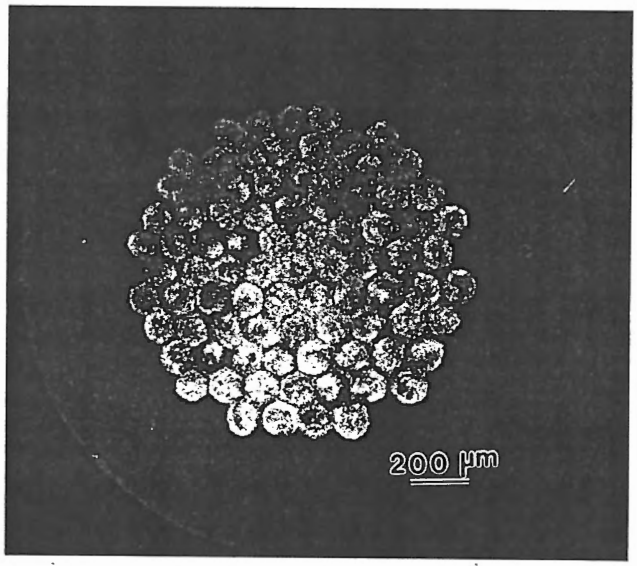

Figure 2.9: Micrograph showing the typical structure of a bundled filament conductor created by bundling and extruding 85 bare Nb-Ti/Nb filaments and 6 Cu half hex pieces together in a 91 filament bundle. Note that the Nb-Ti/Nb bundle essentially forms a new monofilament core.

2.3 Summary

The goal of this thesis was to develop two-phase nanostructures in composites (mono- and multifilamentary) from powder mixtures. Two essential steps of the process were to ensure that the powders were well mixed and were processed into a billet. To accomplish this, composites were extruded, drawn to wire, restacked, extruded a second time and drawn to final size wire comprised of a two-phase nanostructure contained within a copper sheath. The whole process of billet/wire fabrication was developed for this thesis and is described in detail in this chapter. This development required much trial and error. The two following chapters discuss further process refinements in more detail.

Chapter 3

Sources of Early Composite Failures

During the course of this thesis nearly 100 PM APC billets were fabricated and extruded. Each final composite billet required two extrusions, thus making nearly 50 superconducting composites in all. Many of these composites were tests of various aspects of the fabrication process. As Chapter 2 has shown, there are many steps in the fabrication of a complex superconducting composite with a nanometer scale artificial pin structure. The main body of this thesis concentrates on just five of these composites. This chapter summarizes key aspects of the process development required to make the process feasible.

3.1 Powder Characterization

Two different types of starting powders were used; PREP (Plasma Rotating Electrode Process[53, 54]) Nb-55wt%Ti ($< 180\mu m$) or hydride-grind-dehydride (HGD) Nb-47wt%Ti (45-120μm) for the matrix and HGD Nb (45-75μm) for the pinning center. The starting powder shapes are quite different, due to their very different fabrication. Being melted to shape[53], the PREP powder (Figure 3.1) was slightly rough but spherical. Cross sections revealed a dendritic structure with perhaps some unmelted regions. The individual PREP powder particles are apparently single grained. The HGD Nb-Ti and Nb pinning center powders were angular in shape (Figure 3.2) owing to the mechanical grinding used to powder the material. The HGD powders were polycrystalline, typically containing a few grains per particle. According to Table 3.1, the oxygen content of Nb-55wt%Ti powder was 1120ppm, within the range common for Nb-55wt%Ti ingots while the oxygen in the HGD Nb-Ti was ~2-3 times that observed in typical ingots of Nb-47wt%Ti. The 670ppm oxygen seen in the Nb is about an order of magnitude higher than normally obtained in ingot Nb. Nevertheless, the oxygen contents did not appear to adversely affect the drawability of the composites.

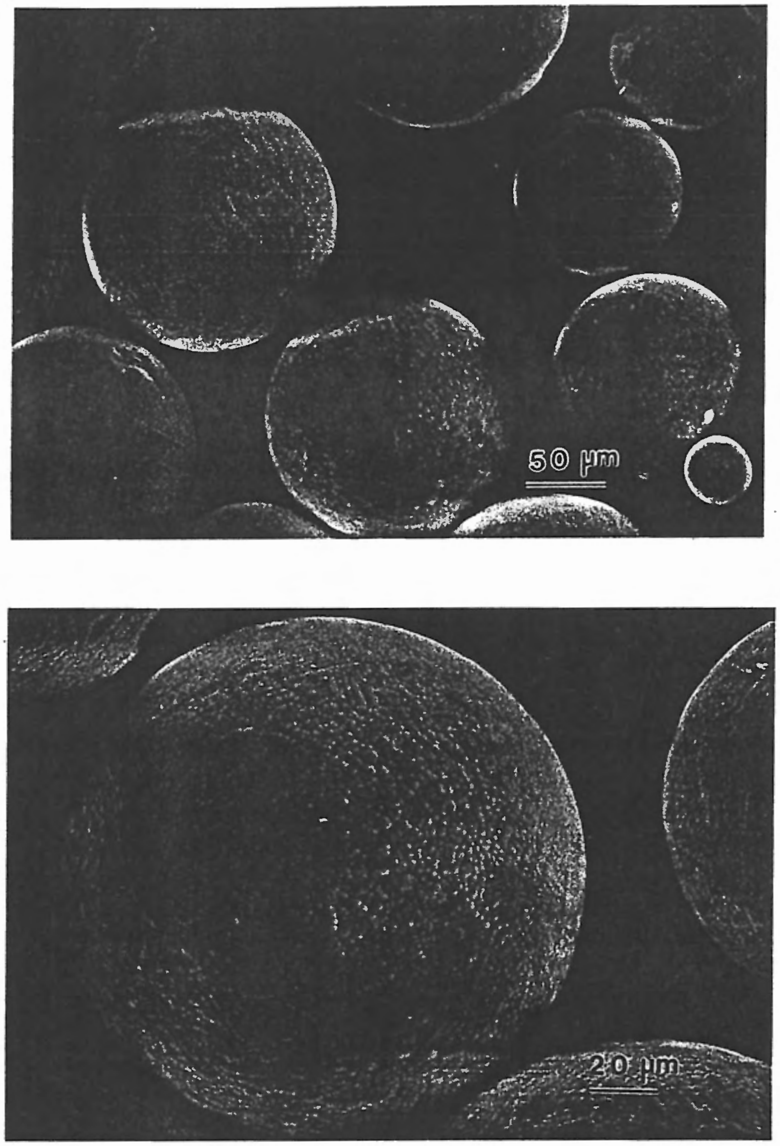

Figure 3.1: SEM secondary electron image of the PREP Nb-55wt%Ti powder used as matrix material (a) and SEM backscatter electron image of a powder cross section after etching lightly (b).

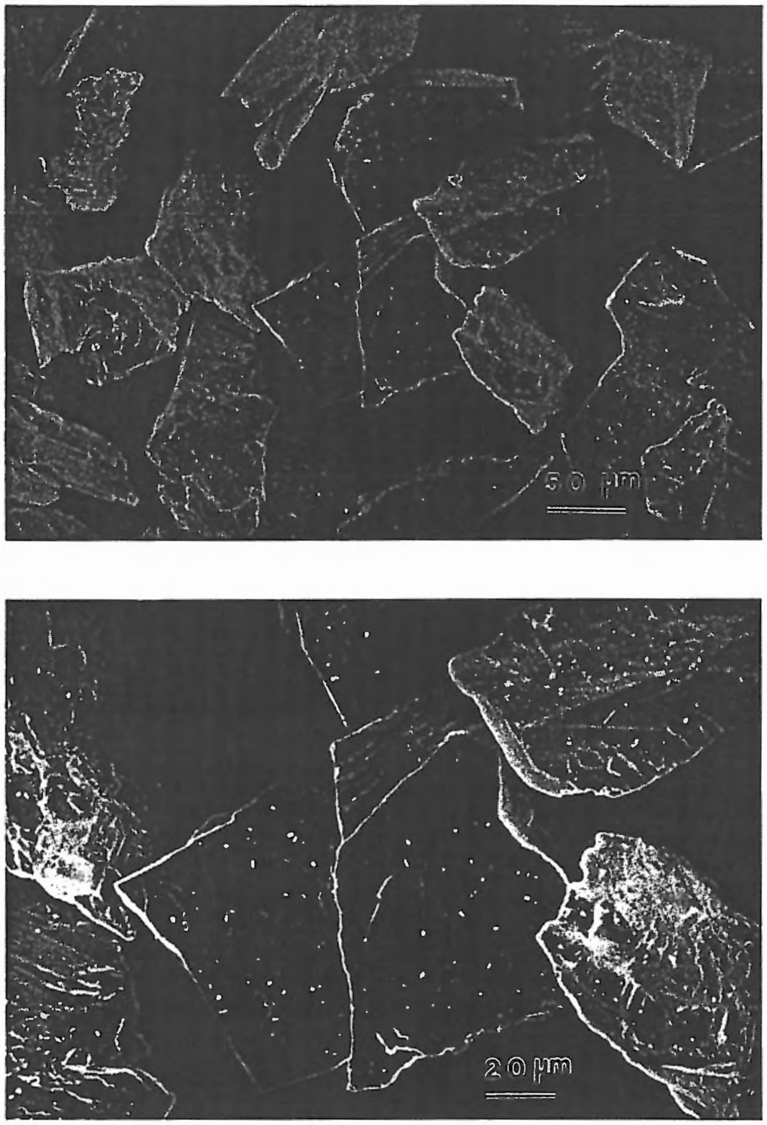

Figure 3.2: SEM secondary electron image of the Nb powder used as pinning center material.

Table 3.1: Powder chemical analysis.

Powder	Analyzed values (ppm)			
	H	N	O	C
Nb-55wt%Ti	8	220	1120	80
Nb-47wt%Ti	160	92	1880	92
Nb	8	30	670	< 30

3.2 Composites Fabricated from Hydride-Grind-Dehydride Nb-Ti Powders

Two pre-sintered ~200g billets of HGD Nb-47wt%Ti and Nb powders with 20 and 40 volume percent second phase were used to fabricate 8 composites. These monofilaments provided the material for a series of multifilamentary composites. The process outline, including diameters and strains, is given in Figure 3.3. The first pair of 91 filament composites failed at 1.1mm dia. ($\epsilon \sim 10$), far from final size. Failure analysis showed that individual filaments fractured, which in turn broke adjacent filaments and then the wire. Metallography revealed anomalously hard particles (see below).

Auger electron spectroscopy (AES) was used to identify these hard par-

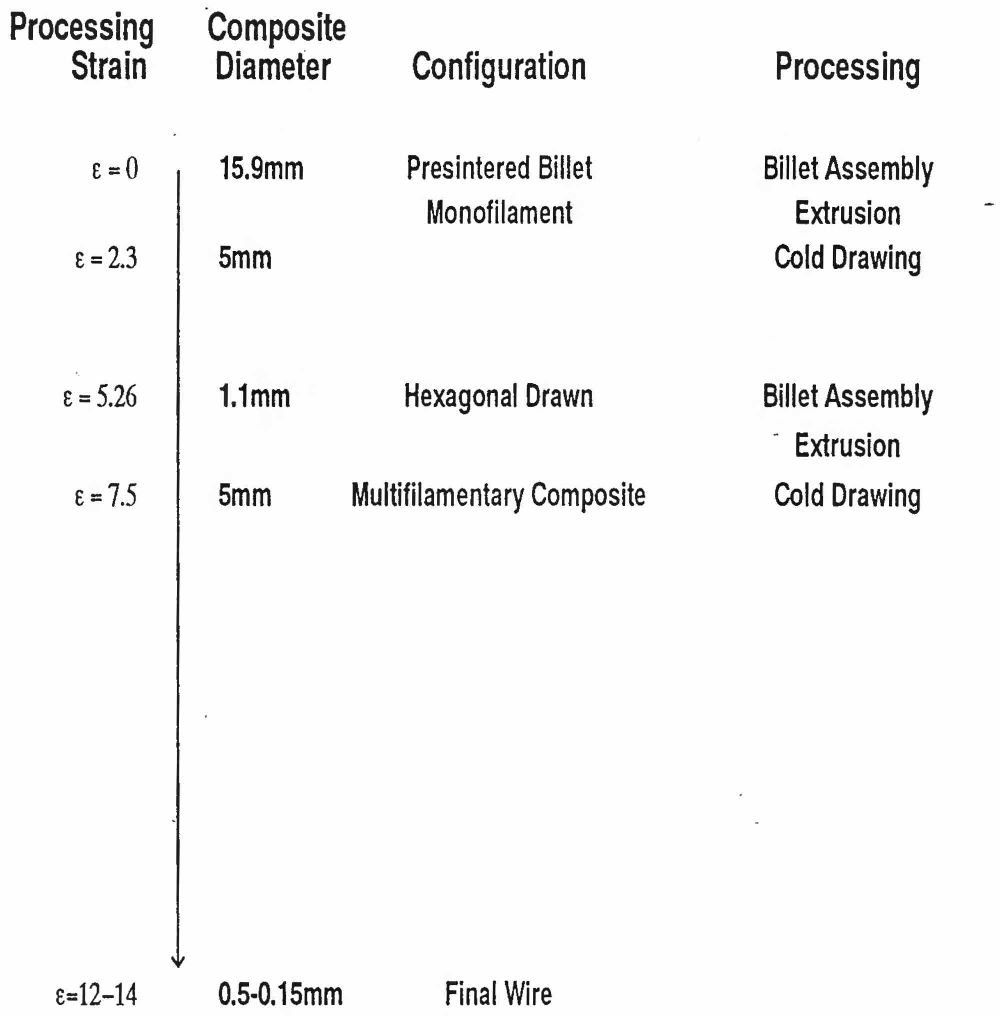

Figure 3.3: Flow chart showing an outline of the PM fabrication route.

ticles since they were suspected to be some type of oxide. The AES results showed that the inclusions contained Ni, Fe, and/or V (Figures 3.4 and 3.5). No obvious source for these foreign particles could be found in our lab; thus we considered whether they were introduced by the manufacturer, perhaps during the grinding operation.

If the transition metals were incorporated during the grinding operation, it is likely that at least some were contained within the starting metal powder particles. Thus simple separation techniques such as sieving would not be effective. Since 6 monofilament rods of the two compositions remained, these were used to evaluate other techniques to eliminate the inclusions. Diffusion calculations were made to evaluate the viability of solutioning the transition metal inclusions without destroying the Nb pinning centers. These calculations were based on the diffusivity of Fe in Nb-Ti alloy[105] since Fe was found to be the slowest diffusing of the inclusion species. These calculations predicted that a solution heat treatment of 1175°C/2h would redistribute the Fe $\sim 200\mu m$ into the surrounding Nb-Ti matrix without adversely affecting the Nb pinning centers (diffusion of any of the metals into Nb is limited only a few nanometers). This treatment should completely solution the inclusion particles which were typically 10-50μm in diameter. No hard particles were observed metallographically after the post extrusion heat treatment.

Multifilamentary composites, subsequently fabricated from solution

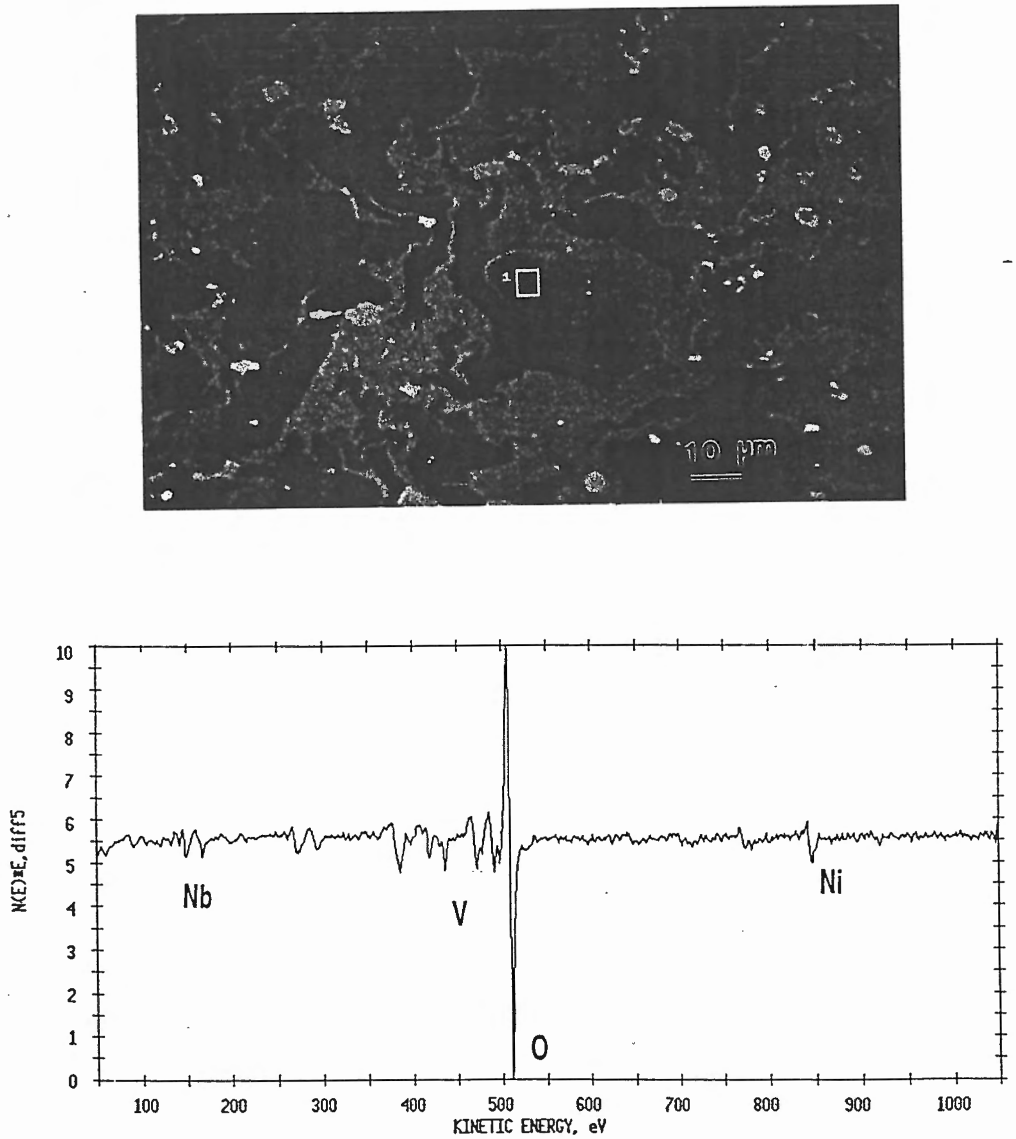

Figure 3.4: Backscatter electron micrograph and auger electron spectroscopy on typical non-deforming inclusion.

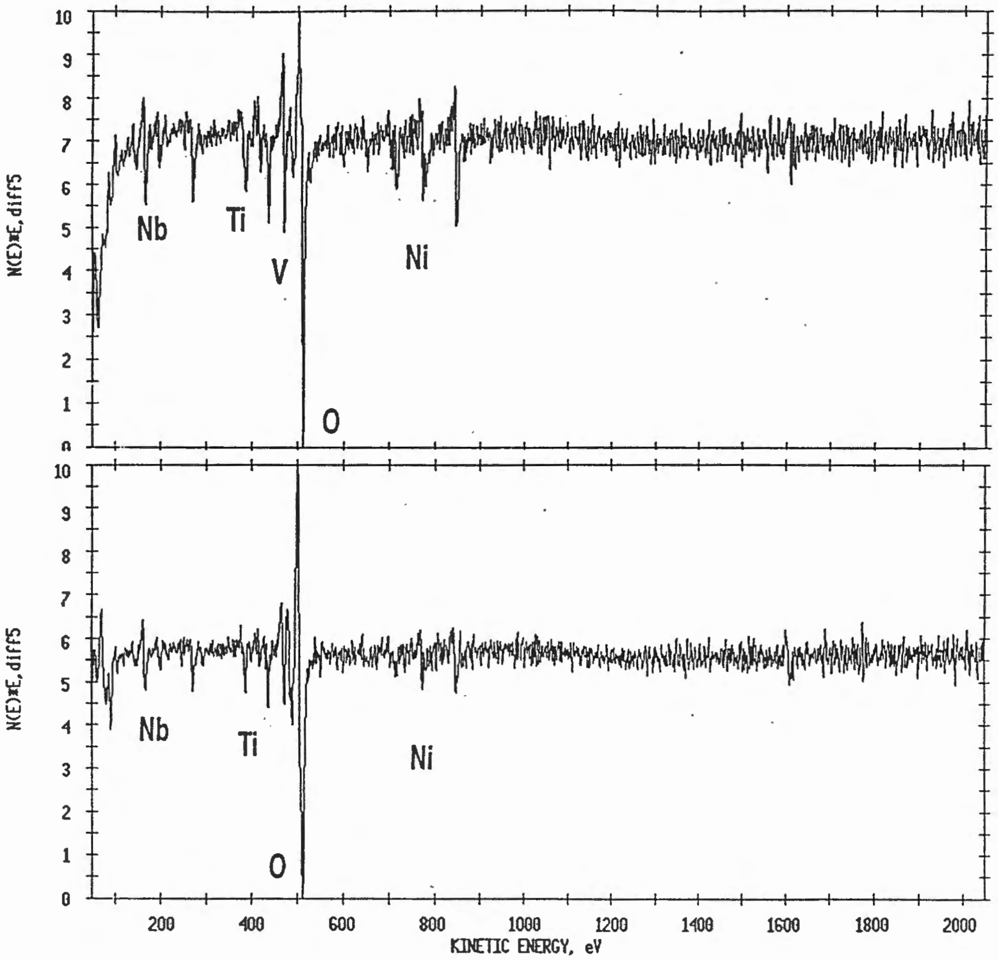

Figure 3.5: Auger electron spectroscopy of other typical non-deforming inclusions.

treated rods, were processed to final size, but not without broken filaments. The source of the broken filaments was traced to angular particles which were found to be Zr-rich by Energy Dispersive Spectroscopy (EDS, see Figure 3.6). We believe these to be ZrO_2, rather than Zr, by virtue of their hardness and angular shape. It is noteworthy that ZrO_2 is favored over Ti_xO_y and Nb_xO_y oxides because of the higher ΔG of formation[36]. Thus, during the sintering and solutioning thermal cycles Zr may actually be gettering the oxygen from the surrounding matrix, further hardening the Zr particles. Once again there was no obvious source for the zirconium in our lab; thus it was suspected that the starting powders were contaminated with Zr, since Zr powder is also processed by the HGD powder vendor.

3.3 Composites Fabricated from PREP Nb-Ti Powders

The conclusion to be drawn from the preceding section was that a change in powder source was required if further improvements were to be made. PREP Nb55Ti was obtained courtesy of I. Donahue at Nuclear Metals. The PREP powder is spherical (Figure 3.1). As discussed in Chapter 2, the PREP powder (including mixtures with HGD Nb) does not hold its shape when pressed and thus cannot be pressed and sintered like the hydride-dehydride

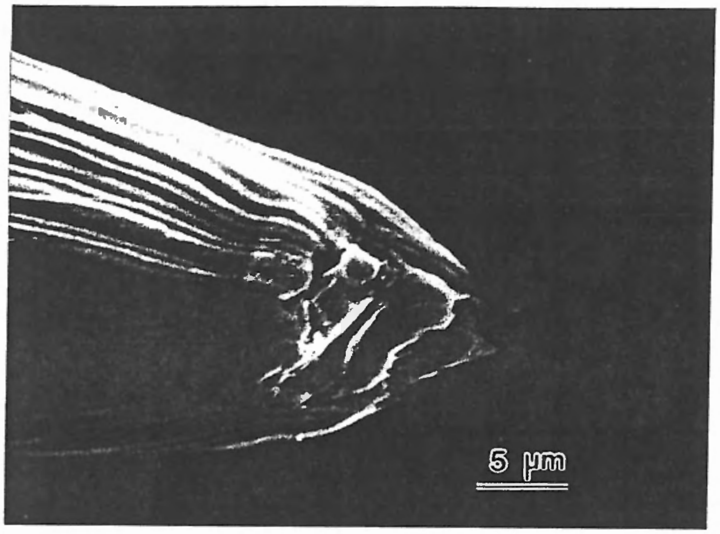

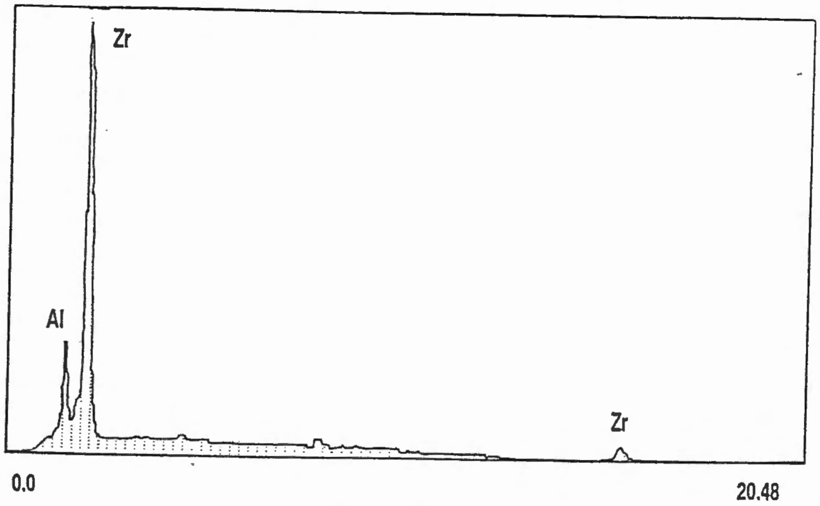

Figure 3.6: Secondary electron image of an extracted filament fracture surface. Energy dispersive analysis of the fracture surface shows that it is essentially a zirconium particle (note that the aluminum peak is from the sample holder).

powder. Fortunately the extrusion press provided an alternate processing route. In the first test billet, a loose mixture of PREP Nb-Ti and HGD Nb powders was canned and extruded. Unfortunately, the loose packing provided significant freedom of movement for the powders and the Nb was observed to segregate to about mid radius (Figure 3.7). In subsequent billets the powder mixture was uniaxially pressed directly in the can, as outlined in Chapter 2 which successfully prevented the gross segregation observed in Figure 3.7.

Several PREP-based conductors containing 20 or 40 volume percent niobium were processed without any heat treatment other than the 250-300°C/15min preheat for extrusion. The composites which contained 20-vol%Nb drew to final size; however, many wire fractures were encountered as the wire neared final size. Composites which contained 40vol%Nb were not fabricable past the monofilament stage. These wire breaks were again traced to broken filaments. Metallography showed that there were some Nb particles which were non-deforming (Figure 3.8), consistent with the increased difficulty drawing the 40vol%Nb conductors. Since the Nb powder was fabricated by the HGD process, there are many potential opportunities for contamination by interstitial impurities. For example if the dehydride atmosphere was slightly oxidizing (the ΔG for the formation of Nb_xO_y is much larger than that for H_2O formation) some of the Nb would be contaminated.

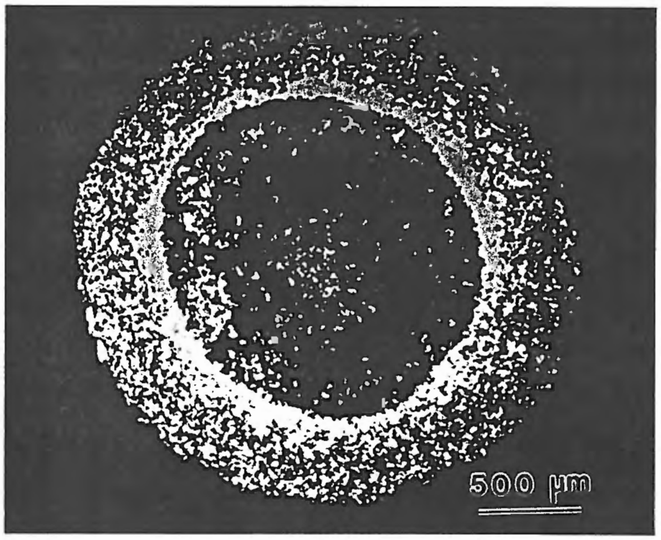

Figure 3.7: Backscatter electron micrograph showing the gross segregation of Nb powder to about mid-radius in a composite extruded from loose powder.

Oxygen is the slowest diffusing interstitial contaminant[105]. Thus an estimate was made of the diffusion distance required for the oxygen to escape the Nb particles. This estimate predicted that an 800°C/2h heat treatment would allow the oxygen to diffuse ~170μm which is about 3 times the size of the Nb particles. Thus a heat treatment was given to the Nb-Ti/Nb rods after the first extrusion in order to redistribute the interstitial oxygen. This process relies not only on diffusivity, but also on the property that the oxygen and other interstitials have a higher activity in Nb than the Nb-Ti alloy[36]. Upon application of this post extrusion heat treatment, non-deforming Nb particles were no longer observed, and several multifilament conductors were processed without wire failures. However, broken filaments were observed upon etching the copper matrix away even when no wire breaks occurred. Hard Zr(O?) particles were again observed similar to the one shown in Figure 3.6.

It is unlikely that the PREP powder was the source for the angular Zr particles because it was fabricated by melt processing. This shifted attention to the Nb powder. A Nb powder cleaning process, aimed at eradicating the zirconium, was then instituted (the details of this process have been left out pending patent approval). In addition to the powder cleaning process, a method of identifying sections of conductor without broken filaments was needed. This led to the bundled bare filament second extrusion (Figure

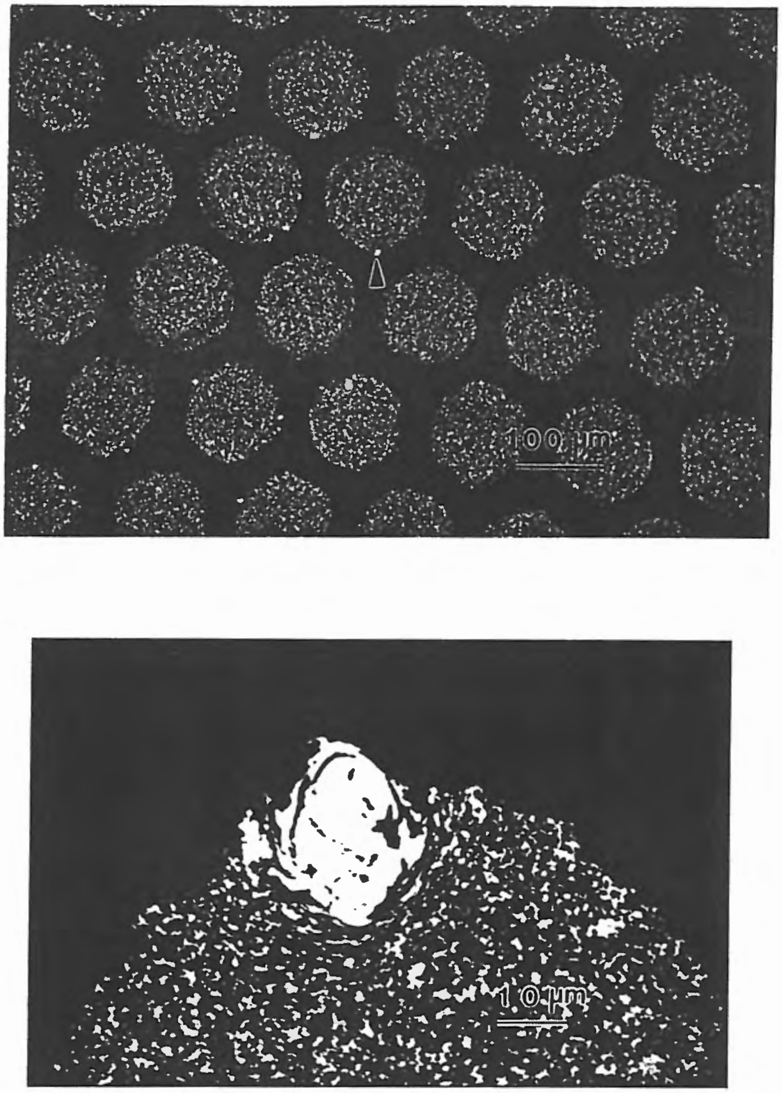

Figure 3.8: Backscatter electron micrograph showing non-deforming particles typically observed in PREP + Nb conductors which received no extra heat treatments. These particles were identified as Nb by EDS.

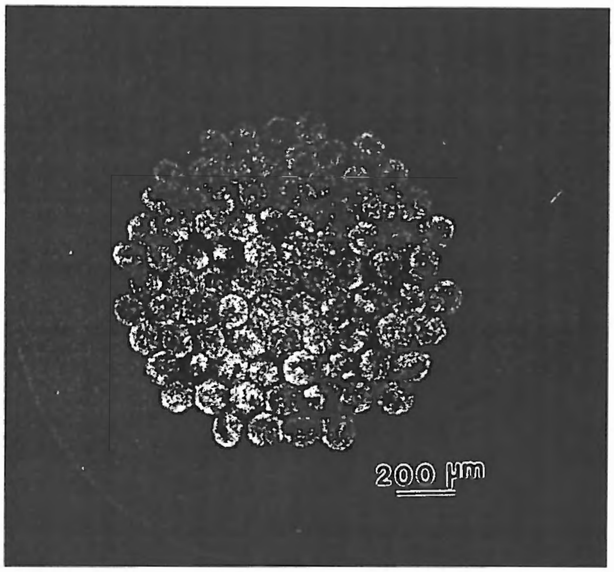

Figure 3.9: SEM secondary electron image showing the overall structure of bundled filament composite.

3.9). It was anticipated that when one of the original filaments failed, it would cause the filament bundle and conductor to fail at the same time, thus selecting uniform, defect free material for J_c testing.

Some filament breaks did occur, but this time the composites broke *every* time a filament failed. Failure analysis performed on these composite failures did not reveal the source of fracture. It was observed that the failures tended to occur late in the drawing schedule, and that the occurrences tended to increase with the amount of Nb added. This coincided with an increase in hardness and hardening rate (see next chapter). The majority of failures occurred once the Nb-Ti/Nb hardness reached about 300kg/mm^2.

3.4 Summary

Some of the difficulties associated with powder impurities have been described in this chapter. In attempting to develop the process we worked with commercially available powders produced by two very different processes. It appears that the HGD powders were contaminated. In other respects, for example their angular, polycrystalline nature, these powders were very suitable for the process. In this respect the PREP powders were less suitable but they were not contaminated. An additional variant of the composite fabrication process was developed to accommodate the low green strength of the pressed PREP powder. Composites were successfully fabricated to nanostructure dimensions from both types of powder.

Chapter 4

Mechanical Properties and Drawability Improvements of the Composites

Chapter 3 discussed the improvements made by removing or avoiding impurity particles and bundling filaments. In this chapter we discuss the wire breaks associated with the parameters of the wire drawing sequence itself. The die sequence/angles are fixed by the available dies which were established to some extent by prior practice on conventional Nb-Ti/Cu composites. We noticed many wire breaks near optimum size (when the microstructure becomes nanometer scale). We wanted to know how the breaks correlated to the stress-strain curves of the composites and whether there were additional parameters which could be varied to improve drawability.

4.1 Billet Fabrication and Experimental Procedure

The pressed powder extrusion process was used to fabricate the conductors described in the remainder of this thesis. Chapter 2 describes the details of this process while Chapter 3 describes how we eliminated filament and conductor fractures by: a) changing to PREP Nb-55wt%Ti for the matrix powder, b) eliminating the Zr particles from the HGD Nb powder, and c) instituting a post extrusion heat treatment to redistribute oxygen from the contaminated Nb particles. To fabricate the composites the appropriate amounts of powders were weighed, blended and pressed into 15.9×12.7mm (OD×ID) copper extrusion cans to produce composites of Nb-55wt%Ti + 10-40vol%Nb in steps of 10vol%Nb (Table 4.1). These composites are further characterized in Chapters 5 and 6. The billets were evacuated to $< 10^{-5}$ Pa, sealed and final machined for extrusion at 250°C and an area reduction ratio of 25 ($\epsilon \sim 3.22$). The copper was etched off the extrudate before heat treating at 800°C/2h. The Nb-Ti/Nb composite rods were each sheathed in copper, drawn into 1.5mm diameter wire and cut into 85 pieces. The copper was again etched off before bundling the filaments into another extrusion can.

Table 4.1: Compositions of Composite Billets

vol%	ID	wt. Nb-55wt%Ti	wt. Nb
10	P21P	42.80g	7.20g
20	P22L	39.88	15.12
30	P23H	30.30	19.70
40	P24C	24.85	25.15

The copper/bundled filament composite was extruded similar to above (reduction ratio of ~16). The process outline, including diameters and strains, is given in Figure 4.1.

Vicker's hardness tests were performed on as-polished transverse composite wire cross sections of the monofilament and bundled filament conductors. Wire samples were taken in steps of $\epsilon \sim 1$. Sampling of the monofilaments and bundled filaments were overlapped in order to evaluate the effect of extrusion on the hardness and hardening rate. Hardness tests were performed using a 200g load and 15s dwell time on all but the coarsest microstructures, in which case a 500g load was used so as to sample the composite microstructure as a whole, rather than that of the individual phases. The data presented are averages of 5 indents per wire diameter.

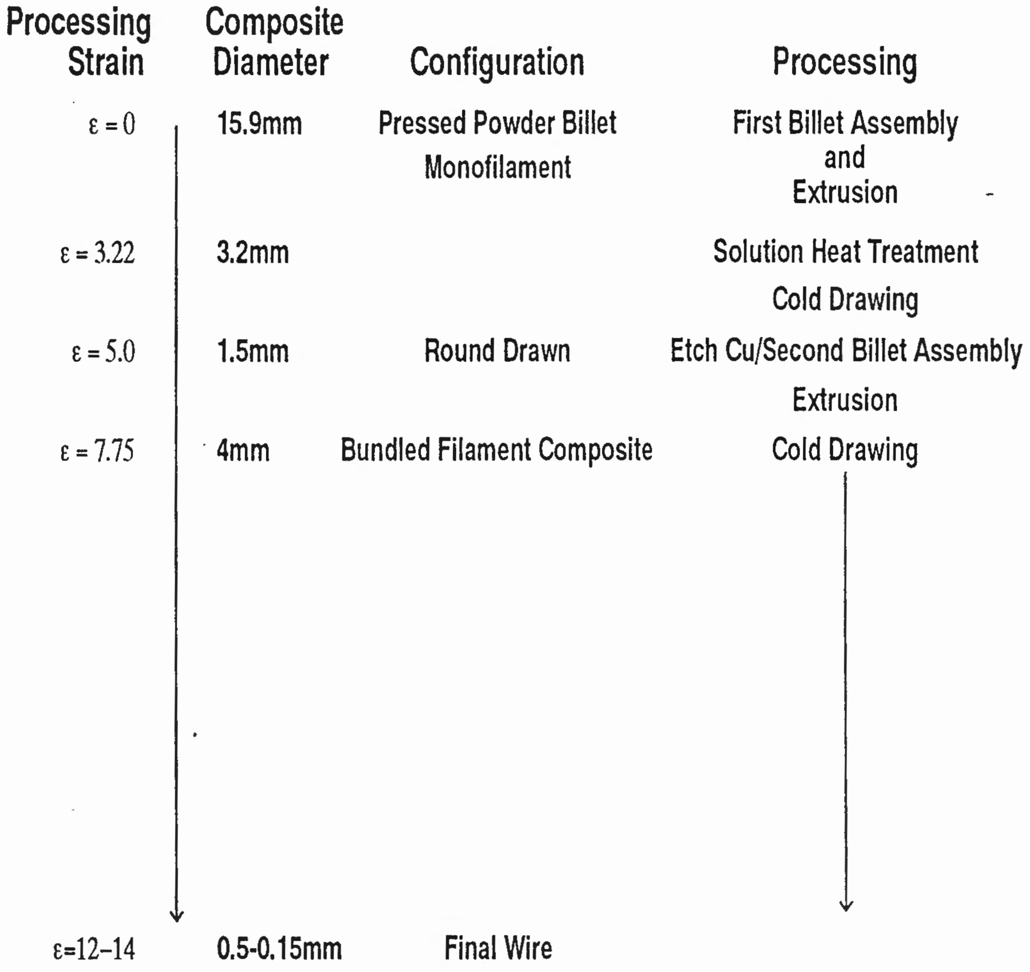

Processing Strain	Composite Diameter	Configuration	Processing
$\varepsilon = 0$	15.9mm	Pressed Powder Billet Monofilament	First Billet Assembly and Extrusion
$\varepsilon = 3.22$	3.2mm		Solution Heat Treatment Cold Drawing
$\varepsilon = 5.0$	1.5mm	Round Drawn	Etch Cu/Second Billet Assembly Extrusion
$\varepsilon = 7.75$	4mm	Bundled Filament Composite	Cold Drawing
ε=12–14	0.5-0.15mm	Final Wire	

Figure 4.1: Flow chart showing an outline of the pressed powder billet fabrication route.

4.2 Vicker's Hardness Results

Figures 4.2-4.5 show H_v vs. ϵ for the various composites. The general trend for all the composites is continued work hardening with increasing strain. H_v started at ~130-160kg/mm^2 after extrusion (ϵ~3.2), rising to ~250-330kg/mm^2 at ϵ~13. Some recovery (~30kg/mm^2) was observed after the second extrusion, but the hardness quickly rejoined the underlying trend, just as it did after the first extrusion and heat treatment. Note that the monofilament and bundled filament results overlap for all of the composites. Two regression analyses were performed. A linear equation in strain

$$H_v = A + B \times \epsilon \tag{4.1}$$

was used in order to estimate the zero strain hardness which gives an indication of the powder quality. Figure 4.6 shows a comparison of the linear regression results. The general trend is that the higher volume percent composites have a lower initial hardness and a higher hardening rate. Thus, below a strain of about 6, the 10vol% Nb conductor was hardest, whereas beyond ϵ~6 the reverse was true. The zero strain hardness ranged from 130-165kg/mm^2 (Table 4.2), typical of annealed conventional Nb-Ti ingots.

The Hollomon [42] equation:

$$\sigma = K\epsilon^n \tag{4.2}$$

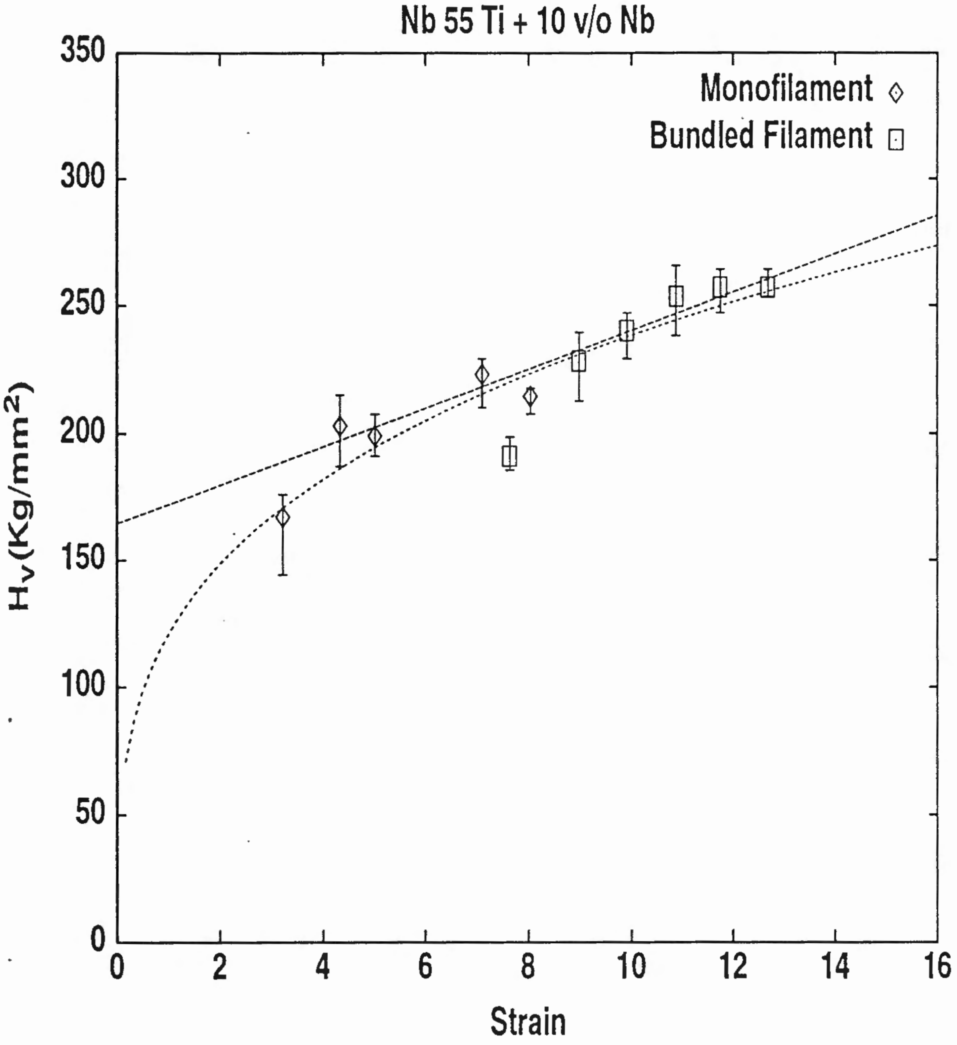

Figure 4.2: Vicker's hardness vs. strain for the Nb 55 wt% Ti + 10 vol% Nb conductor (symbols) and range of data (bars) along with linear regression and Hollomon equation ($H_v = K\epsilon^n$) fits to the data.

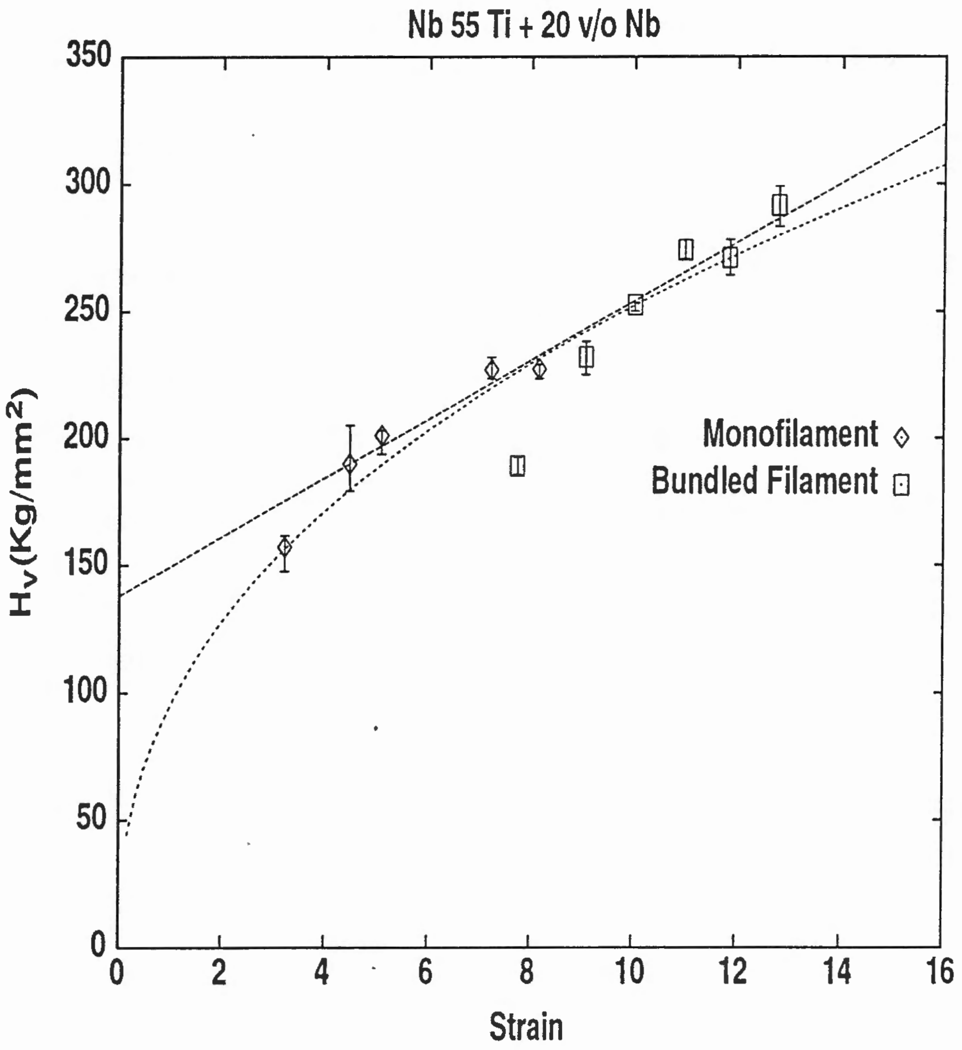

Figure 4.3: Vicker's hardness vs. strain for the Nb 55 wt% Ti + 20 vol% Nb conductor (symbols) and range of data (bars) along with linear regression and Hollomon equation ($H_v = K\epsilon^n$) fits to the data.

was also evaluated, where K is the material strength coefficient and n is the work hardening rate. As seen in Figures 4.2 through 4.5, eqn. 4.2 fits the data quite well. In addition, the usefulness of eqn. 4.1 now becomes apparent since eqn. 4.1 predicts a finite hardness at ϵ=0 while eqn. 4.2 predicts a zero hardness. The Hollomon equation will be used in the wire drawing equations to follow.

Table 4.2: Coefficients to Eqn. 4.1 and 4.2

	Eqn. 4.1		Eqn. 4.2	
vol%Nb added	A	B	K	n
10	164.5	7.55	121.0	0.294
20	137.9	11.6	95.4	0.422
30	118.2	15.0	85.5	0.496
40	127.5	14.2	75.6	0.548

4.3 Wire Drawing Results

Even though we avoided inclusions by selecting PREP Nb-Ti powders and eliminating Zr from the HGD Nb powders (Chapter 3), wire fractures still occurred. The majority of the fractures occurred on the "fine" wire bench

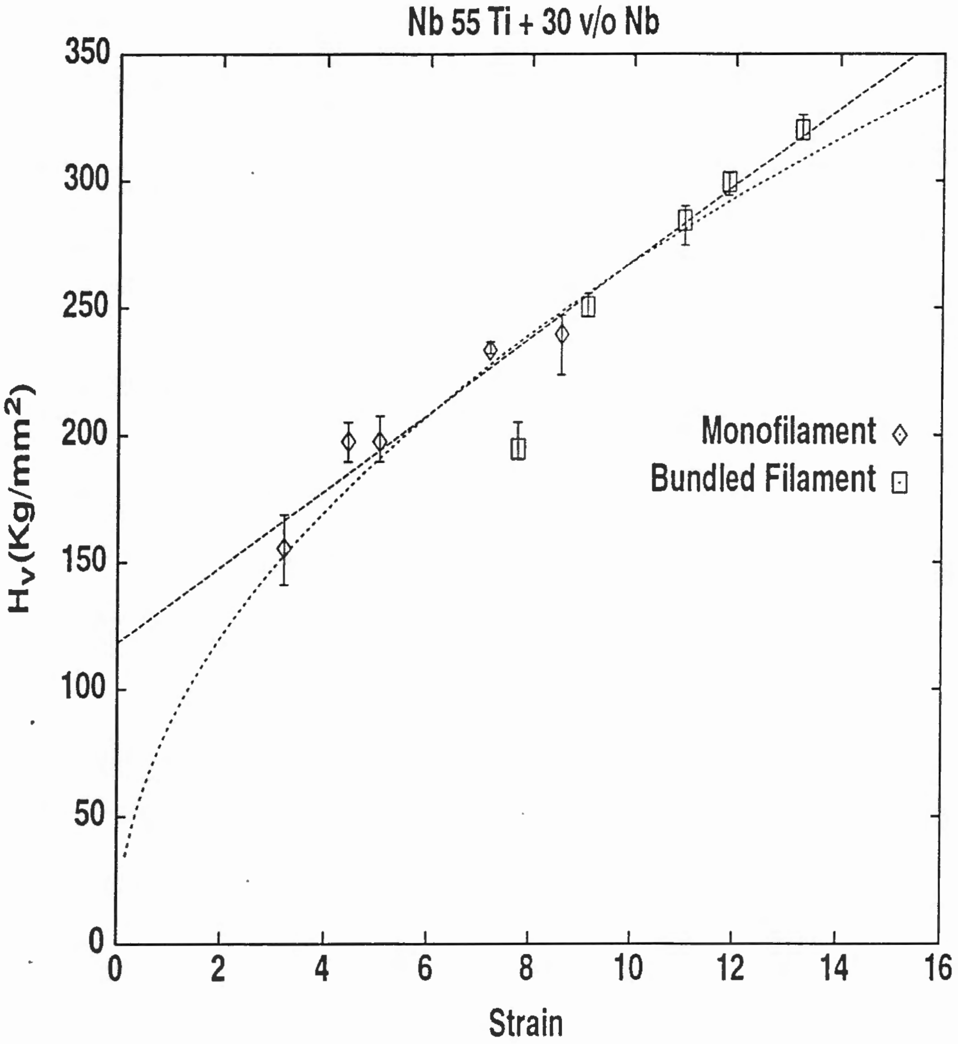

Figure 4.4: Vicker's hardness vs. strain for the Nb 55 wt% Ti + 30 vol% Nb conductor (symbols) and range of data (bars) along with linear regression and Hollomon equation ($H_v = K\epsilon^n$) fits to the data.

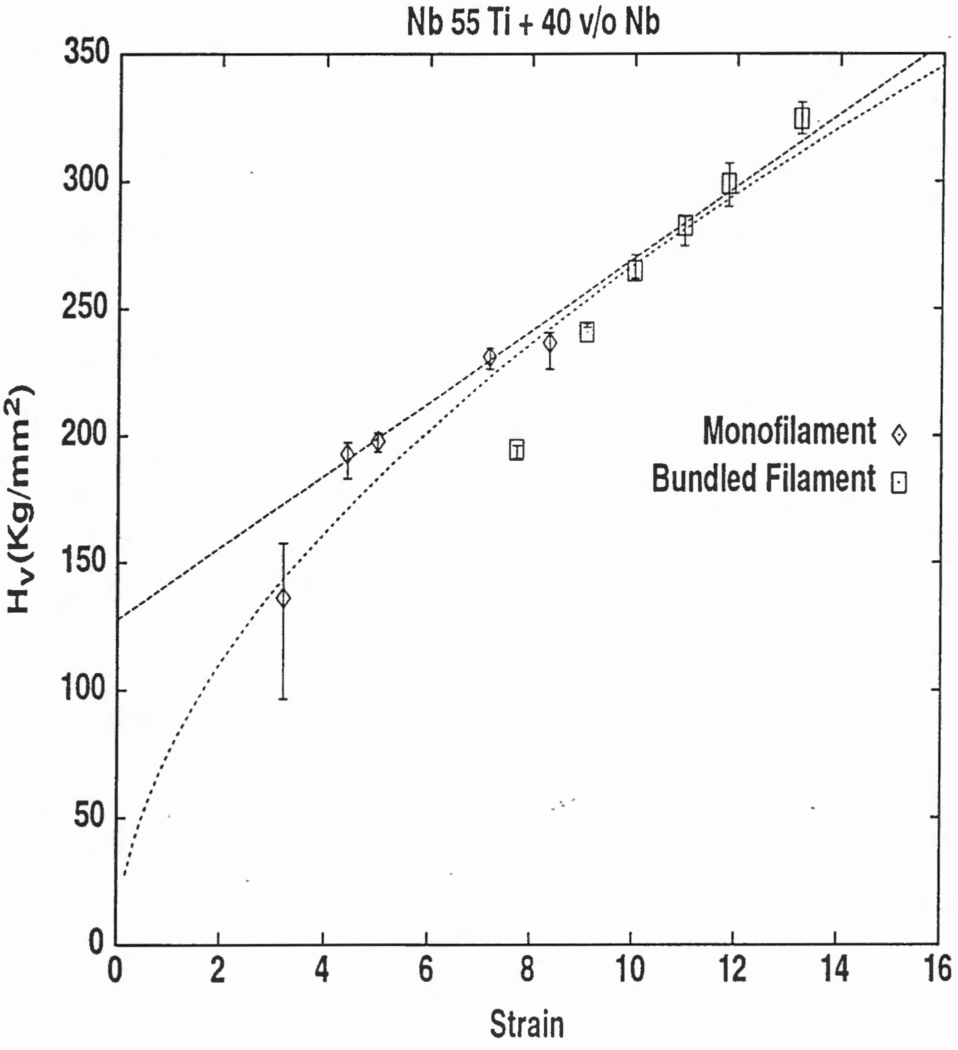

Figure 4.5: Vicker's hardness vs. strain for the Nb 55 wt% Ti + 40 vol% Nb conductor (symbols) and range of data (bars) along with linear regression and Hollomon equation ($H_v = K\epsilon^n$) fits to the data.

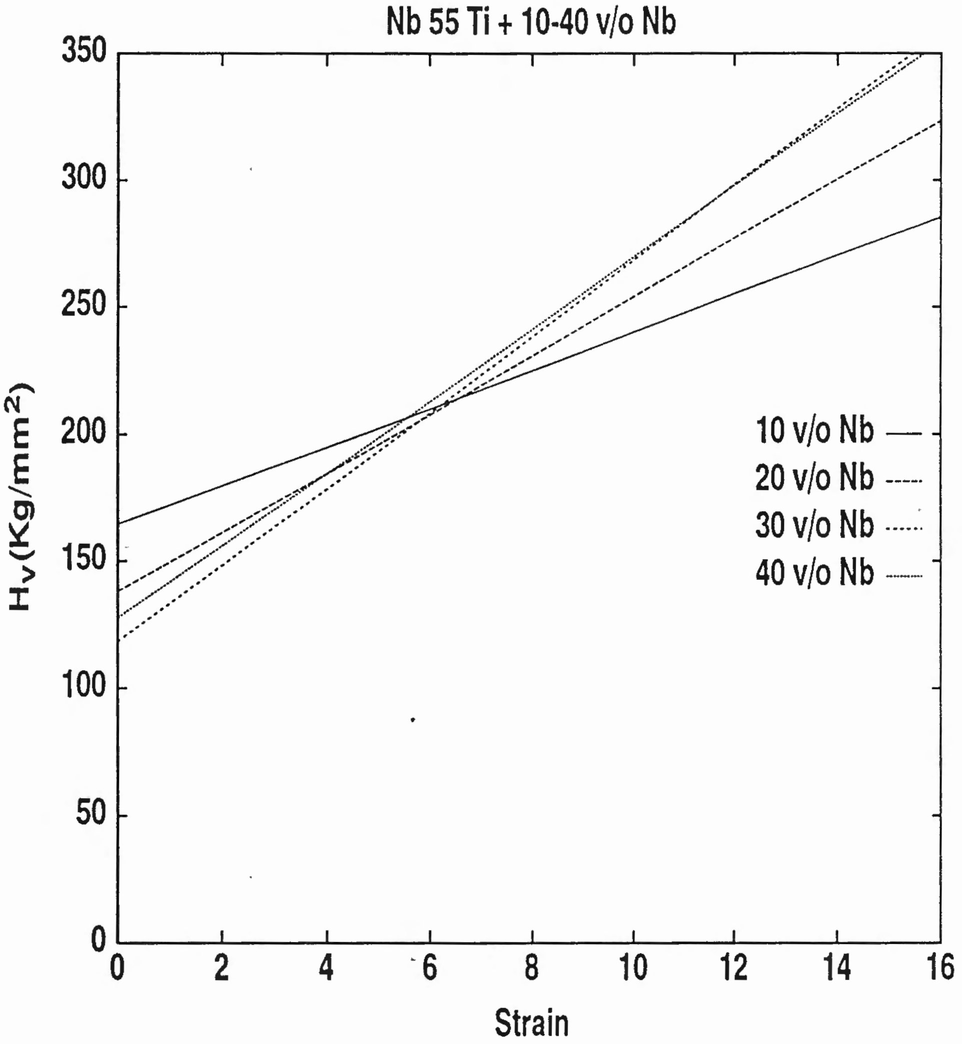

Figure 4.6: Vicker's hardness vs. strain for the Nb 55 wt% Ti + 10-40 vol% Nb conductors. Composite identification is given in the figure and the linear regression coefficients are given in Table 4.2.

where the wire diameter is <0.3mm and the composite strain was ~13. However, the frequency of wire breaks and thus difficulty of drawing tended to increase as more Nb was added to the Nb-Ti powders. Thus the 40vol%Nb conductor experienced wire breaks at diameters as large as d~0.8mm and strains of $\epsilon \sim 11$.

A series of investigations were commenced to determine the source of these wire breaks. These included light microscopy and scanning electron microscopy on polished wire cross sections, fractography of broken wire pieces and a SEM examination of the bare bundle surfaces. None of these evaluations revealed the source of the wire fractures. Thus we turn to predictive wire drawing equations and evaluate them in light of our reduction schedule and material properties.

4.4 Discussion

In the following section we will attempt to correlate the wire drawing experiences with the mechanical property measurements. For a monolithic material, the drawing stress (σ) normalized to the material strength coefficient (K') is

$$\frac{\sigma}{K'} = \frac{\left(\epsilon + \ln\frac{1}{1-r}\right)^n}{n+1} \ln\frac{1}{1-r} \left(0.8 + \frac{\alpha}{4.4r}\left[1 + (1-r)^{0.5}\right]^2\right)(1 + \mu\cot(\alpha)) \tag{4.3}$$

(after [13, 52, 121, 122] as presented in Dieter [22]) which includes material parameters, redundant work parameters and friction factors. If we take a slightly modified Hollomon equation ($K' = K/(n+1)$), we can directly compare the material flow stress to the drawing stress for our wire drawing scheme (i.e., reduction in area per die, $r = 0.20$; die half angle, $\alpha = 6°$; and n given by eqn. 4.2)

$$\frac{\sigma}{K'} = \frac{\epsilon^n}{n+1} \tag{4.4}$$

Since all of the terms in eqns. 4.3 and 4.4 are set by material or drawing parameters, we can solve for the critical friction factor (μ^*), above which fracture is favored over wire drawing. Thus the critical friction factor is given by

$$\mu^* = \frac{\left(\epsilon + \ln\frac{1}{1-r}\right)^n \ln\frac{1}{1-r}\left(0.8 + \frac{\alpha}{4.4r}\left[1+(1-r)^{0.5}\right]^2\right) + \epsilon^n}{\ln\frac{1}{1-r}\left(0.8 + \frac{\alpha}{4.4r}\left[1+(1-r)^{0.5}\right]^2\right)\cot\alpha\left(\epsilon + \ln\frac{1}{1-r}\right)^n} \tag{4.5}$$

If the prestrain (ϵ) is large compared to the strain from wire drawing ($\epsilon{\sim}0.2$ per pass), the equation simplifies slightly to

$$\mu^* = \frac{\ln\frac{1}{1-r}\left(0.8 + \frac{\alpha}{4.4r}\left[1+(1-r)^{0.5}\right]^2\right) + 1}{\ln\frac{1}{1-r}\left(0.8 + \frac{\alpha}{4.4r}\left[1+(1-r)^{0.5}\right]^2\right)\cot\alpha} \tag{4.6}$$

and thus is *independent* of material parameters and only depends on the drawing schedule. For our drawing schedule μ^* evaluates to 0.28. Note that eqn. 4.6 does not depend on strain or the strain hardening exponent n or any other material parameters; thus it cannot explain the wire fractures encountered unless something changes to increase friction from below μ^* to above μ^*. Changes in μ do occur. For example three different drawing lubricants are used. Dry soap flakes are used for lubricant at the fine wire stage ($d \leq 0.284$mm) where the majority of fractures occurred. It is reasonable to suspect that the soap flakes have a lesser lubricating ability than the oily solutions used at larger sizes. In addition, the amount of lubricating action is likely to vary during drawing because the wire will pick up variable amounts of soap flakes as it enters the die. Unfortunately, handling fine wire is very difficult and using a fluid lubricant would further complicate the process because the tape used on wires on the take up reel would no longer adhere to the wire. This would likely lead to wire entanglement. Thus the main advantage of the dry soap flakes is the ease in wire handling. An individual die may cause problems if the bearing surfaces have become rough or some residual metal remains after a previous drawing sequence. Some of these problems have been encountered in the past and were identified by inspecting the die or wire (preferably both). Lastly, friction may change with wire size, perhaps as a result of the increasing surface to volume ratio.

Equations 4.3 and 4.4 were compared assuming a monolithic Nb-Ti/Nb composite with the overall properties derived from the measured hardnesses. The real wires are actually Cu/(Nb-Ti/Nb) composites. It may initially seem unclear how to treat the composites. However, if we recall that the 91 filament conductors drew with broken filaments while the bundled filament composite did not, we could infer that the multifilament conductor acted more like a composite and the bundled filament conductor acted like two individual components. The impact of this will be seen presently. It can be shown [22] that the maximum area reduction per pass (r_{max}) in wire drawing is given by

$$r_{max} = 1 - e^{-\tau(n+1)} \tag{4.7}$$

τ is a measure of the efficiency (τ is less than 1) of deformation which is affected by friction and redundant work. We see that r_{max}, the permitted reduction per pass, decreases as the strain hardening exponent decreases. In the Nb-Ti/Nb composites produced for this thesis work, n was found to be constant throughout the wire drawing strain space. Niobium has been found to steadily work harden by other workers [109] (although some leveling off was observed after a strain of ~10 past the last heat treatment — much greater than the strain of 7-8 past the second extrusion for the present conductors). The work hardening rate of copper has been shown by many workers [109, 28] to plateau at intermediate strains ($\epsilon \sim 3$), thus n for copper decreases at intermediate strains (Figure 4.7). In the case of the multifilament composite, the copper may be partially supported by the Nb-Ti filaments, as suggested by Liu and Warnes [70]. However, in the bundled filament conductor, the wire drawing load must progressively be transferred to the Nb-Ti/Nb bundle because the work hardening rate of copper gradually decreases with increasing strain. This effect is important because the copper sheath comprised about 2/3 of the cross section of the bundled filament conductors. Thus a logical response to the drawability problem would be to reduce the drawing strain per pass as the wires become smaller (eqn. 4.7), which is frequently done in production [33]. Alternatively, the amount of copper could be reduced or the composite annealed, thus restoring n for copper to its original value. We chose to reduce the amount of copper. Copper was etched from conductors containing 30vol% and 40vol% Nb to reduce the fraction of copper to ~1/2. This was equivalent to reducing the conductor diameter by two die sizes. The change in drawability was very marked. The 30vol% conductor went from > 15 breaks (0.45mm $<$ d $<$ 0.16mm, $12 < \epsilon < 14$) to only one (d=$90\mu m$, $\epsilon \sim 14.7$) and the 40vol% conductor went from > 30 breaks (0.8mm $<$ d $<$ 0.28mm, $11 < \epsilon < 13$) to ~7 (0.6mm $<$ d $<$ 0.16mm, $11 < \epsilon < 14$). Both conductors were drawn to $80\mu m$ (the smallest die size we have available), while previous attempts to draw the unmodified composites failed to pass ~0.25-0.15mm. These results clearly indicate a remarkable improvement in fabricability. Incompatible hardening rates of Cu and superconductor may adversely affect the drawability of other APC conductors, especially since the other processes require much more strain to refine the structure than the PM based APC conductors.

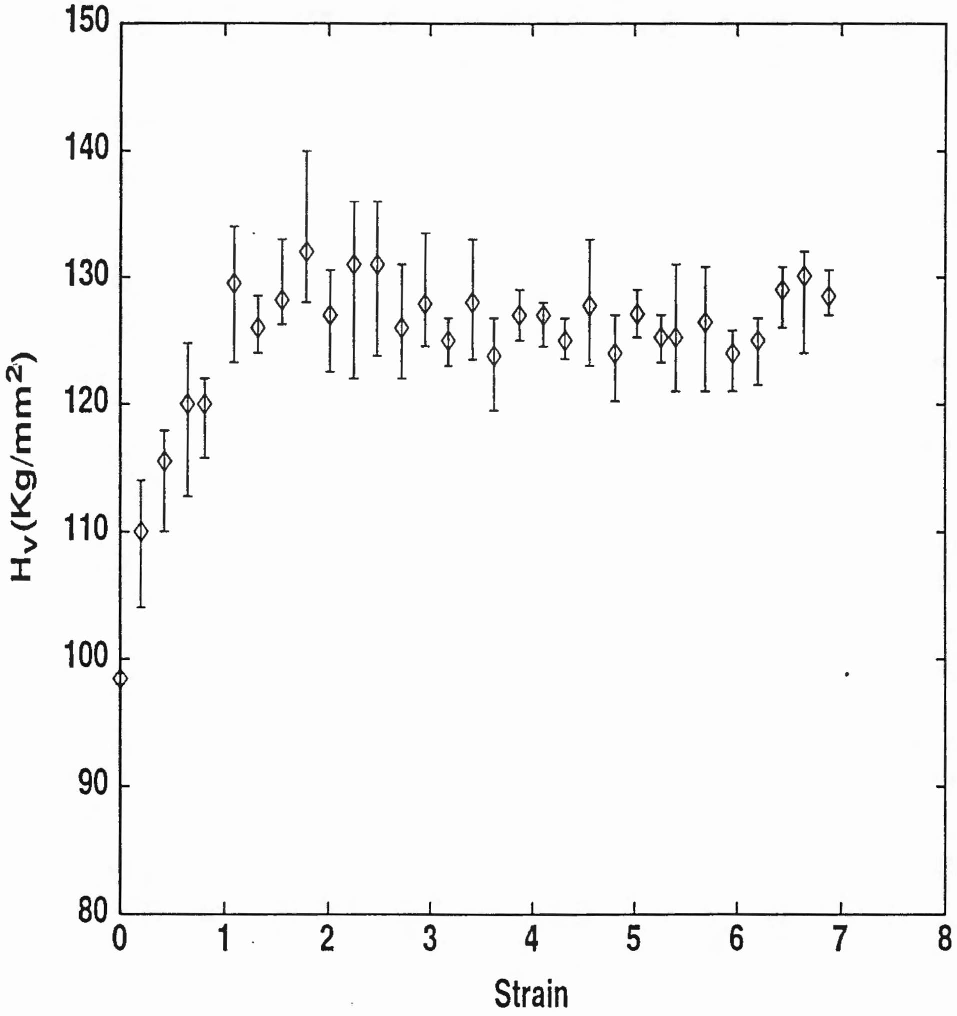

Figure 4.7: Vicker's hardness vs. strain for US C10100 copper. Zero strain corresponds to an anneal heat treatment of 300°C/2h.

Perhaps it is worth considering what implications this might have for other novel composites, for example silver-sheathed Bi-Sr-Ca-Cu-O. In this case the core might be considered to be perfectly plastic (i.e., it does not work harden) thus n=0. Silver appears to respond similarly to copper, in that its work hardening rate also decreases at intermediate strains [28]. The prediction is that these materials would also benefit from a reduction in r as a function of increasing strain. Of course Bi-Sr-Ca-Cu-O composites are more complex than this analysis presumes; e.g., the core density may increase as a function of strain which would exacerbate the problem of decreasing n.

4.5 Summary

The problem we addressed in this chapter was that, although we had eliminated all non-deforming particles from our composites, wire fractures continued and prevented us from reaching final size in the high volume percent niobium composites. Review of predictive wire drawing equations indicated the critical friction factor (μ^*=0.28), beyond which fracture is favored over drawing. Unfortunately, at present we have no easy way of measuring or changing the friction. Perhaps a more important observation was that while the hardening rates of the Nb-Ti/Nb composite cores remained steady through the highest strains measured ($\epsilon\sim$13), the hardening rate of copper was seen to fall off at $\epsilon \sim 2$-3. Since the allowable reduction per draw decreases with decreasing work hardening rate, the Nb-Ti/Nb composite cores were carrying a disproportionate share of the load which occasionally exceeded the core fracture stress causing the wire to break. While improvements in drawability are predicted with use of a decreased reduction schedule ($r < 0.20$), such a die series was not available for evaluation. As an alternative, the amount of copper on the 30 and 40vol%Nb conductors was reduced by etching. This substantially improved the drawability of the wires such that they were fabricated through final size and beyond, to d$\sim 80 \mu m$, our smallest wire drawing die. These conductors thus comprised the ones further characterized in Chapters 5 and 6.

Chapter 5

Microstructure and Superconducting Properties of a Nb-55wt%Ti / 20vol%Nb PM APC Conductor

This chapter explores the superconducting properties of a Nb-55wt%Ti artificial pinning center (APC) composite containing 20vol%Nb added as second phase. The superconducting properties of the composite were studied in terms of the microstructure developed at different drawing strains. The composite incorporated the process refinements outlined in Chapters 2 through 4;

thus no broken filaments or other extrinsic defects were evident in the wires tested. The goals of the experiment were therefore to compare the properties of a good quality PM APC conductor to those obtained from other APC, as well as the conventional processes. Among the questions to be addressed were the fabricability of a PM APC composite, the pinning center refinement and the connection to the superconducting properties. It was found possible to fabricate a good quality composite which drew well to strains greater than those required to establish the optimum superconducting properties. Good superconducting properties were obtained from the composite and strong trends connecting the superconducting properties to the microstructure were observed. The size range of the microstructure at any given stage of the deformation sequence was found to be large. We believe that this compromised the ultimate performance of the composite.

5.1 Billet Fabrication and Other Experimental Details

A detailed description of the billet fabrication was given in Chapter 2, thus only essential details will be given here. A 20vol%Nb billet was fabricated from 15g HGD Nb and 40g PREP Nb-55wt%Ti powders which were blended and pressed into a 15.9×12.7mm (OD×ID) copper extrusion can. The billet was evacuated to $< 10^{-5}$ Pa, sealed and hydrostatically extruded at 250°C with an area reduction ratio of 25 (Figure 5.1 gives an overview of the process, composite configuration, wire diameter and strain). After this first extrusion, copper was dissolved away and the Nb-Ti/Nb rod was heat treated at 800°C for 2h in order to improve the ductility of the Nb particles (see Chapter 3). Once heat treated, the Nb-Ti/Nb APC composite rod was resheathed in copper, drawn to 1.5mm diameter wire and cut into 85 pieces. The copper was again etched off before rebundling the bare Nb-Ti/Nb filaments into a second copper extrusion can. This bundled (85) filament conductor was extruded under the same conditions as before but with an area reduction ratio of 16 (Figure 5.2 shows the overall structure of the bundled filament design) and then drawn to wire having diameters from 0.5mm to $80\mu m$, which correspond to a strain of ~7 to 16 (this range includes both monofilament and bundled filament conductors). The strain, ϵ, is based on the as-extruded superconducting filament core diameter of 2.413mm plus the strain from the first extrusion, $\epsilon \sim 3.22$:

$$\epsilon = 3.22 + 2\ln(2.413/d) \tag{5.1}$$

where d is the equivalent monofilament core diameter whether the composite was a monofilament or a bundled filament conductor. The equivalent monofilament core diameter, d, was given by:

$$d = \frac{d_{comp}}{\sqrt{85(1+CS)}} \tag{5.2}$$

where d_{comp} was the bundled filament composite diameter and CS was the copper to superconductor ratio.

The microstructure was characterized in transverse cross-section using conventional scanning electron microscopy (SEM) secondary electron and backscatter imaging techniques. Transmission electron microscopy (TEM) and field emission scanning electron microscopy (FESEM) techniques were used on some finer scale structures. Transparencies were placed on 200×250mm prints, and tracings were made of the Nb particle outlines. These tracings were scanned into the Megavision computer-based image analysis system in order to determine Nb particle area, perimeter and thickness, as outlined below.

The superconducting critical current density (J_c) measurements were made on wires from the monofilament, as well as from the bundled filament conductor. A resistivity criterion of $10^{-14}\Omega m$ was used to determine the critical current (I_c), and the voltage taps were set 33cm apart[84]. The resistive transition index n was derived from the voltage (V) current (I) characteristics by fitting the V-I characteristic over the range of $\sim$1 to 10 μV to a power law. The superconducting area was found by a weigh and etch

Processing Strain	Composite Diameter	Configuration	Processing
$\varepsilon = 0$	15.9mm	Pressed Powder Billet Monofilament	First Billet Assembly and Extrusion
$\varepsilon = 3.22$	3.2mm		Solution Heat Treatment
			Cold Drawing
$\varepsilon = 5.0$	1.5mm	Round Drawn	Etch Cu/Second Billet Assembly
			Extrusion
$\varepsilon = 7.75$	4mm	Bundled Filament Composite	Cold Drawing
ε=12–14	0.5-0.15mm	Final Wire	

Figure 5.1: Flow chart showing an outline of the pressed powder billet fabrication route.

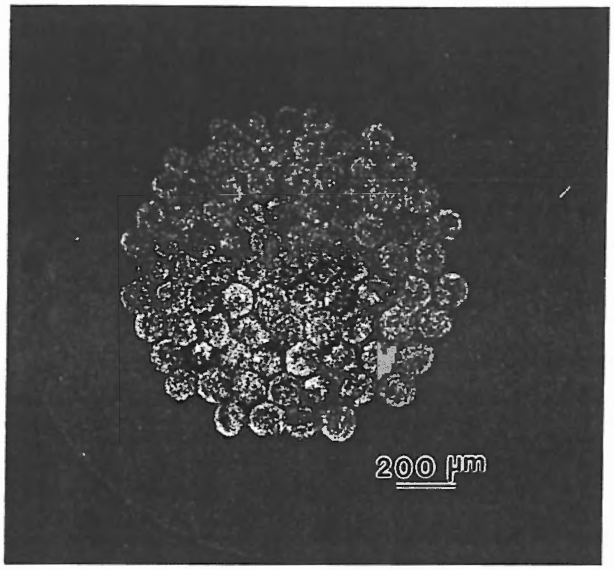

Figure 5.2: SEM secondary electron image showing the overall structure of bundled filament composite.

technique; both the Nb pinning centers and the Nb-Ti matrix were included in the area which was used to calculate J_c from I_c[115].

5.2 Results

5.2.1 Microstructures

The PREP Nb-55wt%Ti and HGD Nb had quite different powder shapes and sizes. Being melted to shape[53], the PREP powder (Figure 5.3) was slightly rough but spherical, with a diameter of $\sim 180 \mu m$ or smaller. Cross-sections of powder particles revealed a dendritic structure with perhaps some

Table 5.1: Powder chemical analysis.

Powder	Analyzed values (ppm)			
	H	N	O	C
Nb-55wt%Ti	8	220	1120	80
Nb	8	30	670	< 30

unmelted regions (Figure 5.4). The individual PREP powder particles were apparently single grained. The HGD Nb pinning center powder was angular in shape (Figure 5.5) owing to the mechanical grinding used to powder the material. The Nb powder was polycrystalline, typically containing a few grains per particle and had a narrow size distribution (~95% of the particles were 45-75μm diameter). According to Table 5.1, the oxygen content of the Nb-55wt%Ti powder was 1120ppm, within the range common for Nb-55-wt%Ti ingots. However, the 670ppm seen in the Nb is about an order of magnitude higher than normally obtained in ingot Nb[104]. The higher than normal oxygen content did not appear to adversely affect the drawability of the composite.

While the overall composition of the conductor was Nb-55wt%Ti + 20-vol%Nb, some regions of the composite were observed to be Nb poor (Figure

Table 5.2: Powder Particle Size and Distribution.

PREP Nb-55wt%Ti	HGD Nb
−80 mesh ($< 180\mu m$), 100wt%	200 mesh ($> 75\mu m$), 1.5wt%
	270 ($> 53\mu m$), 51.0wt%
	325 ($> 45\mu m$), 43.5wt%
	-325 ($< 45\mu m$), 4.0wt%

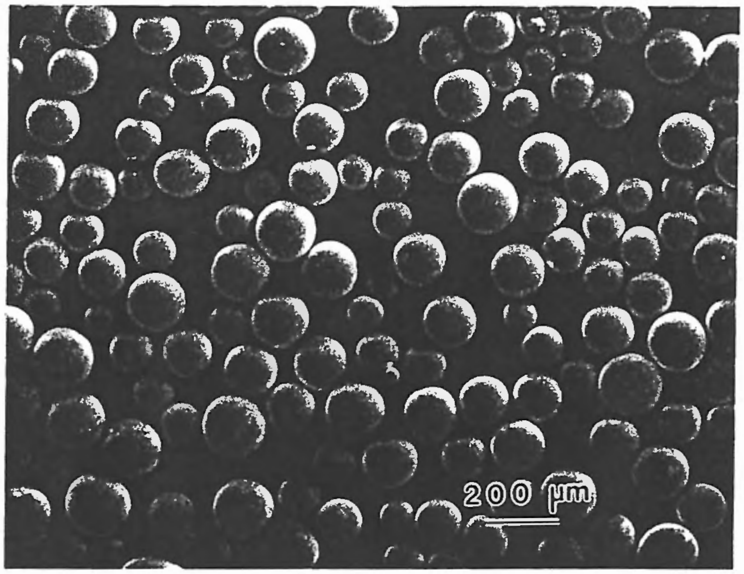

Figure 5.3: SEM secondary electron image of the PREP Nb-55wt%Ti powder used as matrix material.

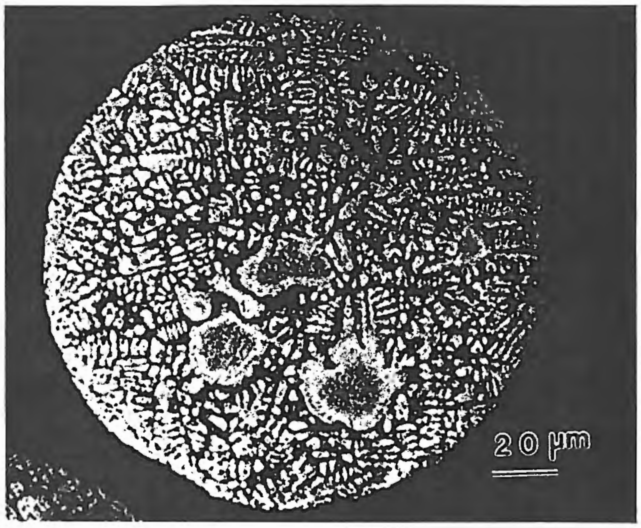

Figure 5.4: SEM backscatter electron image of an polished and etched cross-section of the PREP Nb-55wt%Ti powder.

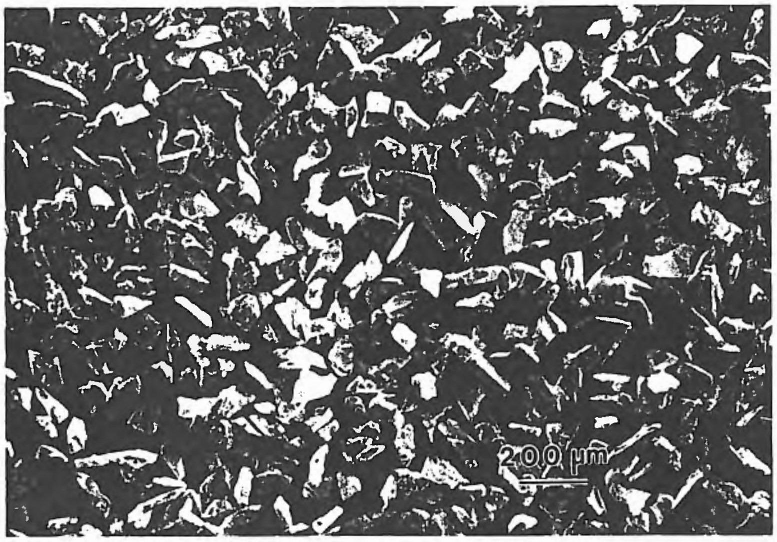

Figure 5.5: SEM secondary electron image of the Nb powder used as pinning center material.

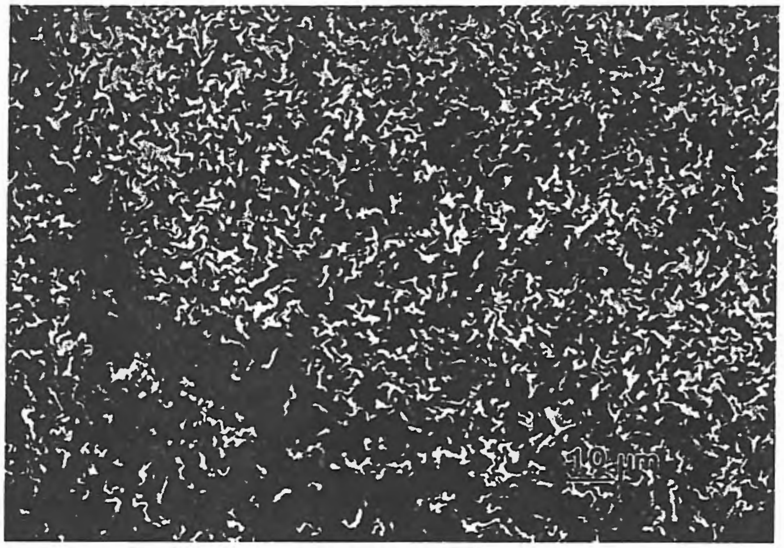

Figure 5.6: SEM secondary electron image showing a localized region depleted in Nb particles. These regions were typically observed near the monofilament surface. The region shown is a triple point where three filaments in the bundled filament conductor.

5.6). Overall, however, the Nb distribution appeared random, even though the outlines of the individual filaments were still detectable. Close examination revealed some Nb-poor regions near the monofilament interfaces. This Nb depletion helps to define the monofilament outline, as observed in Figure 5.2. However, little variation was observed between monofilaments; thus a longitudinally uniform distribution of pinning centers appears to have been established during the initial billet fabrication.

Figure 5.7 shows the Nb particle refinement and shape change as a function of strain, as seen with conventional SEM. At a strain of ~3.22, the Nb particles had already developed a highly aspected ribbon morphology and were quite variable in size (Nb particle cross-sections ranged from 7-720μm^2), especially when compared to the much smaller size range of the starting Nb powder (Figure 5.5 and Table 5.2). The Nb particles develop a more pronounced ribbon morphology as wire drawing strain increased (Figure 5.7). Beyond ϵ~9, the Nb particles were no longer fully resolvable by conventional SEM. Figures 5.8 and 5.9 show TEM images of the nanostructure at strains of ~11 and ~12.8. The dark features in Figure 5.9 are strongly diffracting grains. It is interesting that some Nb and Nb-Ti regions appear to readily cross from dark to light regions, as if the nanometer scale (~50nm dia.) grains were actually composite Nb-55wt%Ti/Nb grains (Figure 5.9).

FESEM was also used to evaluate the microstructure at ϵ~12.8 (Figures

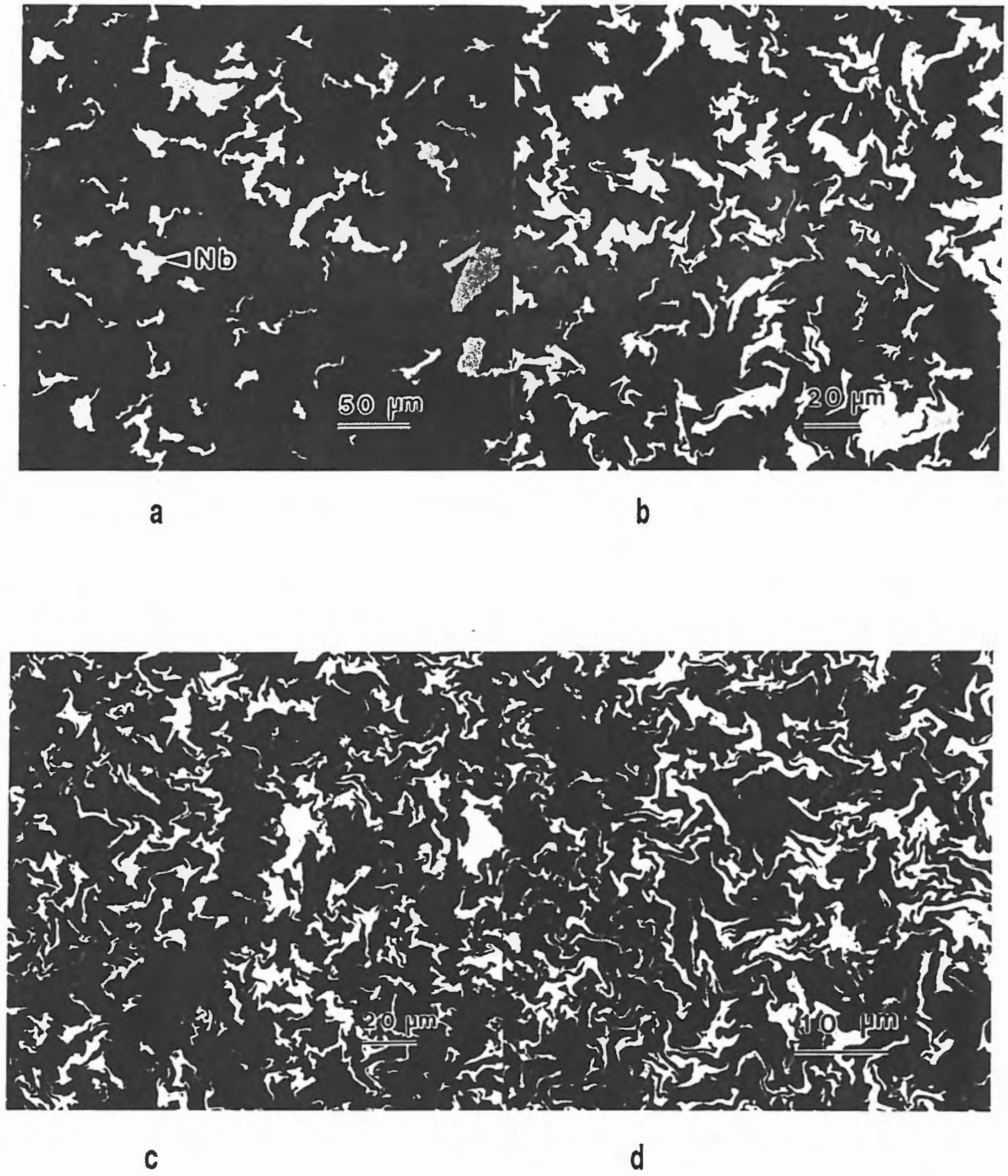

Figure 5.7: SEM secondary electron micrographs at strains of 3.22 (a), 4.47 (b), 5.08 (c), and 7.23 (d) showing the microstructural refinement of the Nb pinning centers during the mechanical deformation.

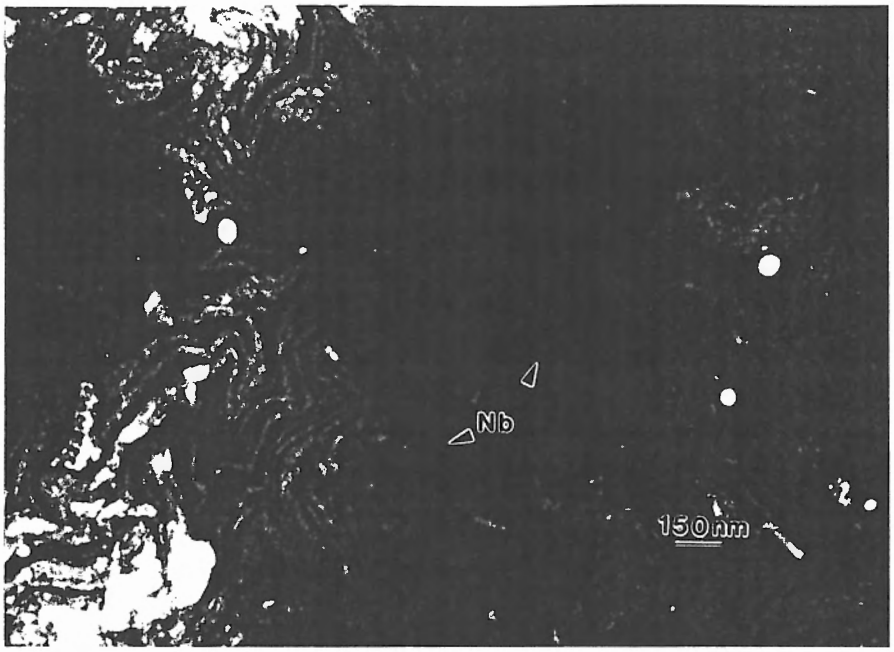

Figure 5.8: Transmission electron micrograph showing further refinement of the microstructure on drawing to $\epsilon \sim 11$.

5.10 and 5.11). Here we see a structure consisting of folded ribbons of Nb in a Nb-Ti matrix, quite similar to that seen in the conventional SEM micrographs and the TEM at $\epsilon \sim 11$. Although the TEM image in Figure 5.9 also shows a similar structure (i.e., folded ribbons of Nb in a Nb-Ti matrix), the linear scales of the two images differ by a factor of ~20 (the boxes in Figures 5.10 and 5.11 represent areas equivalent to that shown in Figure 5.9). Thus it appears that the size scale of the imaged features changes significantly depending on the imaging techniques used. This point will be addressed further in the Discussion.

The characterization technique used for the microstructural quantifica-

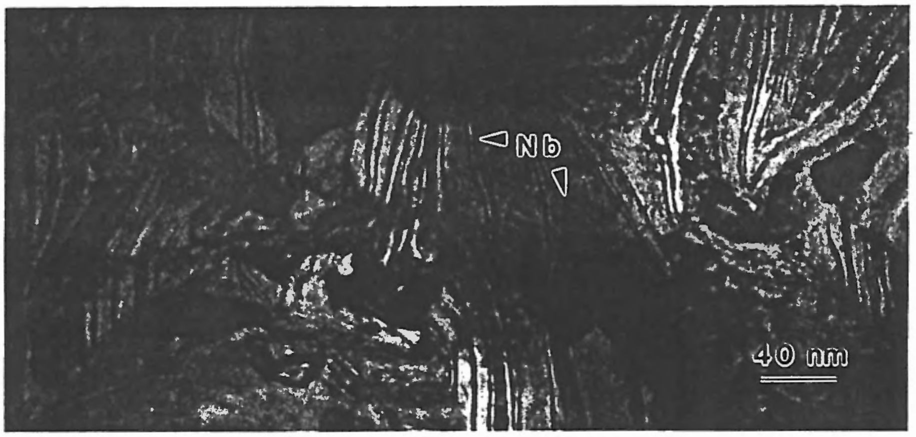

Figure 5.9: Transmission electron micrograph showing the fine scale of the microstructure as the composite nears optimum size for the high field J_c ($\epsilon \sim 12.8$).

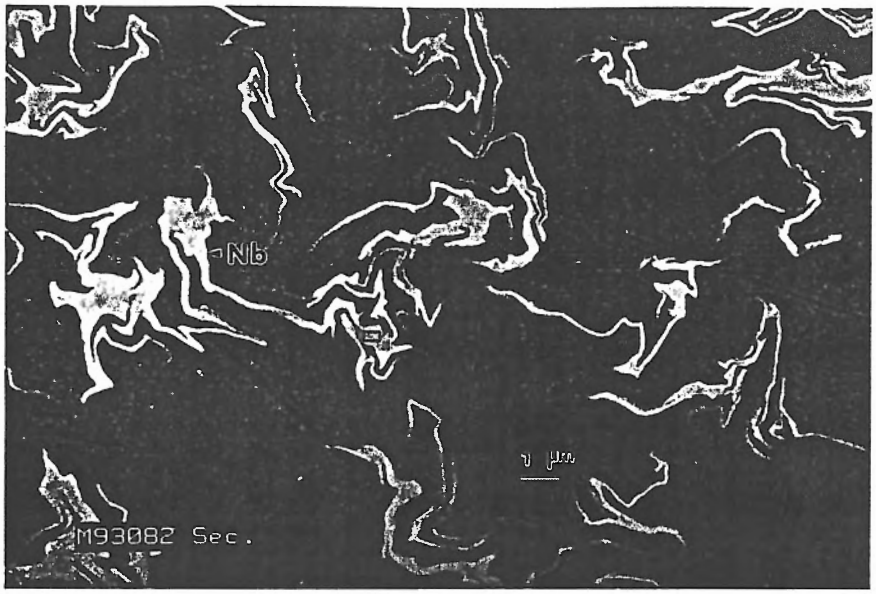

Figure 5.10: Field emission scanning electron microscopy secondary electron micrograph showing the microstructural development of the APC conductor at a strain of 12.8. This is the same wire size shown in Figure 5.9. The box outlines the approximate equivalent area shown in Figure 5.9.

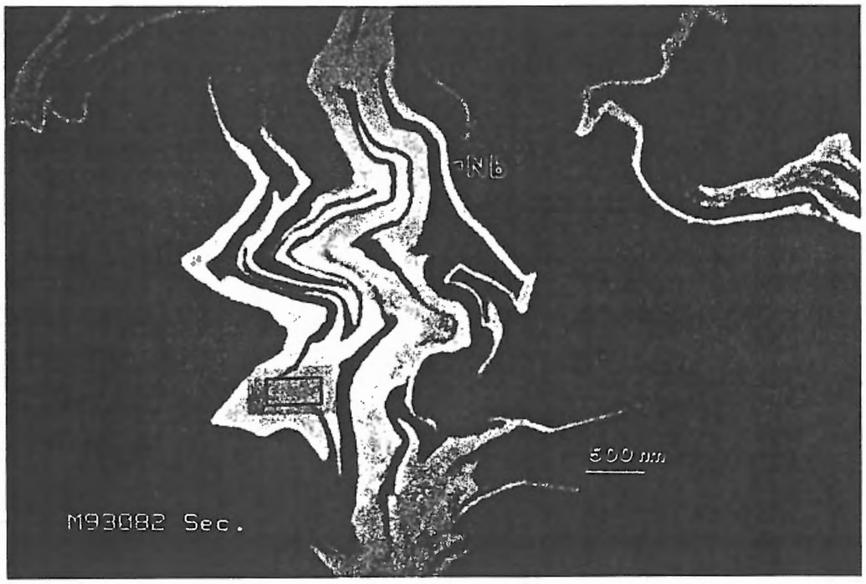

Figure 5.11: Field emission scanning electron microscopy secondary electron micrograph showing the microstructural development of the APC conductor at a strain of 12.8. This is the same wire size shown in Figure 5.9. The box outlines the approximate equivalent area shown in Figure 5.9.

tion was one which described the thickness of each Nb particle by a single value. Since there were many Nb particles in each image and each varied in thickness, it is necessary to describe them in terms of an average particle thickness. The average Nb particle thickness was calculated from the particle area (A) and perimeter (p) measured from the conventional SEM images. To convert these measurements to a thickness, a shape transform was applied to the Nb particle. This shape transform converts the irregular shaped particle into a rectangular shape with the same area (A) and perimeter (p) as the original Nb particle. From the rectangular geometry we have:

$$A = t_{Nb} l_{Nb} \tag{5.3}$$

and

$$p = 2\left(t_{Nb} + l_{Nb}\right) \tag{5.4}$$

where t_{Nb} and l_{Nb} are the thickness and length of the rectangular equivalent, respectively. Thus it is a simple matter to use eqns. 5.3 and 5.4 to solve for t_{Nb} in terms of p and A:

$$t_{Nb} = \frac{p - \sqrt{p^2 - 16A}}{4} \tag{5.5}$$

Equation 5.5 gives the thickness of the rectangular equivalent of the original Nb particle. t_{Nb} calculated from eqn. 5.5 has been found to be in good agreement with the average particle thickness as measured by the line intercept method (see Discussion) and is one of the simplest microstructural characterization techniques [96]. Additional features of this technique will be presented in the Discussion.

Figure 5.12 plots the averages of the Nb particle thicknesses (t_{Nb}) for each of the images analyzed. The abscissa is the superconducting filament diameter, d, which is the equivalent monofilament core diameter whether the data was taken from a monofilament or a bundled filament conductor. The equivalent strain is given at the top of the figure. The bars indicate the $t_{Nb}+/-2\sigma$ values for data taken from conductors with d >0.1mm. This data was also used to formulate the predictive t_{Nb} and $t_{Nb}+/-2\sigma$ lines shown in the figure using

$$\log(t_{Nb}) = a + b\log(d) \tag{5.6}$$

The coefficients to eqn. 5.6 are given in Table 5.3. The data below d~0.1mm are from the TEM images (Figures 5.8 and 5.9) and the FESEM images (Figures 5.10 and 5.11). In these two cases the bars indicate the actual range of the data, rather than $+/-2\sigma$ data. As can be seen in the figure, t_{Nb} from the conventional SEM images ranges from $\sim 3\mu m$ to $\sim 0.2\mu m$ as d is reduced from ~2mm to ~0.1mm. At the same time the $t_{Nb}+/-2\sigma$ values ranged from a factor of ~10 to a factor of ~5-6; thus it would appear that the tendency was for the structure to become more uniform with increased strain. However, the range of the t_{Nb} values derived from the TEM images taken

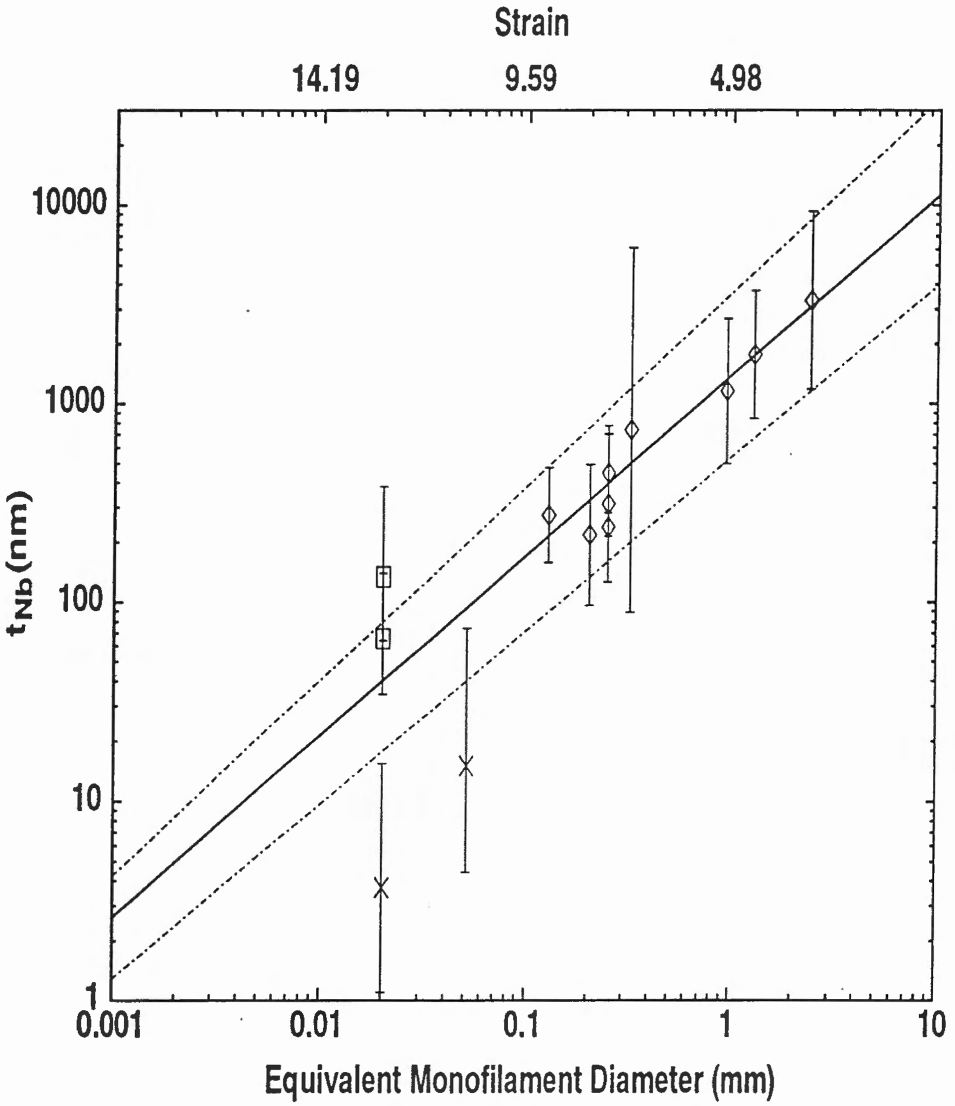

Figure 5.12: Nb particle thickness vs. equivalent monofilament diameter for the Nb-55wt%Ti + 20vol%Nb conductor. The symbols represent: ◇ = conventional SEM, × = TEM, and □ = FESEM. The bars indicate the $+/-2\sigma$ values for d >0.1mm and the range of t_{Nb} for d <0.1mm. The lines represent log-log linear regression fits to the conventional SEM t_{Nb} and $+/-2\sigma$ data.

Table 5.3: Coefficients for the predictive t_{Nb} equation (eqn. 5.6) based on the image analysis results from the conventional SEM images and the equivalent monofilament core diameter d(mm).

	a	b
$t_{Nb}(\mu m)$	0.144	0.908
$t_{Nb}-2\sigma(\mu m)$	-0.271	0.873
$t_{Nb}+2\sigma(\mu m)$	0.560	0.978

at smaller size was larger (more than a factor of 10) than this prediction, and the average t_{Nb} values were about 10 times smaller than those predicted by the extrapolation of the conventional SEM data. The FESEM results showed t_{Nb} slightly larger than the predicted values (~1.5 to 3 times larger) and a range of values similar to what was predicted by the extrapolation from larger sizes (~5 times). Thus the size distribution appears to depend on the characterization technique used, a point which we return to in the discussion.

5.2.2 Superconducting Properties

As the microstructure was refined, the critical current density increased markedly. Figure 5.13 shows J_c vs. B at several stages of refinement. Here we see that J_c(1T) rises from $\sim 1200 A/mm^2$ to $\sim 7500 A/mm^2$, while J_c(5T) rises from $\sim 50 A/mm^2$ to $\sim 2000 A/mm^2$ with n-values >60. The improvement in J_c corresponds to a refinement of t_{Nb} from ~500nm to ~30nm, as shown by Figure 5.12.

We examine this trend in more detail as exhibited by the enhancement of J_c(5T) with strain (Figure 5.14). In order to incorporate a strain range of ~7-16, results from both the monofilament and bundled filament conductors are shown. We see that there is a smooth transition between the two, and that J_c steeply increases in the strain range of ~10-13. This corresponds to t_{Nb} refining from ~500 to 40nm, as derived from the data in Figure 5.12. At $\epsilon \sim 13$-14, J_c(5T) reaches a maximum value $\sim 2000 A/mm^2$ after which a falloff is observed. The peak value is only weakly dependent on t_{Nb} in the range from 40 to 17nm, a falloff commencing once $t_{Nb} < 17$nm.

The influence of the pinning center refinement on the flux pinning behavior is shown by plotting F_p vs. B curves (Figure 5.15). We observe that F_p increases with increasing strain at all fields for $\epsilon \sim 8$-13.5 ($t_{Nb} \sim 330$ to 30nm), reaching a maximum of $\sim 11.5 GN/m^3$ at 3T. With further refinement of the microstructure, $F_{p_{max}}$ diminishes, the falloff being apparent at low fields. We observe $B(F_{p_{max}})$ to increase from <1T at $\epsilon \sim 8.2$ to ~4T at $\epsilon \sim 14.6$ as summarized in Table 5.4. However, F_p at fields beyond $B(F_{p_{max}})$ appears to saturate. Additionally, B_{c_2}, evaluated by extrapolating F_p to zero, remained constant at ~9.5T for strains of 11.85 to 15.60. This value is similar to the

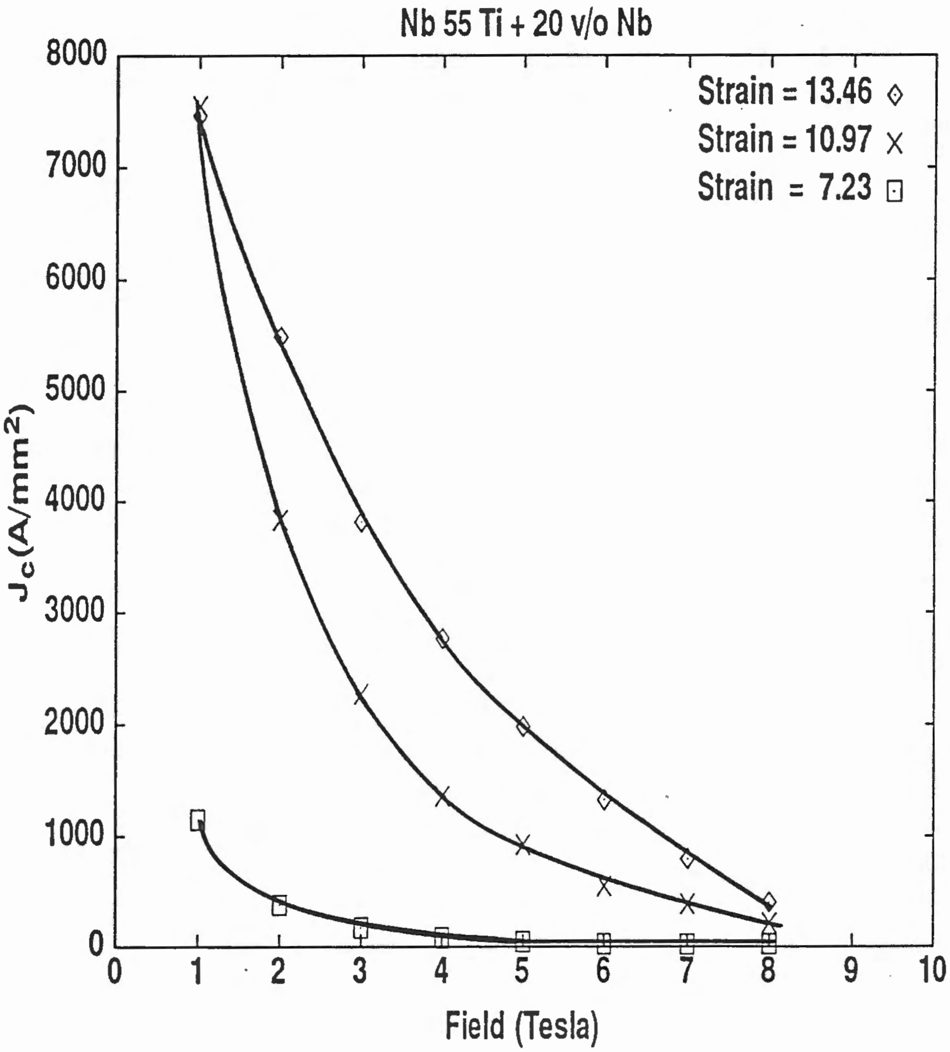

Figure 5.13: J_c vs. B for various stages of microstructural refinement. The largest strain wire (ϵ~13.46) is approximately the wire size that has optimum J_c(5T) properties.

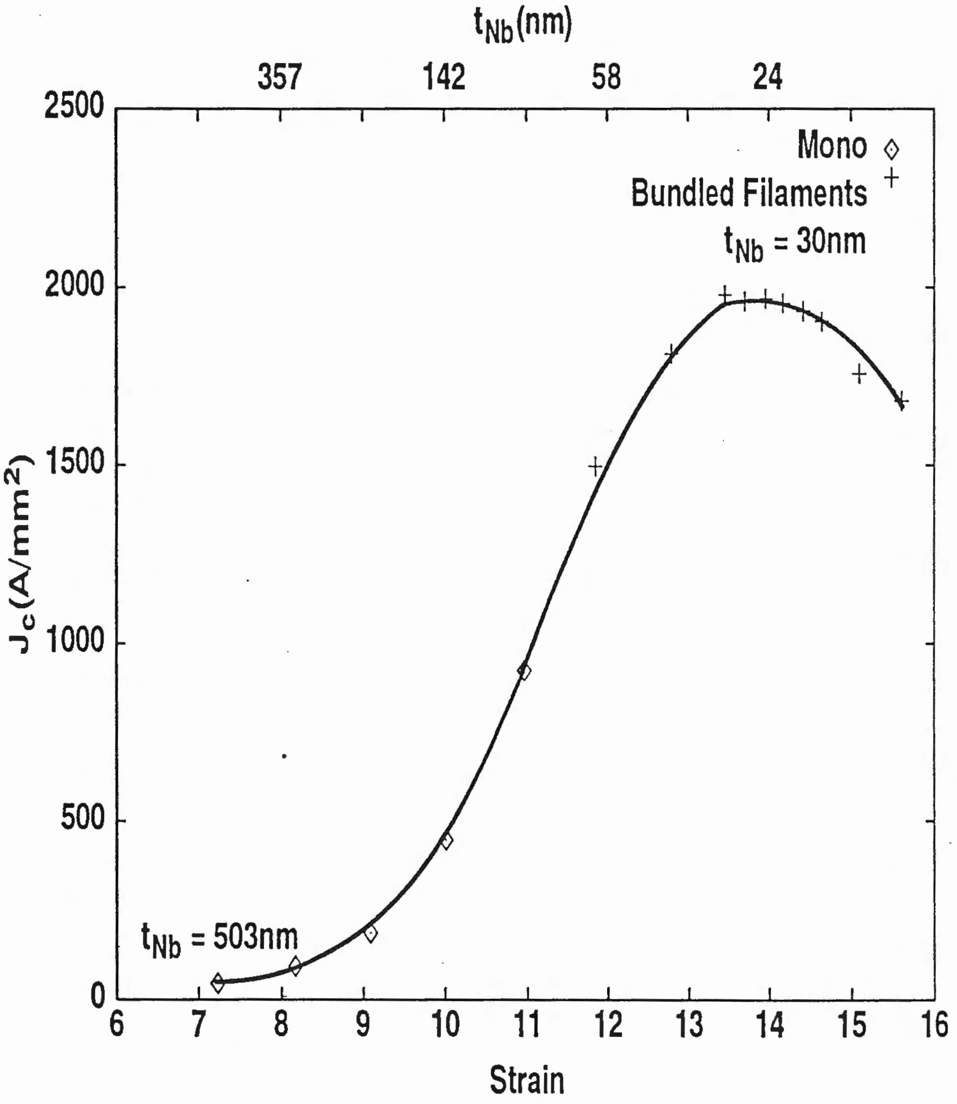

Figure 5.14: J_c(5T) vs. strain and t_{Nb}. t_{Nb} is also given at low strain ($\epsilon \sim 7$) J_c and peak J_c in the figure.

Table 5.4: $B(F_{p_{max}})$ at Differing Strains.

$B(F_{p_{max}})$	ϵ	t_{Nb}
<1T	8.17	328nm
~2T	10.97	92
~3T	11.85	62
~3T	13.46	30
~4T	15.60	11

9.7T of the matrix Nb-55wt%Ti. This is consistent with the derived t_{Nb} values since we would expect B_{c_2} to increase to almost 11T when the Nb particles become refined to <5nm. We return to this point in the Discussion.

A comprehensive view of the influence of precipitate thickness on optimum J_c over a wide range of fields is shown in Figure 5.16. We see that J_c peaks for t_{Nb} values ranging from 20-35nm and that the peak occurs at larger t_{Nb} for lower fields. The dependence of J_c on t_{Nb} is also observed to be much sharper at lower than at higher fields.

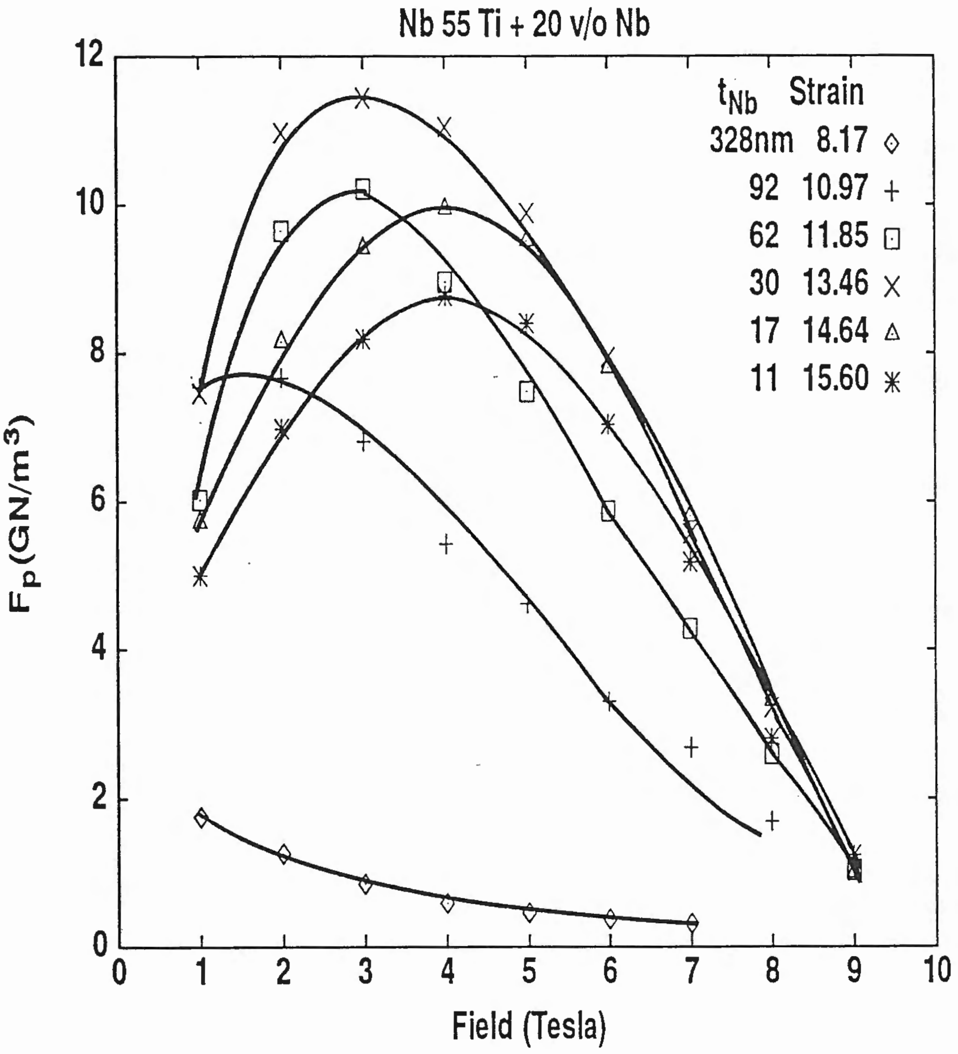

Figure 5.15: F_p vs. B at various stages of Nb thickness refinement.

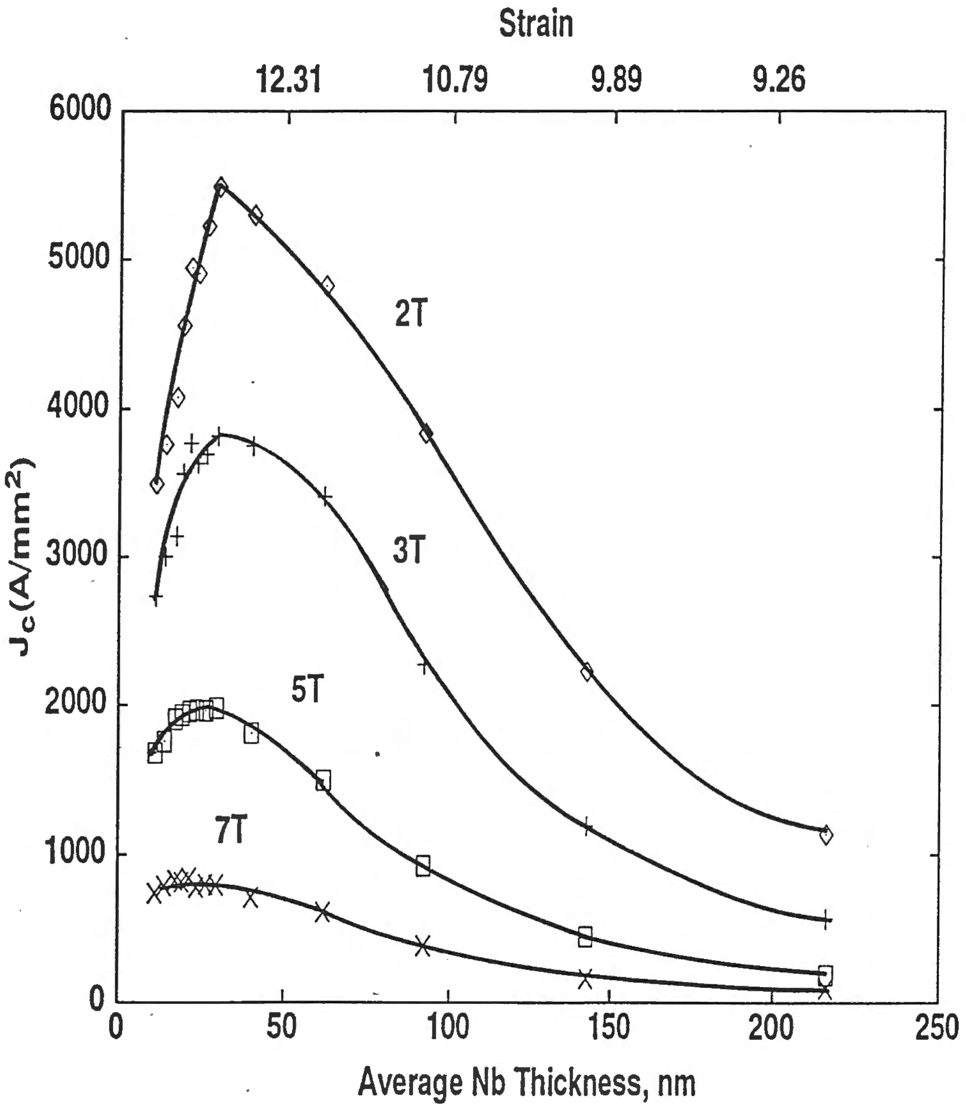

Figure 5.16: J_c vs. Nb thickness for 2, 3, 5, and 7T.

5.3 Discussion

The goal of this thesis was to develop a new process for making APC composites that would offer advantages of fabricability and performance as compared to either conventional Nb-Ti or the other APC designs. The innovation of the PM APC process has been recognized by the award of a U.S. patent[49]. In this chapter we have described the fabrication and performance of a composite having about the same amount of pinning center as is contained in conventionally optimized Nb-Ti composites. In the following sections we will discuss several key questions concerning the fabrication, the microstructure and the superconducting properties of this composite. We will conclude with some preliminary comments about the advantages and disadvantages of the PM APC process. Further discussion will be made at the conclusion of Chapter 6 which is a study of PM APC composites having variable pinning center volume fractions.

5.3.1 Composite Fabrication

While an occasional wire fracture occurred, the composite drew well through two extrusions to a total strain of almost 16. This fabrication achievement is not at all negligible, given that the composite contained 20vol% of second phase throughout the whole process. By comparison, the conventional Nb-

Ti billet fabrication process gradually develops ~20vol%α -Ti over a strain range of 5 to 7 during 3 or 4 heat treatments. The final drawing strain of ~5 produces a maximum strain of ~12, beyond which point wire drawing breaks become very common. We avoided these difficulties largely due to the process refinements discussed in Chapters 3 and 4. The high quality of the composite is exemplified in the high n-values at peak J_c(5T) of ~60.

As was pointed out earlier, the PREP matrix and HGD pinning center powders were quite different in size and shape (Figures 5.3 and 5.5). We were concerned that this would make composite fabrication difficult. However, with the process refinements described in Chapters 2 through 4, particularly those which minimized powder handling and the pressing of the powder directly into the extrusion can, a composite was fabricated with a well distributed second phase. Nonetheless, some Nb-depleted regions were observed, typically near the monofilament surface. We tentatively assign this depletion to the better packing of the surface region by round, rather than angular particles. These Nb-depleted regions are perpendicular to the direction of fluxon movement, i.e., perpendicular to the wire axis. Thus their impact on the superconducting properties should be negligible. In addition, the bundled filament design distributes these pinning-center depleted regions throughout the composite, further minimizing their impact.

The powder-mixing process (see Chapter 2) is inherently a random, rather than an ordered mixing process. Thus some Nb-Nb particle contacts are expected during the billet pressing step and these should lead to larger particles which become welded during extrusion. We conclude that the random mixing will inherently broaden the starting Nb particle size distribution, a point that requires further discussion in the next section.

5.3.2 Microstructural Changes During Deformation

Underlying the whole APC concept is the idea that a more ideal or more conveniently fabricable pinning structure can be produced than is obtainable by conventional precipitation and drawing cycles. The conventional process produces ~20vol% of a very dense array of nanometer thick α -Ti ribbons which produce strong flux pinning forces exceeding $15GN/m^3$ when drawn to their optimum thickness of ~1 to 3nm[84]. At this size the precipitates are strongly coupled to the matrix. The maximum bulk pinning force is a strong function of strain, which suggests that the pinning interactions are optimized at a specific precipitate thickness.

Meingast and Larbalestier[84] showed that the flux pinning in conventional Nb-Ti arose from the interaction of the fluxon cores with the α -Ti ribbons. The flux pinning scaled with the thickness and number density of the α -Ti ribbons which is consistent with a elementary fluxon core pinning interaction and with full summation (i.e., every fluxon is pinned). When the core interaction is responsible for flux pinning, ribbons are advantageous since they have a well defined thickness and the long axis (in transverse section) is advantageous for the capture of vortices over long lengths. Thus, in comparison to lower dimensional defects, such as rod-shaped pins which provide only a point-like interaction, the ribbon morphology is advantageous.

Such a ribbon nanostructure was also obtained in this PM APC composite. The microstructure changed greatly as it was deformed through a total strain of ~16. Significant changes resulted from the first extrusion (compare Figures 5.5 and 5.7). The strain of this extrusion is large ($\epsilon \sim 3.22$) being more than half the strain ~5 required to optimize the two-phase microstructure of conventional Nb-Ti after the final heat treatment. During the extrusion, as seen in Figure 5.7, the initially angular Nb particles were deformed into ribbon-shaped particles. These ribbons continued to thin and to become more convoluted in shape as the deformation strain increased (Figure 5.8) because both Nb-Ti and Nb are bcc phase metals which develop a $\langle 110 \rangle$ wire texture during extrusion and wire drawing. This texture provides only two active slip directions, and local deformation occurs in a plane strain rather than in axisymetric mode[43, 72]. As a result, grains tend to become highly aspected and must intercurl to accommodate one another, thus producing the convoluted Nb particle shapes seen in Figures 5.7 through 5.11. However, while the Nb particles do form into ribbons, they are not nearly as uniform in thickness as the α -Ti ribbons of conventional Nb-Ti. This complicates quantitative microstructural characterization for which it is desirable to represent the microstructure by a single number. Perhaps more importantly, it greatly complicates the optimization of F_p with strain since the particle thickness varies widely from one particle to another.

The extensive microstructural characterization done at large sizes permitted a linear regression analysis and thus a prediction of t_{Nb} at final size (Figure 5.12). We tried to use TEM to verify these predictions but found it difficult to get large thin areas at final size. Although it was clear that TEM could not be used as a routine test, we wanted to check the t_{Nb} extrapolations. Thus we compared TEM (resolution ~1nm) and FESEM (resolution ~50nm) characterizations at a strain of ~12.8, which is very near the optimum strain of ~13.5. We found that the FESEM gave results which fell on the high side of the SEM extrapolation and the TEM on the low side of the extrapolated t_{Nb}. These results are consistent with the resolution limit of the FESEM and the difficulty of foil preparation for TEM. As a final independent check, we considered t_{Nb} at optimum size. t_{Nb} is predicted to be 30nm by Figure 5.12. Since the extrapolated B_{c_2} from the F_p curve is identical to that of the matrix, t_{Nb} must be greater than 2ξ~10nm, which sets a lower bound for t_{Nb}. Since the particles refine into ribbons they thin faster than a simple proportional prediction of ~70nm, which sets an upper bound. Thus, as the predicted t_{Nb} lies between these extremes, Figure 5.12 appears to be an adequate estimate of t_{Nb}.

At this point we would have liked to compare our microstructure to that of other APC composites. Unfortunately, *all* other investigators[23, 56, 98, 99, 123, 124] working on Nb-Ti APC conductors report only the "effective" thickness (or diameter) of the pinning center as a simple function of wire diameter, assuming uniform co-reduction of the composite from initial through final size. In comparison to α -Ti in conventional Nb-Ti, the Nb thickness is quite variable. Since the size of the α -Ti grains are comparable to the size of the Nb-Ti grains, perhaps this plays a critical role in maintaining a more uniform α -Ti thickness. Recalling that the ribbon morphology develops as a result of the $\langle 110 \rangle$ wire drawing texture, it is worth briefly considering what might be done to better control the Nb particle morphology. Heussner [38] showed that grain size plays a major role in the shape instability of Nb-foil-wrapped Nb-Ti rods, and Cooley et al.[18] showed that the overall pinning center rod shape could be maintained, at least down to ~100nm diameter, in a gunbarrel-drilled Nb-Ti/Nb APC composite by starting with fine grained materials. Indeed, it was shown that the particle shape in Cooley's composite could be destroyed within a drawing strain of 1-2 after a recrystallization heat treatment, if the resulting grain size was too large [19]. Consequently, grain size has been established as a critical factor in determining the particle shape, small grain size being preferred since it helps maintain shape stability. While a very narrow Nb particle size distribution was used for pinning centers of this composite, the particle size of Nb-Ti was more variable. Thus we can cite several factors which may play important roles in broadening the size distribution of Nb pinning centers at optimum size: starting size distribution, the random packing process, too large a grain size in the matrix and pinning center, and finally, spherical matrix and angular pinning center morphologies.

5.3.3 Superconducting Properties

Unlike our earlier PM APC composites [50] in which the J_c values were compromised by broken filaments, the present results show no signs of extrinsic limitations (i.e., we observed no broken filaments and the composite had high n-values at optimum J_c size). Thus the present work represents an opportunity to evaluate the "intrinsic" flux pinning characteristics of this PM Nb-Ti APC conductor, thus making it useful to relate the microstructure to the superconducting properties.

The general trends seen in the optimization of F_p with refinement of pinning center size (Figure 5.15) are similar to those seen in conventional Nb-Ti. There is only a weak dependence of F_p or J_c (Figure 5.14) on strain up to the point at which t_{Nb} becomes less than 100nm. F_p and J_c become greatly enhanced for $t_{Nb} < 100$nm. However, below $t_{Nb}\sim30$nm, the J_c becomes much less sensitive to strain, and ultimately the properties decline. These results are similar to conventional Nb-Ti, a result which is not unexpected since the process mimics the refinement of α -Ti pinning centers. The fundamental difference is that the pinning centers are Nb rather than Ti, since the quantity of pinning center in this composite (20vol%Nb) is nearly identical to the 18-20vol%α -Ti found in optimized conventional composites.

There are however several differences of detail between the properties found in this PM APC composite and conventional Nb-Ti. For example, $F_p(B)$ reaches its maximum at $\sim0.3B_{c_2}$ while in conventional Nb-Ti $F_{p_{max}}$ occurs at $\sim0.5B_{c_2}$. Also, $F_{p_{max}}$ for the PM APC conductor occurs for $t_{Nb}\sim30$nm rather than 1-3nm. Whatever the uncertainty in the exact value of t_{Nb} in this composite, there is clearly a large difference between this and conventional Nb-Ti. This difference has also been reported in the linear extrapolated t_{Nb} of other APC conductors (e.g., Cooley[18], Matsumoto[76], and Yamafuji[123]). Thus F_p peaks for a much lower density of pinning centers than in conventional Nb-Ti. This and the peaking of F_p at low fields are probably connected since one consequence of an optimization at sizes much less than the vortex diameter is that there are always more precipitates than fluxons however high the field.

It was observed that the extrapolation of $F_p(B)$ to zero was independent of strain within the limits of linear extrapolations made for composites having strains of 11 to 15.6, which corresponds to t_{Nb} varying from 92 to 11nm. This result is surprising because it is clear from conventional Nb-Ti that B_{c_2} becomes that of the overall composition once the nanostructure has a scale less than the coherence length[84]. At t_{Nb}=11nm the $+/-2\sigma$ range is 5 to 20nm, i.e., 1-4ξ. Thus we would expect to see some proximity effect coupling between the Nb pins and the Nb-Ti matrix. Based on the overall composition (80vol%Nb-55wt%Ti + 20vol%Nb), we would expect that any mixing would lead to an increase in B_{c_2}, from ~9.5T of the Nb-55wt%Ti matrix to a maximum of ~11T at Nb-44wt%Ti to ~10.7T of the overall Nb-40wt%-Ti composition. From the lack of any measured increase in B_{c_2} we must conclude that there was essentially no useful mixing which would produce a more Nb-rich matrix at any of the wire strains tested. This confirms beyond a doubt that the Nb pins are optimizing at sizes which are considerably larger than is the case for α -Ti ribbons in conventional Nb-Ti.

A final point to discuss is what the ultimate capability of the PM APC composite process is. The global aspects of this are best left to Chapter 6 where composites having 0-40vol%Nb are discussed. At this point we can compare the properties to conventional Nb-Ti. An important qualification to the capability of this composite is that the B_{c_2} was ~9.5T, rather than the ~10.7T of its design. Thus the high field J_c of this composite is necessarily compromised in comparison to conventional Nb-Ti. The F_p of $11.5 GN/m^3$ compares very favorably to the values seen before high homogeneity Nb-Ti alloy was introduced. The older, inhomogeneous Nb-Ti alloys typically reached values of $F_{p_{max}} < 10 GN/m^3$ ([57, 60]). The introduction of high homogeneity Nb-Ti alloys raised the potential of conventional Nb-Ti to $F_p \sim$15-18GN/m^3 [69]. Thus it may well be that the present conductor is limited by the broad variation of its pinning center size.

5.4 Conclusions

We have demonstrated that a Nb-Ti/Nb artificial pinning center superconductor can be made by powder metallurgy techniques within a reduced strain space ($\epsilon < 14$). The superconducting properties are greatly enhanced as the structure is refined (5490 A/mm^2 at 2T and 1980 A/mm^2 at 5T as t_{Nb} refines through ~30nm). The bundled filament technique and other process improvements described in Chapters 3 and 4 provided relief from extrinsic limitations experienced in earlier multifilament conductors[50]. A considerable variation in t_{Nb} was measured (~1 to 400nm at $\epsilon \sim 12.8$). Since microstructures of the other APC designs have not been quantitatively characterized, it remains to be seen how the present results would compare. However, the observed distribution in t_{Nb} is very large compared to that observed in α -Ti ribbons in conventional Nb-Ti. Thus the broad distribution of t_{Nb} may be adversely impacting J_c, especially at higher fields. The evidence supporting a broad distribution in t_{Nb} include: the measured and extrapolated t_{Nb} values and the J_c vs. ϵ optimization curves. We illustrate several possible sources of these variations and have identified corrective actions throughout the chapter.

Chapter 6

The Influence of Pinning Center Volume Fraction on the Superconducting Properties of PM APC Conductors

In the previous chapter, we described in detail the microstructural and critical current density development of a Nb-55wt%Ti + 20vol%Nb conductor fabricated by the pressed powder extrusion process. Here we consider conductors with 0-40vol%Nb second phase, as much as two times the amount of second phase obtainable in conventionally processed Nb-47wt%Ti.

6.1 Billet Fabrication and Other Experimental Details

Since the details of the billet fabrication are contained in Chapter 2, this section will serve to briefly review the pertinent details of the fabrication process. The appropriate amounts of powders were weighed, blended and pressed into 15.9×12.7mm (OD×ID) copper extrusion cans to fabricate composites of Nb-55wt%Ti + 0-40vol%Nb in steps of 10vol%Nb (Table 6.1). The pressed powder billets were evacuated to $< 10^{-5}$ Pa, sealed and machined. Each billet was preheated in the extrusion press chamber for ~15 minutes and then extruded at 250°C with an area reduction ratio of 25. The copper was etched off the extruded rods which were then heat treated at 800°C for 2h (except for the 0vol%Nb control billet). This heat treatment was found to improve the ductility of the Nb particles. The APC composite rod was then sheathed in copper, drawn into 1.5mm diameter wire and cut into 85 pieces. The copper was again etched off, so that the APC rods (~1mm diameter) could be rebundled into a monolith inside another extrusion can. The second extrusion conditions were similar to the first, this time with a area reduction ratio of ~16. The strain, ϵ, is based on the as-extruded superconducting filament core diameter, d_o (given in Table 6.6) plus the strain from the first

Table 6.1: Compositions of Composite Billets

vol%	ID	wt. Nb-55wt%Ti	wt. Nb	Overall Composition
0	P20X	50g	0g	Nb-55wt%Ti
10	P21P	42.80	7.20	Nb-47.0wt%Ti
20	P22L	39.88	15.12	Nb-39.9wt%Ti
30	P23H	30.30	19.70	Nb-33.3wt%Ti
40	P24C	24.85	25.15	Nb-27.3wt%Ti

extrusion, $\epsilon = 3.22$:

$$\epsilon = 2\ln(d_o/d) + 3.22 \tag{6.1}$$

where d is the equivalent monofilament core diameter whether the composite was a monofilament or a bundled filament conductor. The equivalent monofilament core diameter, d, was given by:

$$d = \frac{d_{comp}}{\sqrt{85(1+CS)}} \tag{6.2}$$

where d_{comp} was the bundled filament composite diameter and CS was the copper to superconductor area ratio. Figure 6.1 contains an overview of the process, including strains, composite dimensions and composite configuration.

The microstructural development was characterized using SEM backscat-

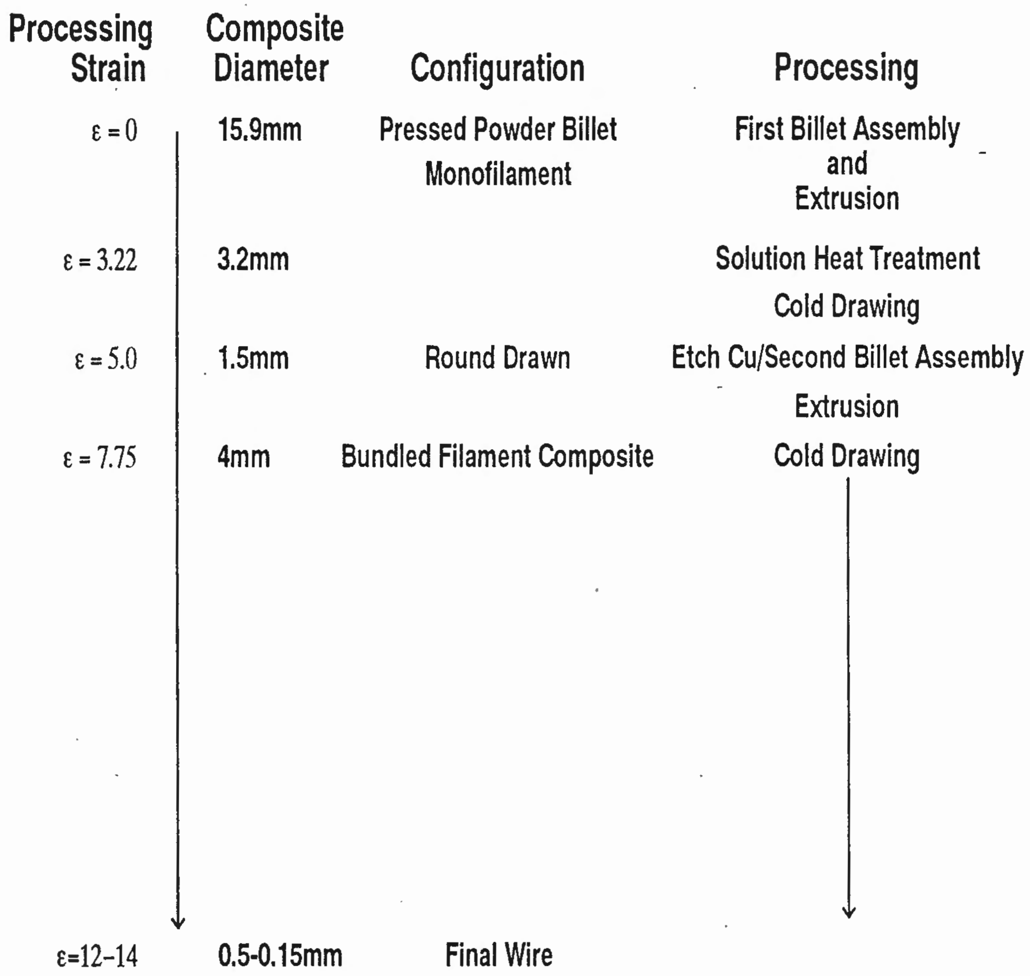

Figure 6.1: Flow chart outlining the pressed powder billet fabrication route.

ter techniques on transverse cross-sections. Transparencies were placed on 200×250mm prints and tracings were made of the Nb particle outline. The tracings were scanned into the Megavision computer-based image analysis system. The measured Nb particle area and perimeter were used to estimate the Nb thickness, as outlined below.

The superconducting critical current density (J_c) measurements were made on wires from the original monofilaments, as well as the bundled filament conductors. In this way, superconducting properties could be measured over the strain range of ~7 to 16. A resistivity criteria of 10^{-14}ohm-m with the voltage taps set 33cm apart (similar to Meingast et al.[84]) was used to determine I_c. The resistive transition index n was derived from the voltage (V) current (I) characteristics by fitting the V-I characteristic over the range of ~1 to 10 μV to a power law. The superconducting area was found by a weigh and etch technique; the Nb pinning centers were included in the Nb-Ti area. These procedures are identical to those reported in Chapter 5.

6.2 Results

6.2.1 Microstructural Comparison

Transverse cross-sections of the APC microstructures immediately after the first extrusion are shown in Figure 6.2. It can be seen that the Nb particles de-

Table 6.2: As-Extruded (ϵ~3.2) Nb Particle Area Size Range.

vol%	Min	Max
10	4 μm^2	740 μm^2
20	7	720
30	8	1020
40	8	17,700

velop a noticeable ribbon morphology even during the first extrusion (ϵ~3.2). This feature is especially pronounced in the 10 and 20 vol% Nb conductors. The higher volume percent conductors appear to have many contiguous Nb particles. The trend towards larger "islands" of Nb with increasing volume percent is exhibited in the measured Nb particle areas (Table 6.2). It was observed that the minimum Nb particle area was similar for all the conductors (4-8μm^2), while the maximum size varied widely (720-17,700μm^2) after the first extrusion. In addition to the broadened size range, some isolated matrix islands of Nb-Ti are evident in composites with higher volume fractions (especially the 40vol% conductor).

By the bundling size (ϵ~5), the Nb particles have developed a more complex, intercurled ribbon morphology. This tendency is stronger in the 10 and 20vol%Nb conductors than in the 30 and 40vol% conductors (Figure 6.3). In

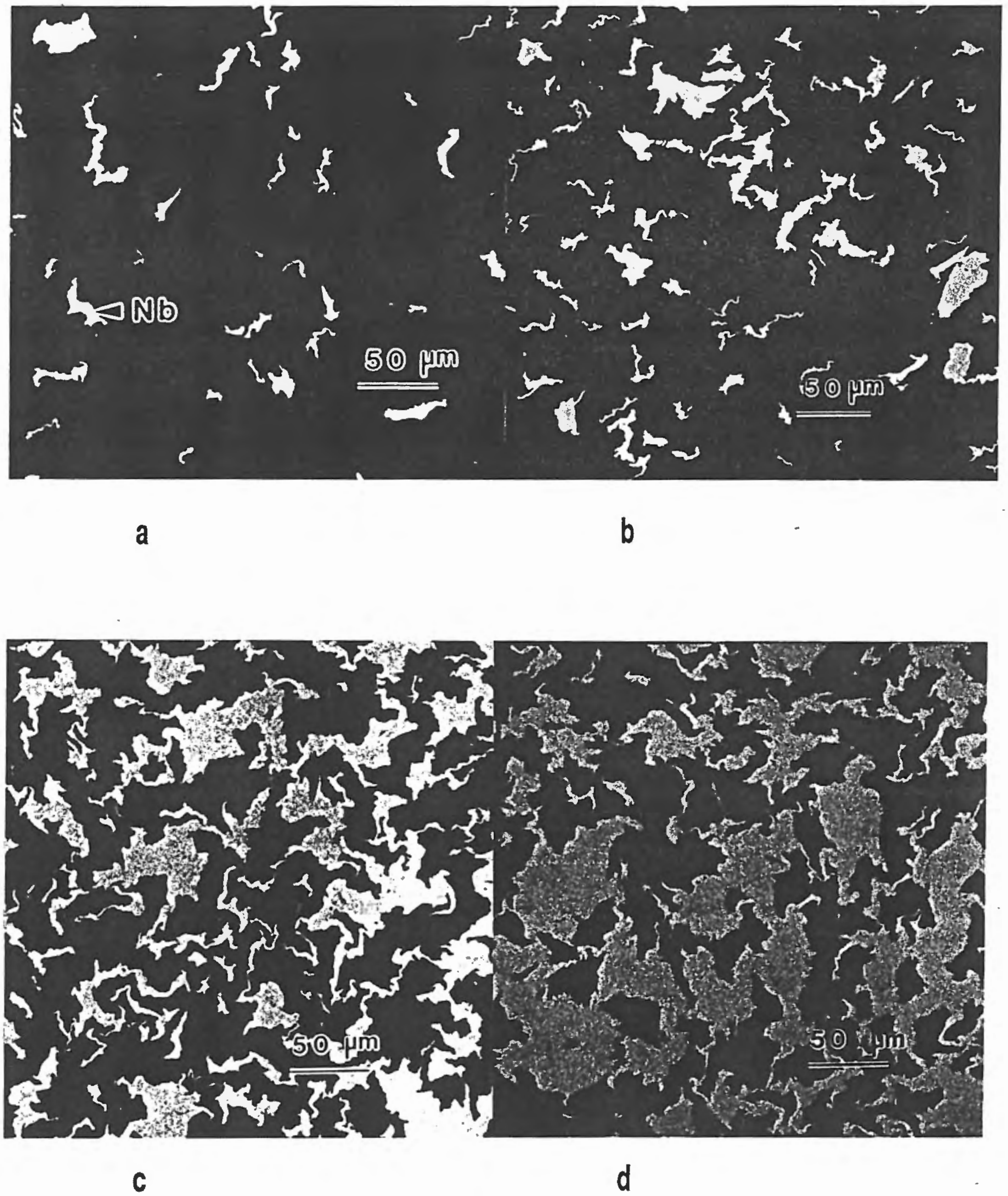

Figure 6.2: Transverse cross-section SEM backscatter micrographs showing the as-extruded ($\epsilon \sim 3.2$) microstructure in the composites with 10-40vol% Nb added; Nb-55wt%Ti + 10vol%Nb in (a), Nb-55wt%Ti + 20vol%Nb in (b), Nb-55wt%Ti + 30vol%Nb in (c), Nb-55wt%Ti + 40vol%Nb in (d).

Table 6.3: Interstitial Chemistry Analysis of the Starting Materials.

	Nb-55wt%Ti	Nb
H	8ppm	8ppm
N	220	30
O	1120	670
C	80	<30

Table 6.4: Powder Particle Size and Distribution.

PREP Nb-55wt%Ti	HGD Nb
−80 mesh ($< 180\mu m$), 100wt%	200 mesh ($> 75\mu m$), 1.5wt%
	270 ($> 53\mu m$), 51.0wt%
	325 ($> 45\mu m$), 43.5wt%
	-325 ($< 45\mu m$), 4.0wt%

Table 6.5: Interstitial Chemistry of the Bundled Filament Composites (ϵ>8).

Composite	N	O	C
10vol%Nb	140 ppm	1430 ppm	121 ppm
20	160	1180	108
30	140	1110	82
40	92	1060	112

addition, Nb-Ti islands are now less evident in the 30 and 40vol% conductors. All the bundled filament composites exhibited some Nb-poor regions (Figure 6.4) at the monofilament surface; however, the filament to filament Nb quantity appeared consistent.

Interstitial Chemistry Analyses

Table 6.3 shows the starting powder interstitial chemistries. After the conductors were processed into bundled filament conductors, samples from the front of the wires were sent to Teledyne Wah Chang for chemical analysis. At this stage of the process, the composites had received all their thermal treatments (two extrusions at ~250°C and the heat treatment of 800°C/2h, Figure 6.1) so that no further contamination was expected. In addition, the bundle incorporates material from the entire length of the original monofila-

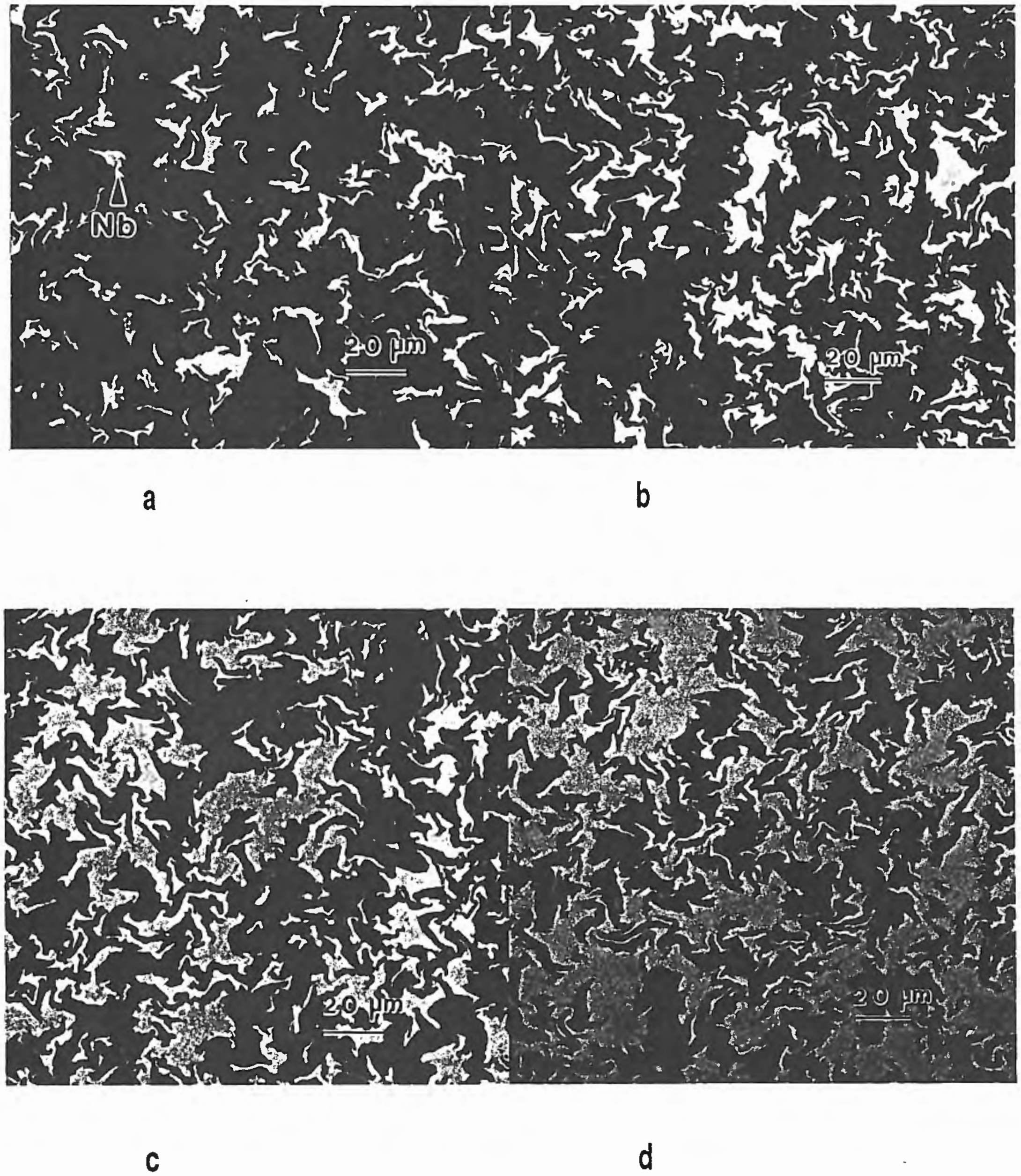

Figure 6.3: Transverse cross-section SEM backscatter micrographs showing the structure of the composites at the filament bundling size ($\epsilon \sim 5$); Nb-55-wt%Ti + 10vol%Nb in (a), Nb-55wt%Ti + 20vol%Nb in (b), Nb-55wt%Ti + 30vol%Nb in (c), Nb-55wt%Ti + 40vol%Nb in (d).

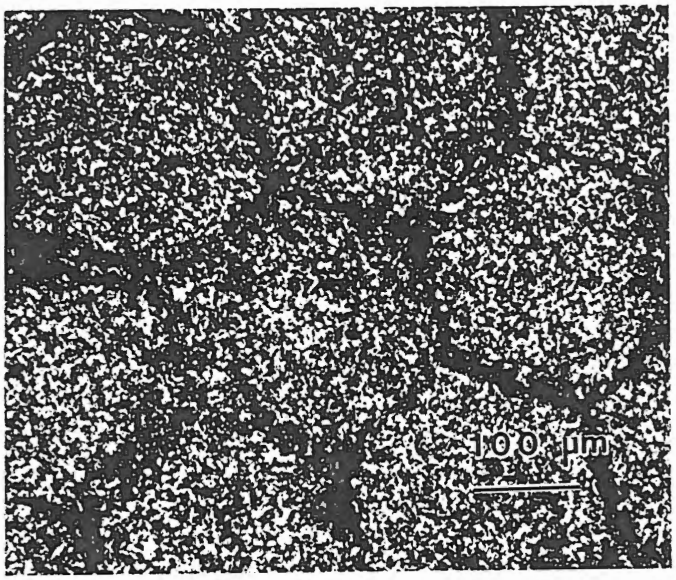

Figure 6.4: Transverse cross-section SEM backscatter micrograph of the 30-vol%Nb conductor at an overall composite diameter of 4mm ($\epsilon \sim 7.8$) showing the Nb-denuted zone which appears near the surface of each monofilament. This characteristic was seen in all the bundled filament composites.

ment, thus a chemical analysis at this stage should be representative of the total accumulation of contaminants in the whole composite. Table 6.5 shows that the carbon and nitrogen content in all the conductors was ~150ppm or less, while oxygen was ~1100ppm, except for the 10vol%Nb composite which had ~1400ppm oxygen.

t_{Nb} Measurements and Estimates

The characterization technique used for the microstructural quantification was one which described the thickness of each Nb particle by a single value. Since there were many Nb particles in each image and each varied in thickness, it is necessary to describe them in terms of an average particle thickness. The average Nb particle thickness was calculated from the particle area (A) and perimeter (p) measured from the conventional SEM images. To convert these measurements to a thickness, a shape transform was applied to the Nb particle. This shape transform converts the irregular shaped particle into a rectangular shape with the same area (A) and perimeter (p) as the original Nb particle. From the rectangular geometry we have:

$$A = t_{Nb} l_{Nb} \tag{6.3}$$

and

$$p = 2\left(t_{Nb} + l_{Nb}\right) \tag{6.4}$$

where t_{Nb} and l_{Nb} are the thickness and length of the rectangular equivalent, respectively. Thus it is a simple matter to use eqns. 6.3 and 6.4 to solve for t_{Nb} in terms of p and A:

$$t_{Nb} = \frac{p - \sqrt{p^2 - 16A}}{4} \tag{6.5}$$

Equation 6.5 gives the thickness of the rectangular equivalent of the original Nb particle. t_{Nb} calculated from eqn. 6.5 has been found to be in good agreement with the average particle thickness as measured by the line intercept method (see Discussion) and is one of the simplest microstructural characterization techniques [96]. Additional features of this technique will be presented in the Discussion.

Figures 6.5 through 6.8 show a series of plots of the average Nb particle thicknesses (t_{Nb}) for each of the images analyzed. The abscissa is the superconducting filament diameter, d, which is based on the equivalent monofilament diameter whether the data was taken from a monofilament or a bundled filament conductor. The equivalent strain is given at the top of the figures. The bars indicate the $t_{Nb}+/-2\sigma$ values for data taken from conductors with d >0.1mm. The data was fitted by linear regression in order to formulate the predictive t_{Nb} and $t_{Nb}+/-2\sigma$ lines according to

$$\log(t_{Nb}) = a + b\log(d) \tag{6.6}$$

shown in the figures. The coefficients to eqn. 6.6 are given in Table 6.6. The data below d~0.1mm on Figure 6.6 are from the TEM or FESEM images described in the previous chapter (Figures 5.8, 5.9, 5.10 and 5.11). The bars for the TEM and FESEM data sets indicate the full size range. As can be seen in the figures, t_{Nb} from the conventional SEM images diminished from ~4μm to 0.2μm as the conductor core is drawn from ~2mm to 0.1mm. At the same time the $t_{Nb}+/-2\sigma$ values ranged from a factor of ~10-50 to a factor of ~5-10; the smallest range was for the 10vol%Nb conductor and the largest for the 40vol%Nb conductor. Since the range of the $t_{Nb}+/-2\sigma$ values decreased with increasing strain, it would appear that the tendency was for the structures to become more uniform with increased strain. However, the range of the t_{Nb} values derived from the TEM and FESEM images on the 20-vol%Nb conductor was much larger than that predicted from the conventional SEM images. Figure 6.9 shows a comparison of the predictive t_{Nb} vs. d lines from the various conductors. As can be seen from the figure, the t_{Nb} line for the 10vol%Nb conductor is the steepest (i.e., quickest refining) while the t_{Nb} lines for the 20 and 30vol%Nb conductors are progressively less steep. The line for the 40vol%Nb conductor lies between those of the 10 and 20vol%Nb conductors.

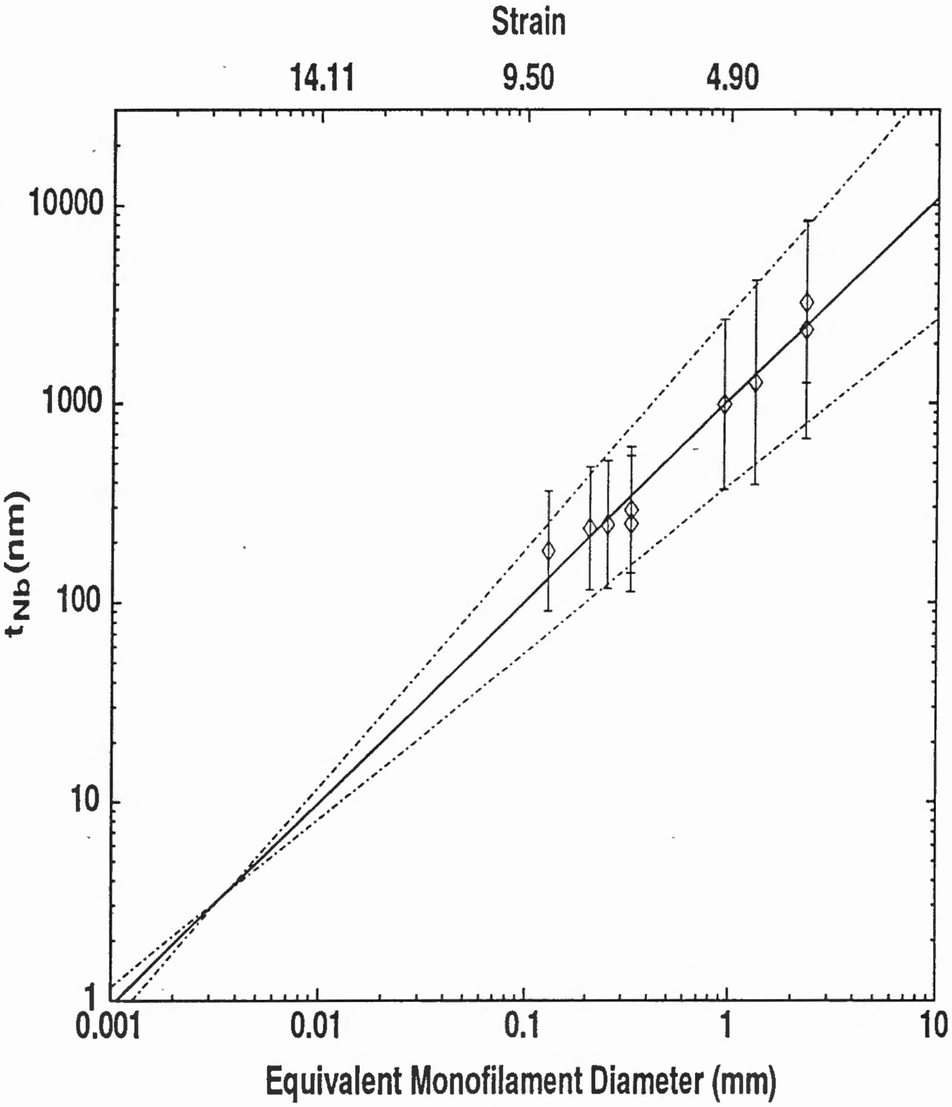

Figure 6.5: t_{Nb} vs. effective monofilament diameter for the 10vol%Nb conductor.

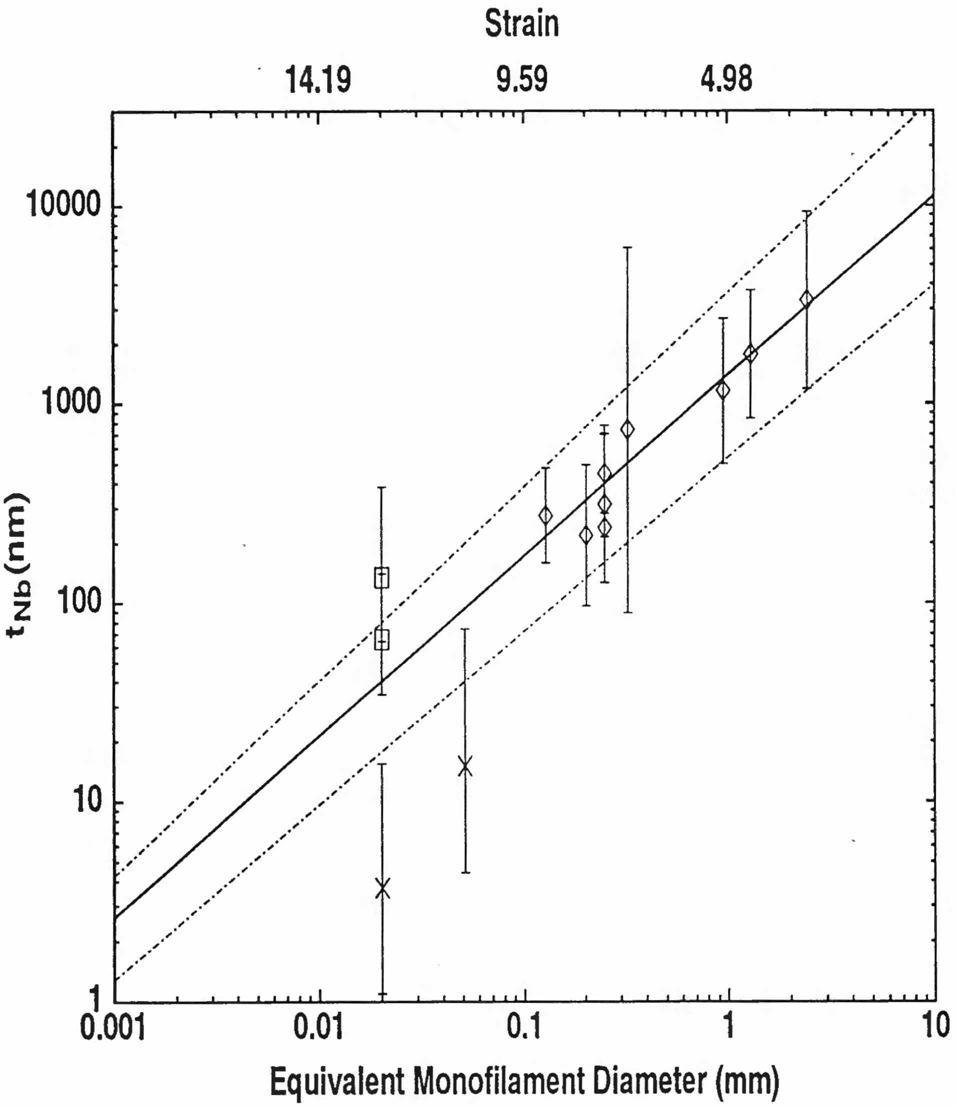

Figure 6.6: t_{Nb} vs. effective monofilament diameter for the 20vol%Nb conductor.

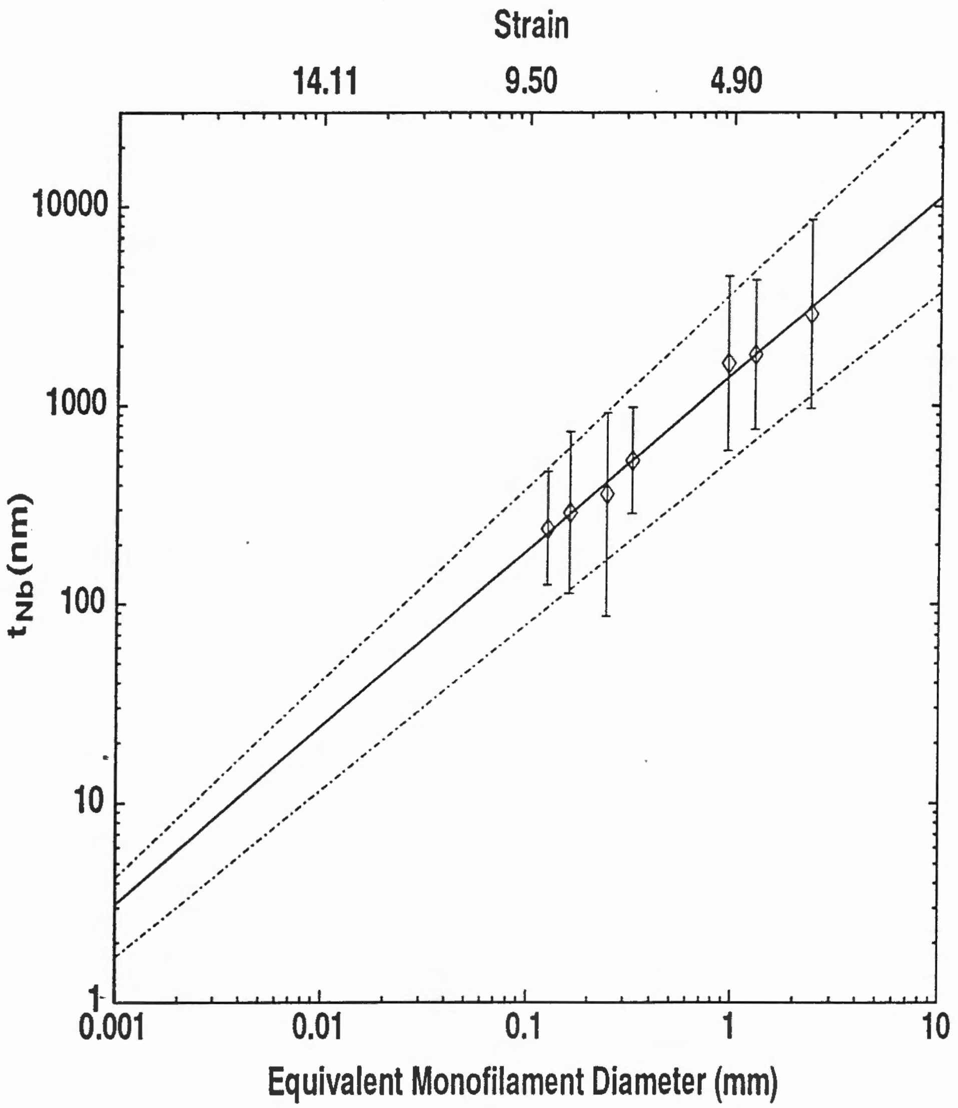

Figure 6.7: t_{Nb} vs. effective monofilament diameter for the 30vol%Nb conductor.

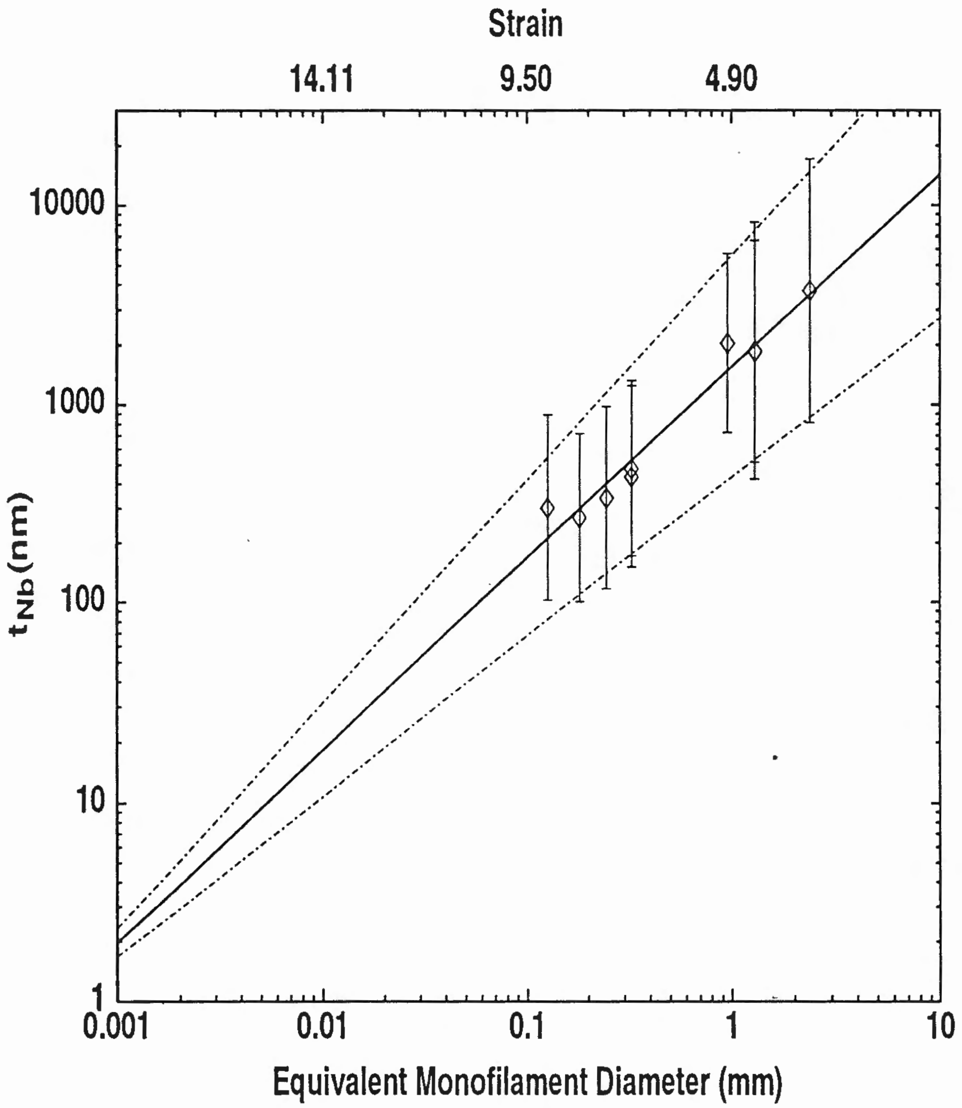

Figure 6.8: t_{Nb} vs. effective monofilament diameter for the 40vol%Nb conductor.

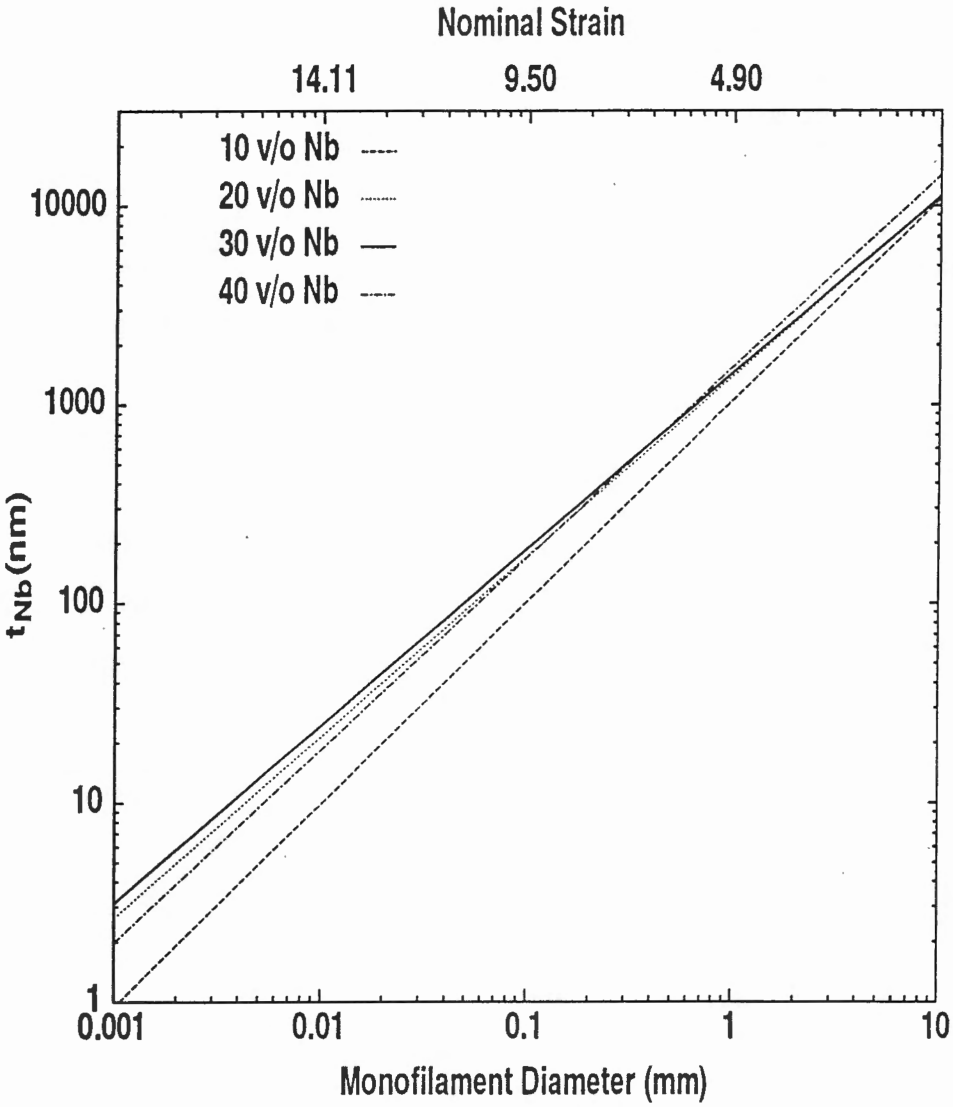

Figure 6.9: Comparison of the predictive lines of t_{Nb} vs. effective monofilament diameter for the 10-40vol%Nb conductors.

Table 6.6: Coefficients for the predictive t_{Nb} equations (eqn. 6.6) based on the image analysis results on the various composites are given along with the original monofilament core diameter (d_o).

$t_{Nb}(\mu m)$				$t_{Nb}-2\sigma(\mu m)$		$t_{Nb}+2\sigma(\mu m)$	
vol%Nb	$d_o(mm)$	a	b	a	b	a	b
10	2.311	0.0223	1.016	-0.411	0.840	0.456	1.193
20	2.413	0.144	0.908	-0.271	0.873	0.560	0.978
30	2.360	0.162	0.889	-0.264	0.836	0.573	0.982
40	2.362	0.192	0.965	-0.364	0.803	0.748	1.126

6.2.2 Superconducting Properties

Figures 6.11 through 6.14 show how the $J_c(B)$ of the various PM APC conductors increases as they are strained from ~7 to optimum J_c sizes of ϵ~13-14. The Nb-55wt%Ti + 0vol%Nb control was tested in the strain range of 12 to 15 (Figure 6.10). We see in Figure 6.10 that without the addition of Nb pinning centers J_c always remained less than $1000A/mm^2$, and there was only a weak tendency for J_c to increase with increasing strain. In stark contrast to these results are the $J_c(B)$ of the PM APC conductors. For example, in the 10vol%Nb conductor (Figure 6.11) J_c strongly increases above $1000A/mm^2$ for strains larger than ~10. More substantial increases in J_c are observed in conductors with larger amounts of Nb (Figures 6.12 through 6.14). It is also noted that even at the lowest strain of ~7 there is an increase in J_c(1T) over the 0vol%Nb control, rising to nearly $2000A/mm^2$ in the 40vol%Nb conductor. Figure 6.15 summarizes the $J_c(B)$ results once the conductors have reached their maximum J_c(5T). This figure graphically illustrates the J_c enhancement as Nb second phase is added. It can be seen that the J_c varies considerably from about $900A/mm^2$ at 1T for the Nb-55wt%Ti + 0vol%Nb control composite to ~$15000A/mm^2$ at 1T for the Nb-55wt%Ti + 40vol%Nb composite.

Figures 6.16 through 6.20 show J_c(5T) vs. ϵ through a strain range of

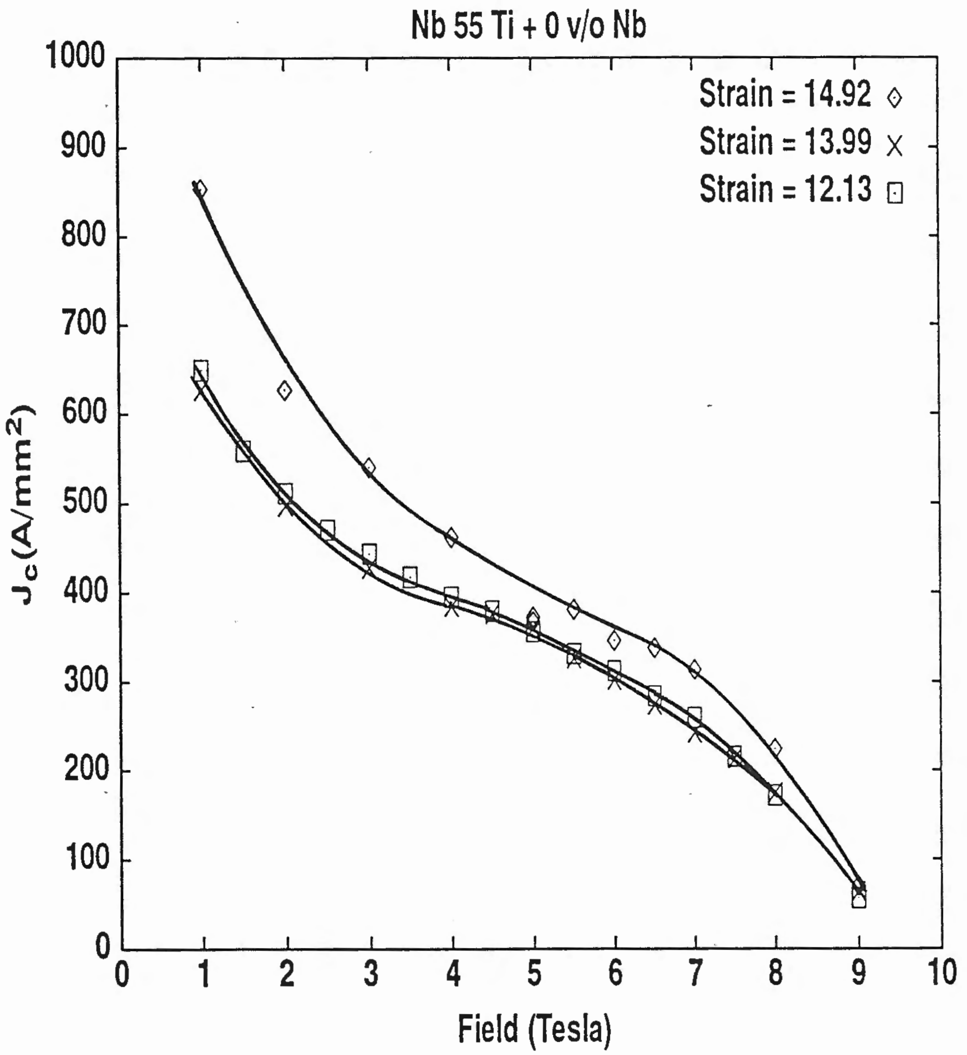

Figure 6.10: J_c vs. Field for the Nb-55wt%Ti + 0vol%Nb conductor at different fabrication strains.

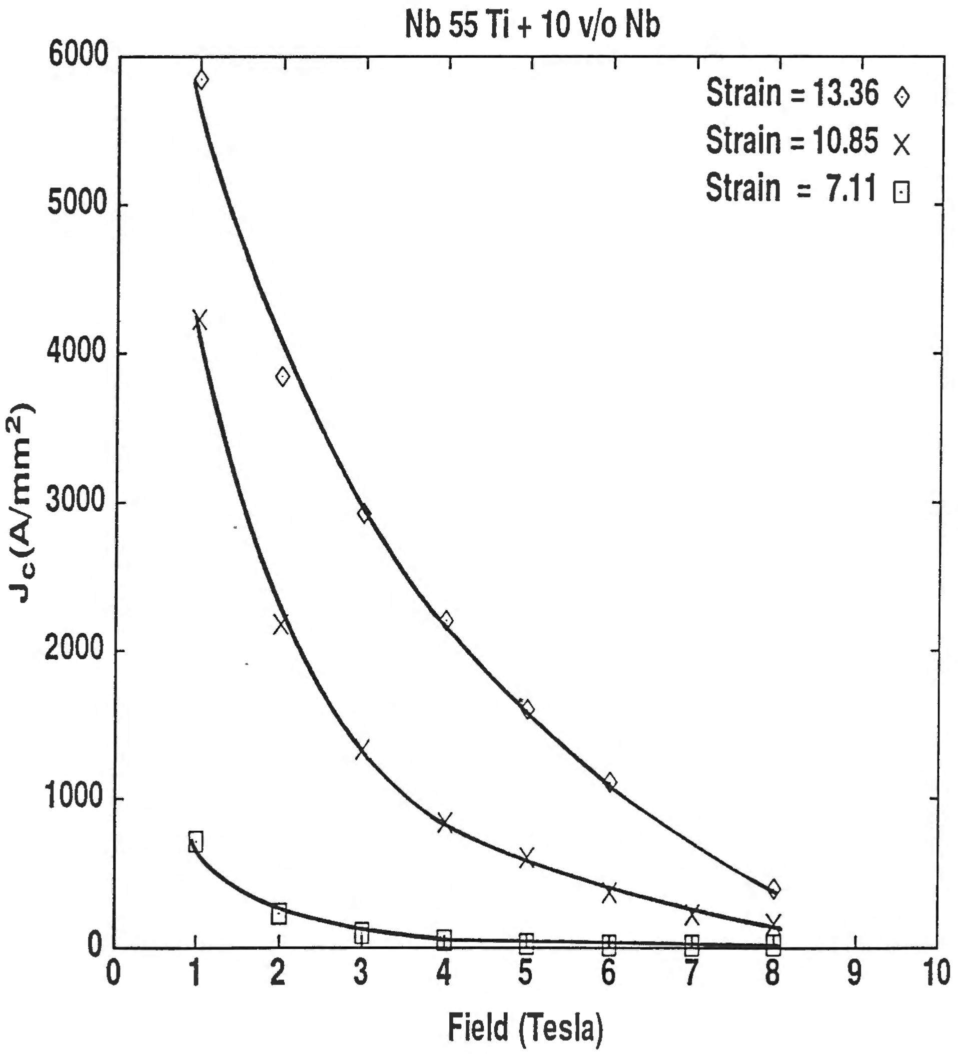

Figure 6.11: J_c vs. Field for the Nb-55wt%Ti + 10vol%Nb conductor at different fabrication strains.

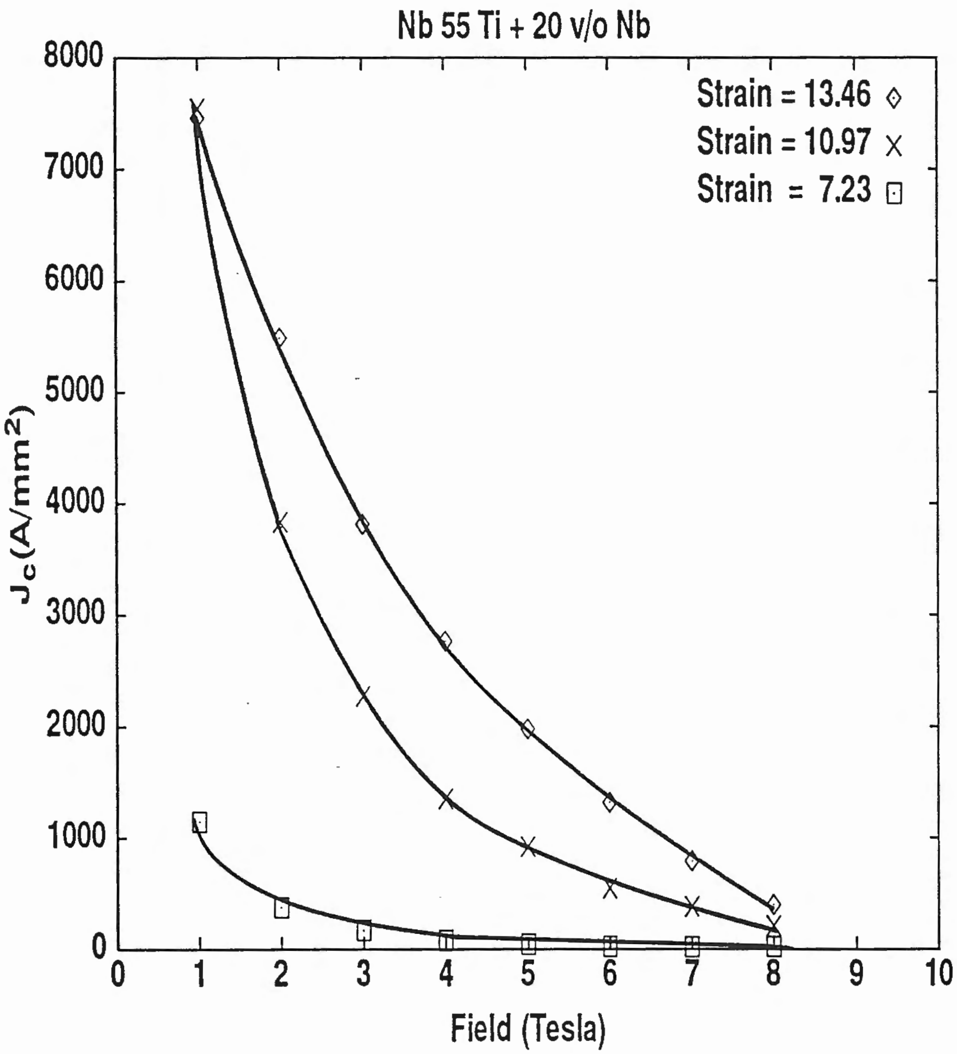

Figure 6.12: J_c vs. Field for the Nb-55wt%Ti + 20vol%Nb conductor at different fabrication strains.

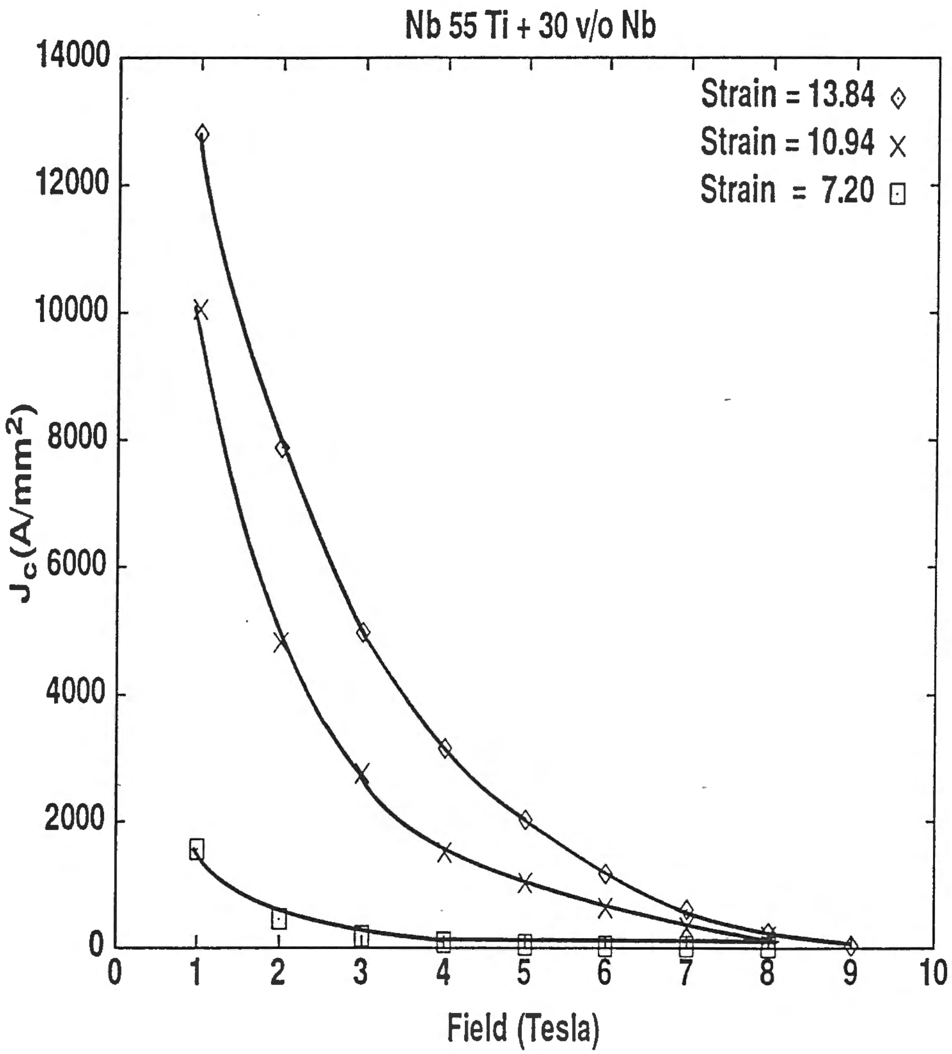

Figure 6.13: J_c vs. Field for the Nb-55wt%Ti + 30vol%Nb conductor at different fabrication strains.

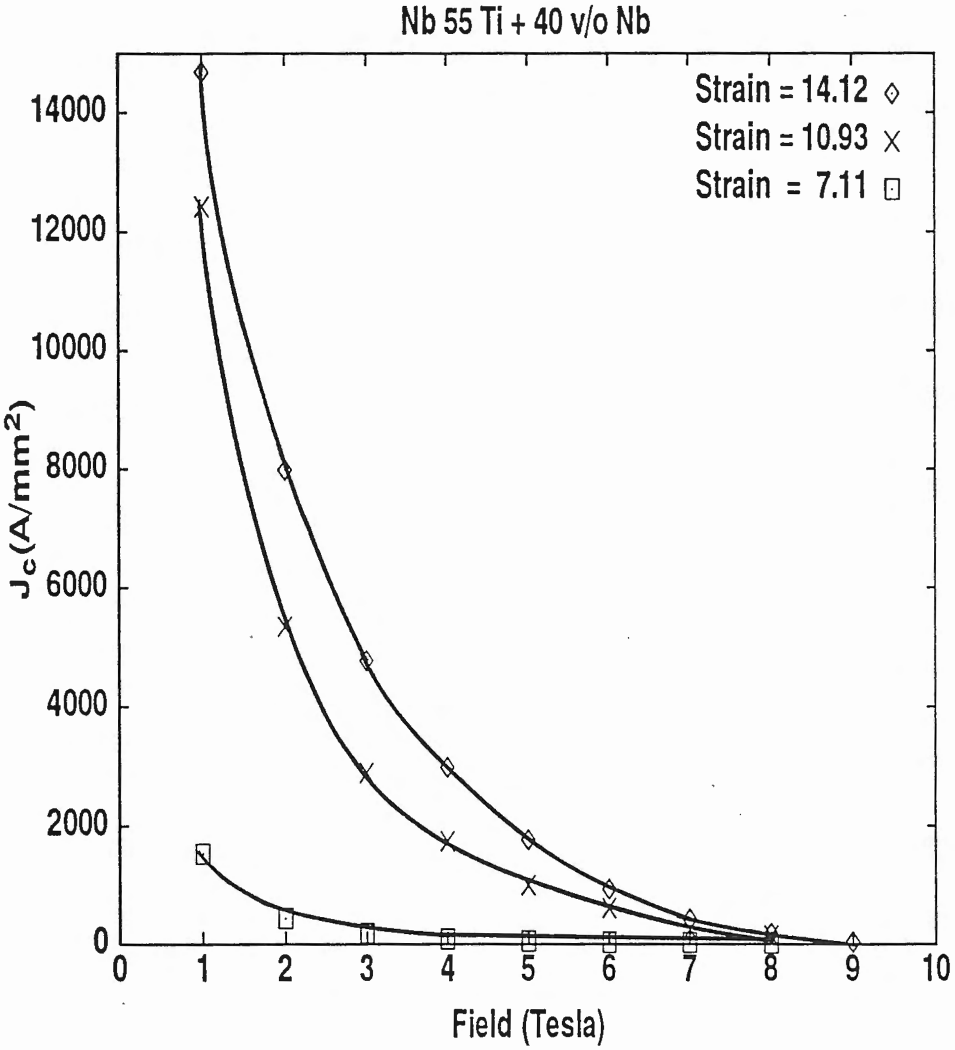

Figure 6.14: J_c vs. Field for the Nb-55wt%Ti + 40vol%Nb conductor at different fabrication strains.

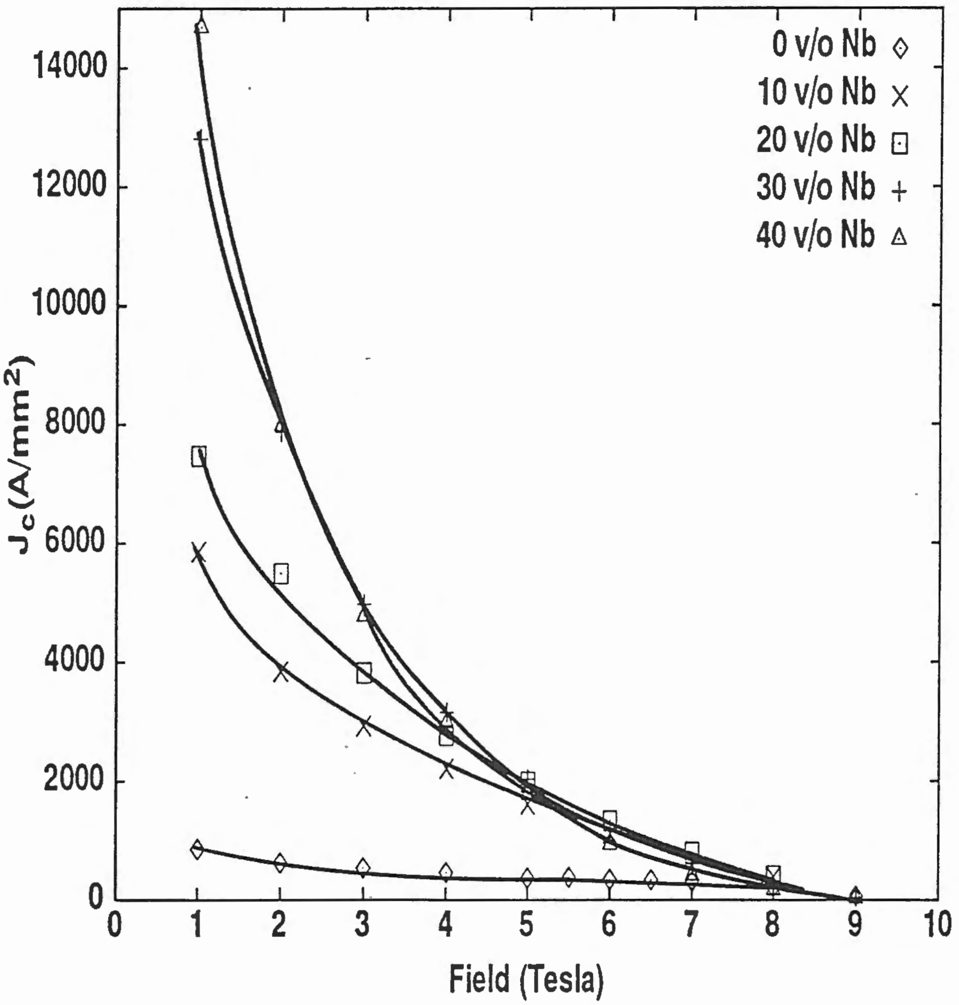

Figure 6.15: The J_c vs. Field is compared for the Nb-55wt%Ti + 0-40vol%Nb conductors at the size at which they have reached their peak J_c(5T).

~7 to 16 for the PM APC conductors and strains of 12 to 15 for the 0-vol%Nb control. We observed in all of the PM APC conductors that J_c increased steeply for strains of ~10 to 13. The J_c for all of the conductors reached a maximum for ϵ~13 to 14. A relatively shallow maximum in J_c of $\Delta\epsilon$~1 wide was typically observed, beyond which further refinement of the microstructure led to a fall off in J_c. Maximum J_c(5T) values were obtained for t_{Nb} values of 14, 30, 28, and 23nm for the 10-40vol%Nb conductors. These t_{Nb} values are given in Figures 6.17 through 6.20 along with t_{Nb} at ϵ~7. t_{Nb} corresponding to strain is given at the top of the figures.

The effect of additions of the Nb pinning center volume percent on the critical current density for fields of 1-8T are shown in Figures 6.21 through 6.28. The enhancement in J_c at low fields is enormous, J_c(1T) rising from ~800 to $16000A/mm^2$ and J_c(3T) rising from ~500 to $5000A/mm^2$ with additions of Nb through 40 volume percent. For fields greater than 3T we see a gradual downturn in J_c with the larger additions of Nb pinning centers, such that a peak is observed in the plots of J_c vs. vol%Nb. The peak J_c gradually shifts to lower volume percent Nb with increasing field such that J_c(8T) falls with additions greater than 10vol%Nb; these results are summarized in Table 6.7.

In order to directly compare the combined effects of variable volume percent Nb and different fields on J_c, we show the normalized critical current

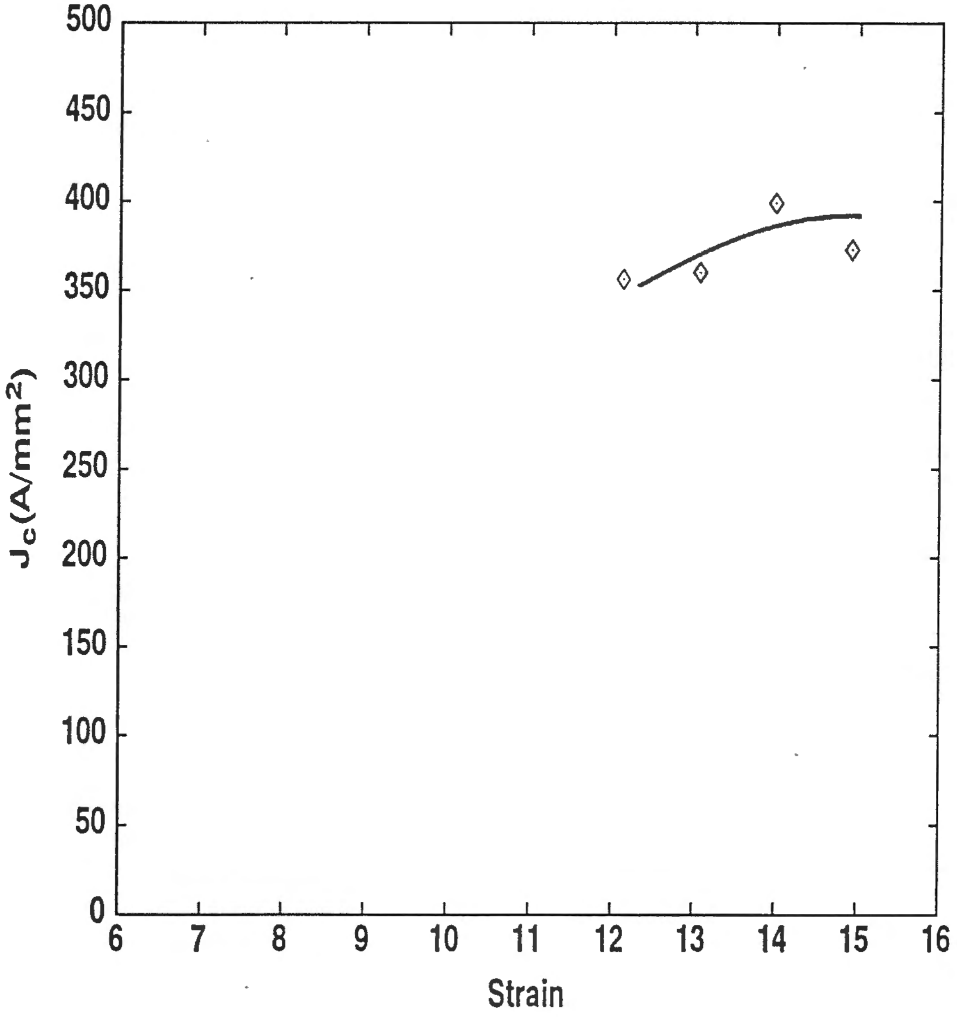

Figure 6.16: J_c(5T) vs. the fabrication strain of the Nb-55wt%Ti + 0vol%Nb conductor.

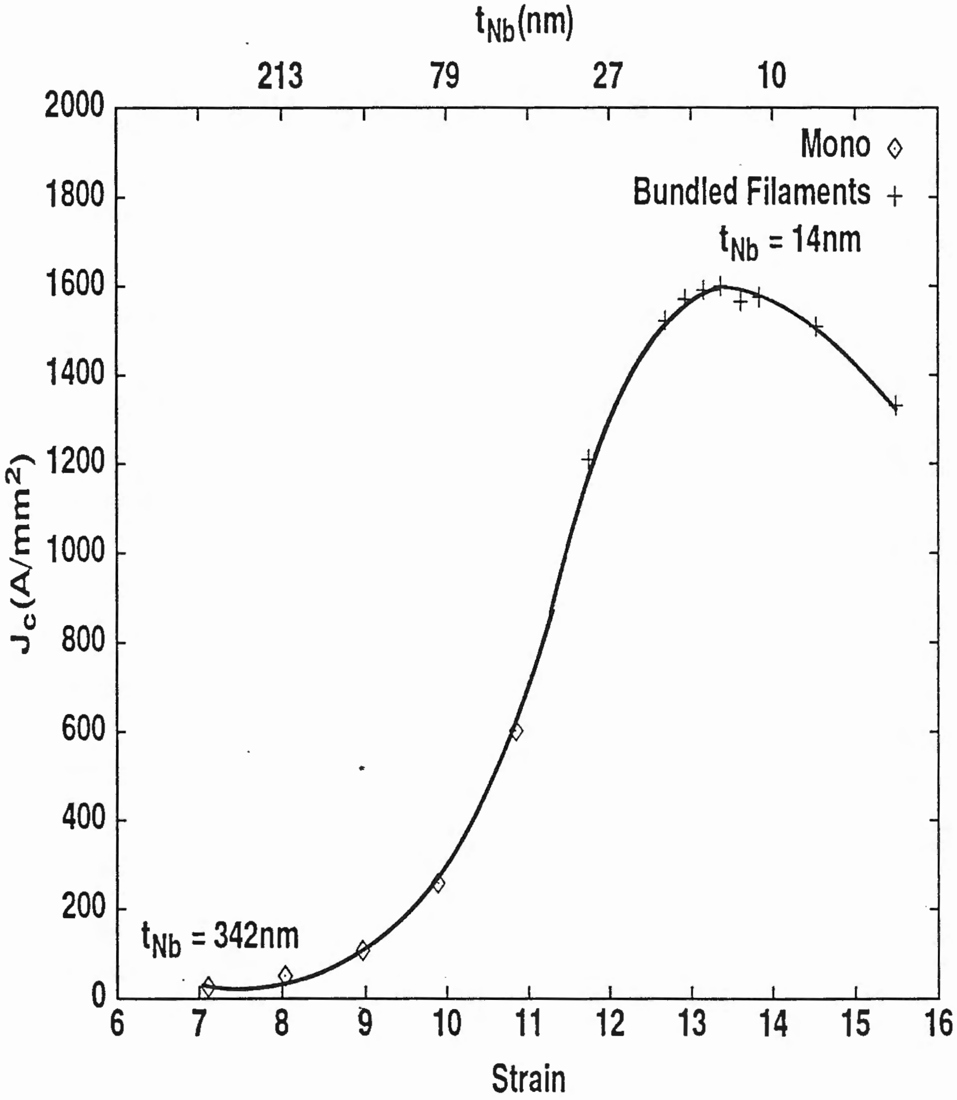

Figure 6.17: J_c(5T) vs. the fabrication strain of the Nb-55wt%Ti + 10-vol%Nb conductor. The t_{Nb} values are given at ϵ~7 and peak J_c(5T). t_{Nb} corresponding to strain is given at the top of the figure.

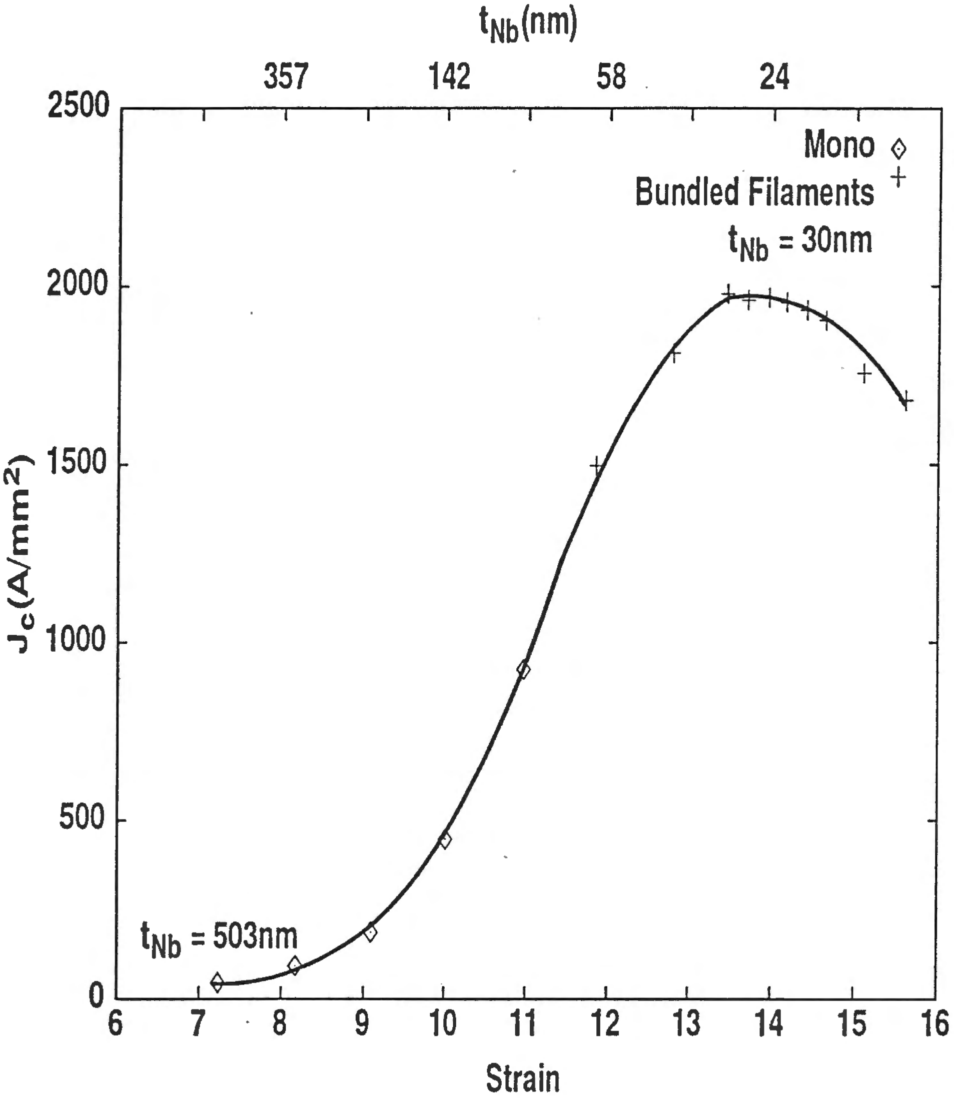

Figure 6.18: J_c(5T) vs. the fabrication strain of the Nb-55wt%Ti + 20-vol%Nb conductor. The t_{Nb} values are given at ϵ~7 and peak J_c(5T). t_{Nb} corresponding to strain is given at the top of the figure.

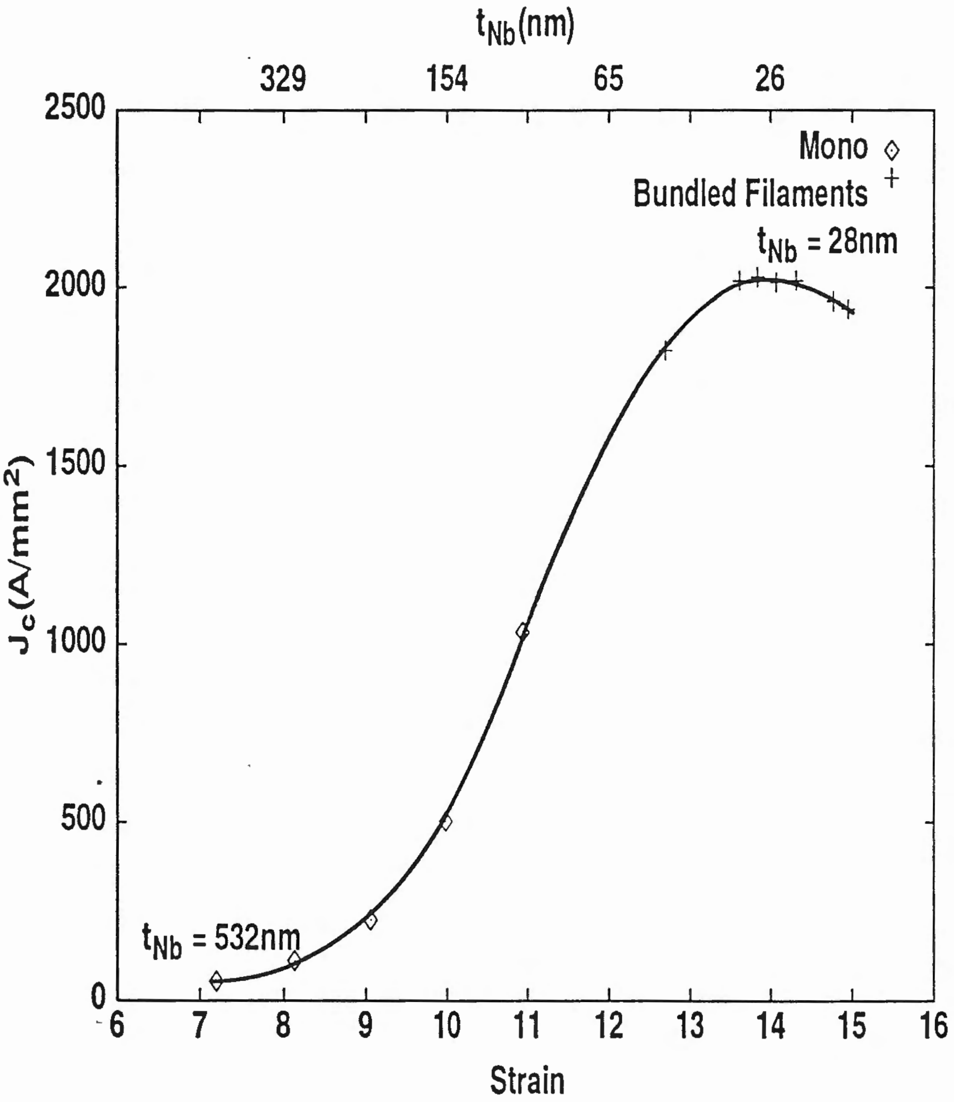

Figure 6.19: J_c(5T) vs. the fabrication strain of the Nb-55wt%Ti + 30-vol%Nb conductor. The t_{Nb} values are given at ϵ~7 and peak J_c(5T). t_{Nb} corresponding to strain is given at the top of the figure.

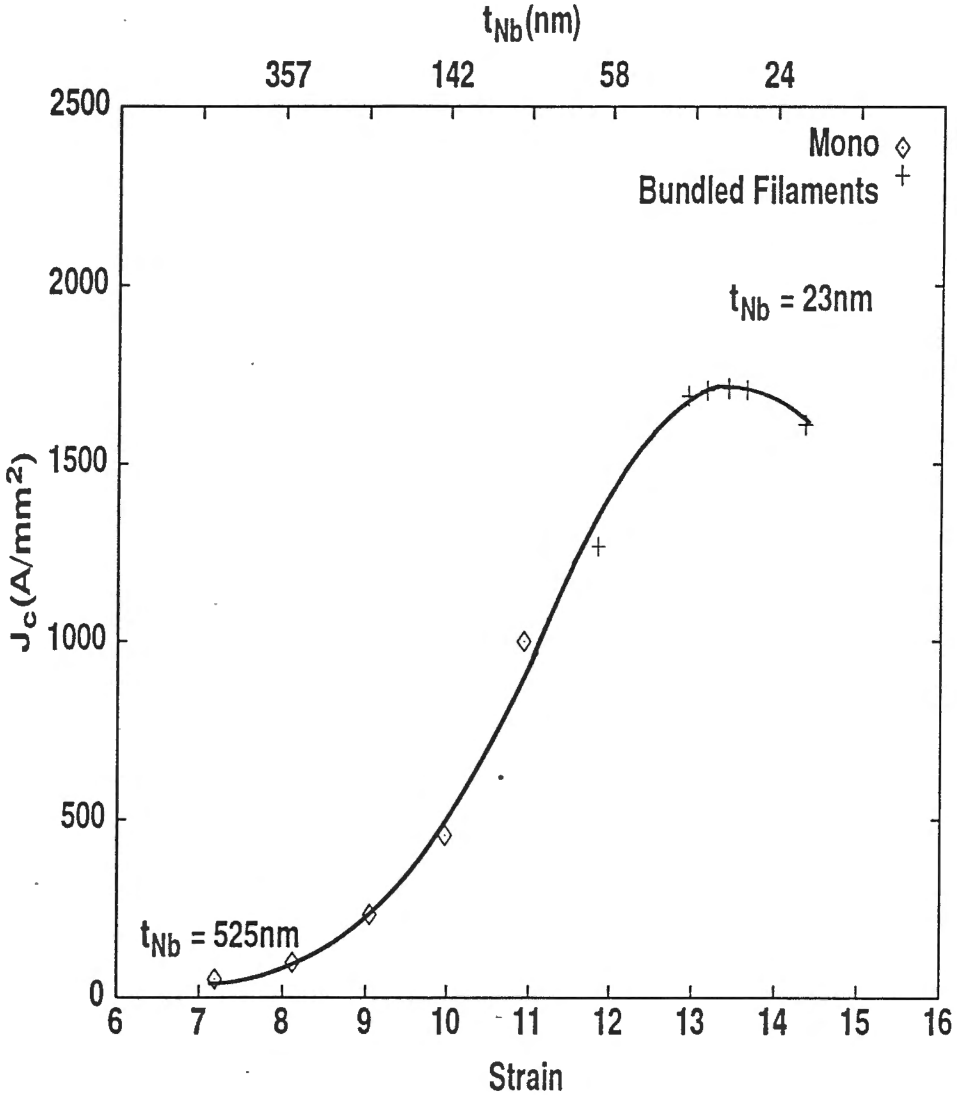

Figure 6.20: J_c(5T) vs. the fabrication strain of the Nb-55wt%Ti + 40-vol%Nb conductor. The t_{Nb} values are given at $\epsilon \sim 7$ and peak J_c(5T). t_{Nb} corresponding to strain is given at the top of the figure.

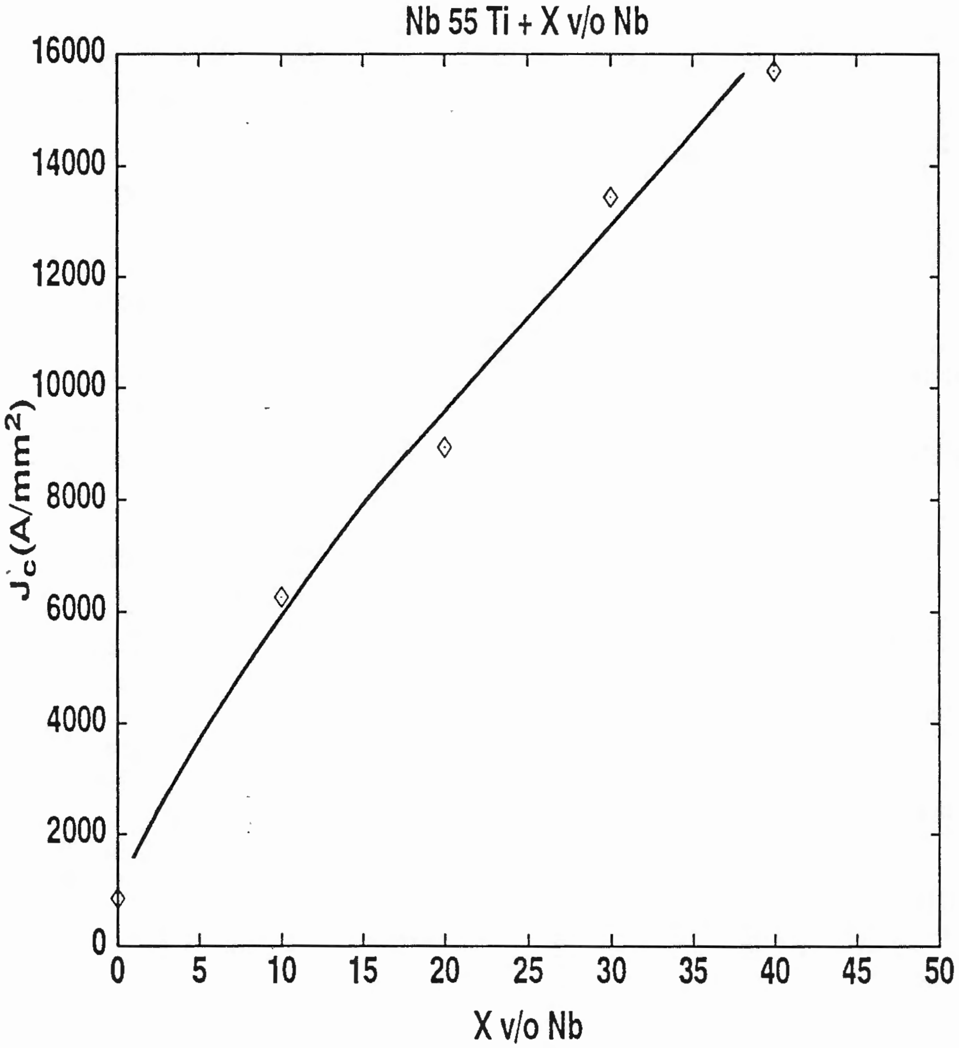

Figure 6.21: Peak J_c(1T) vs. volume percent Nb added to Nb-55wt%Ti is shown.

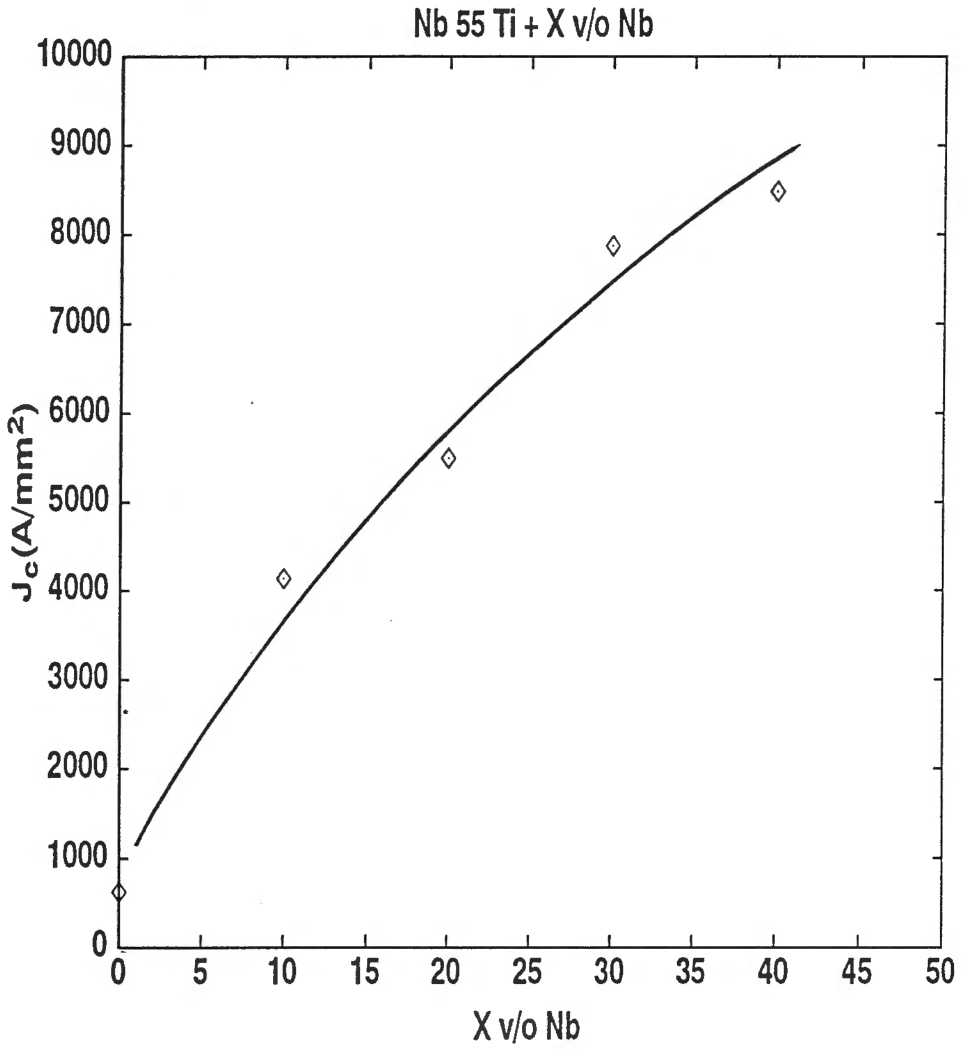

Figure 6.22: Peak J_c(2T) vs. volume percent Nb added to Nb-55wt%Ti is shown.

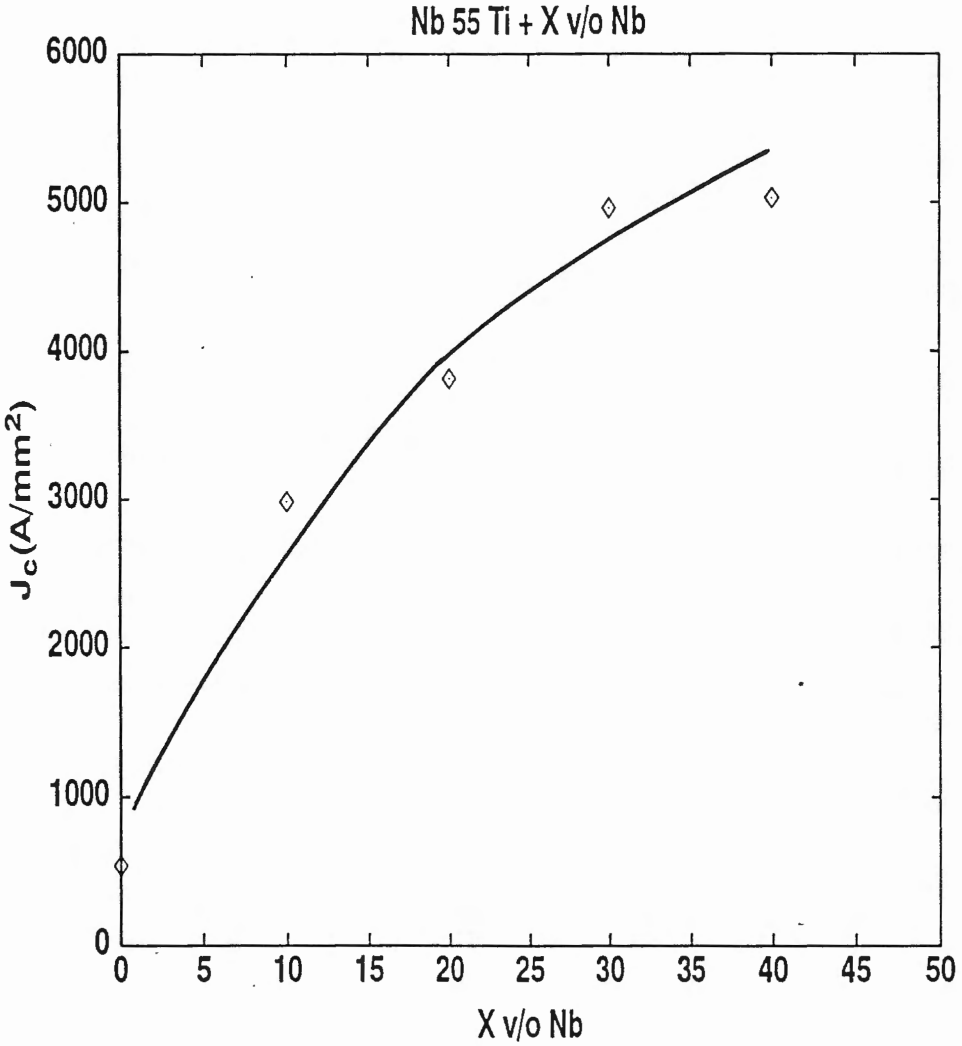

Figure 6.23: Peak J_c(3T) vs. volume percent Nb added to Nb-55wt%Ti is shown.

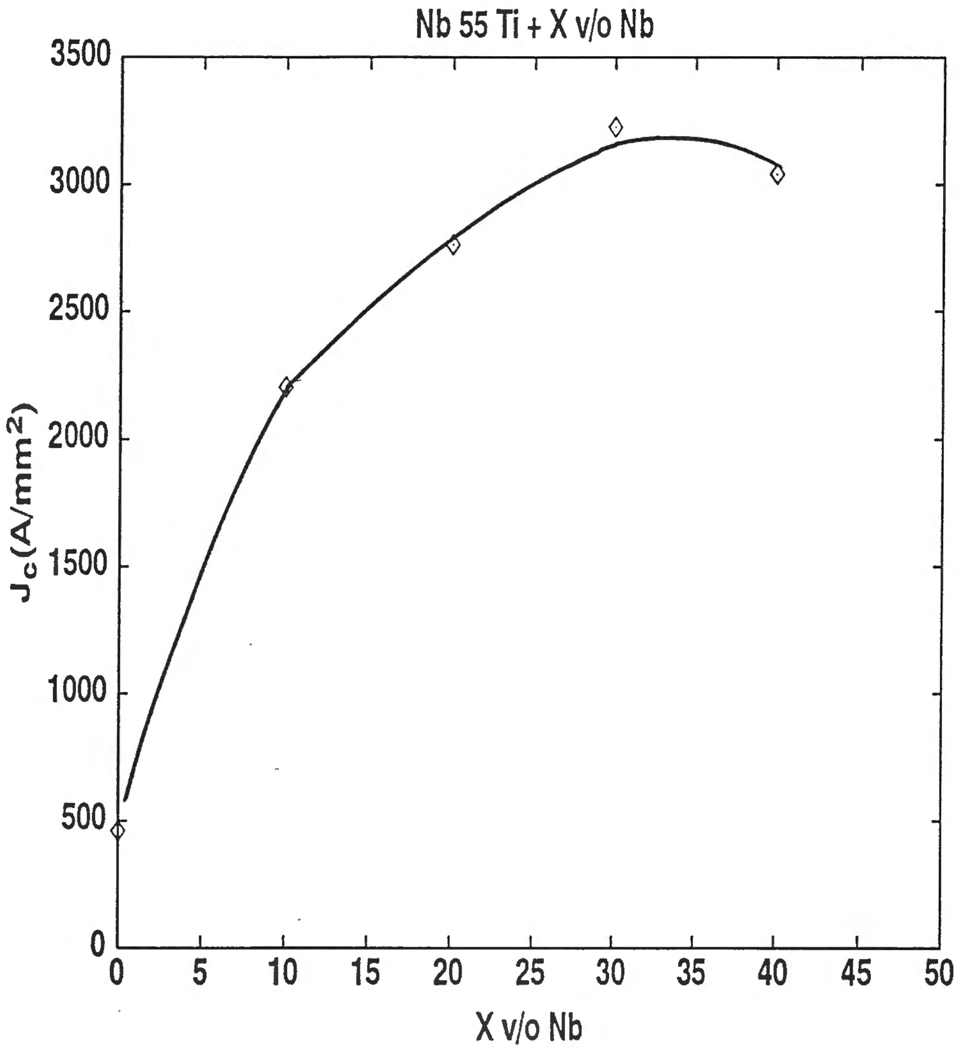

Figure 6.24: Peak J_c(4T) vs. volume percent Nb added to Nb-55wt%Ti is shown.

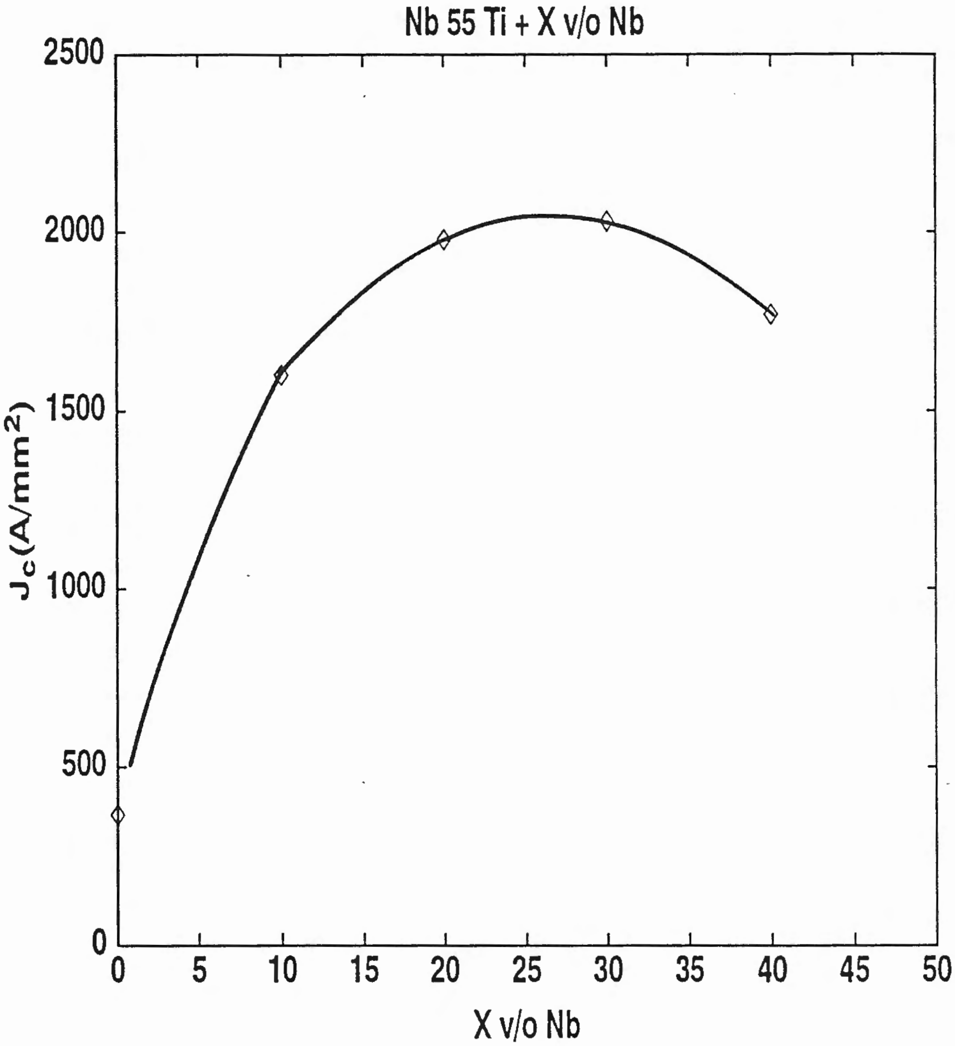

Figure 6.25: Peak J_c(5T) vs. volume percent Nb added to Nb-55wt%Ti is shown.

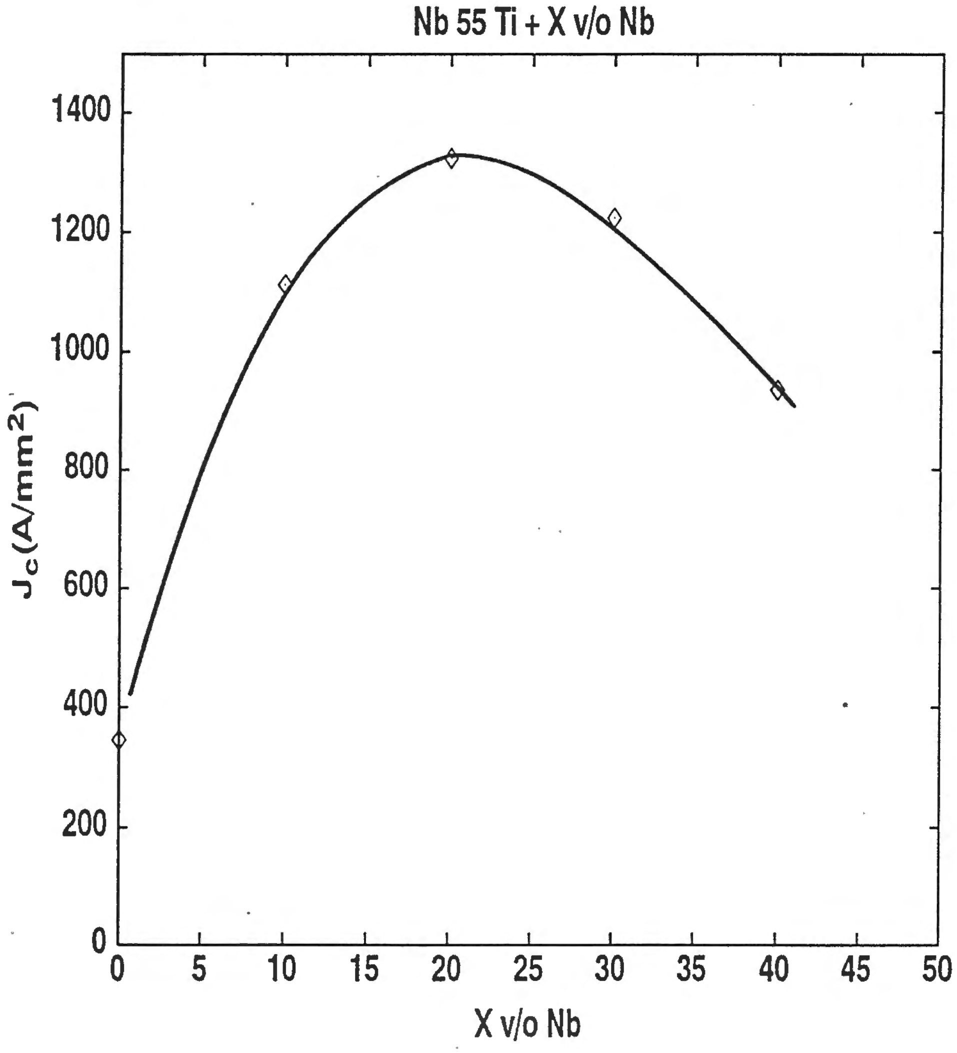

Figure 6.26: Peak J_c(6T) vs. volume percent Nb added to Nb-55wt%Ti is shown.

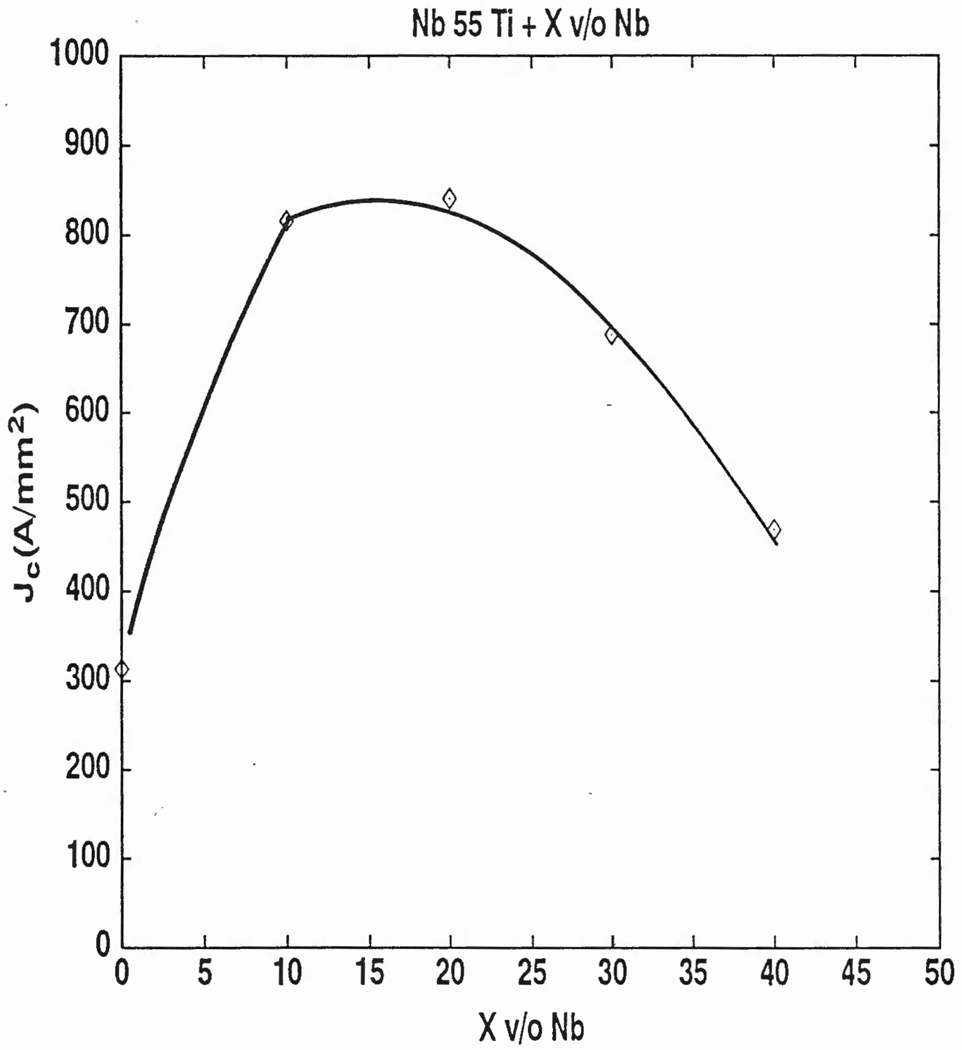

Figure 6.27: Peak J_c(7T) vs. volume percent Nb added to Nb-55wt%Ti is shown.

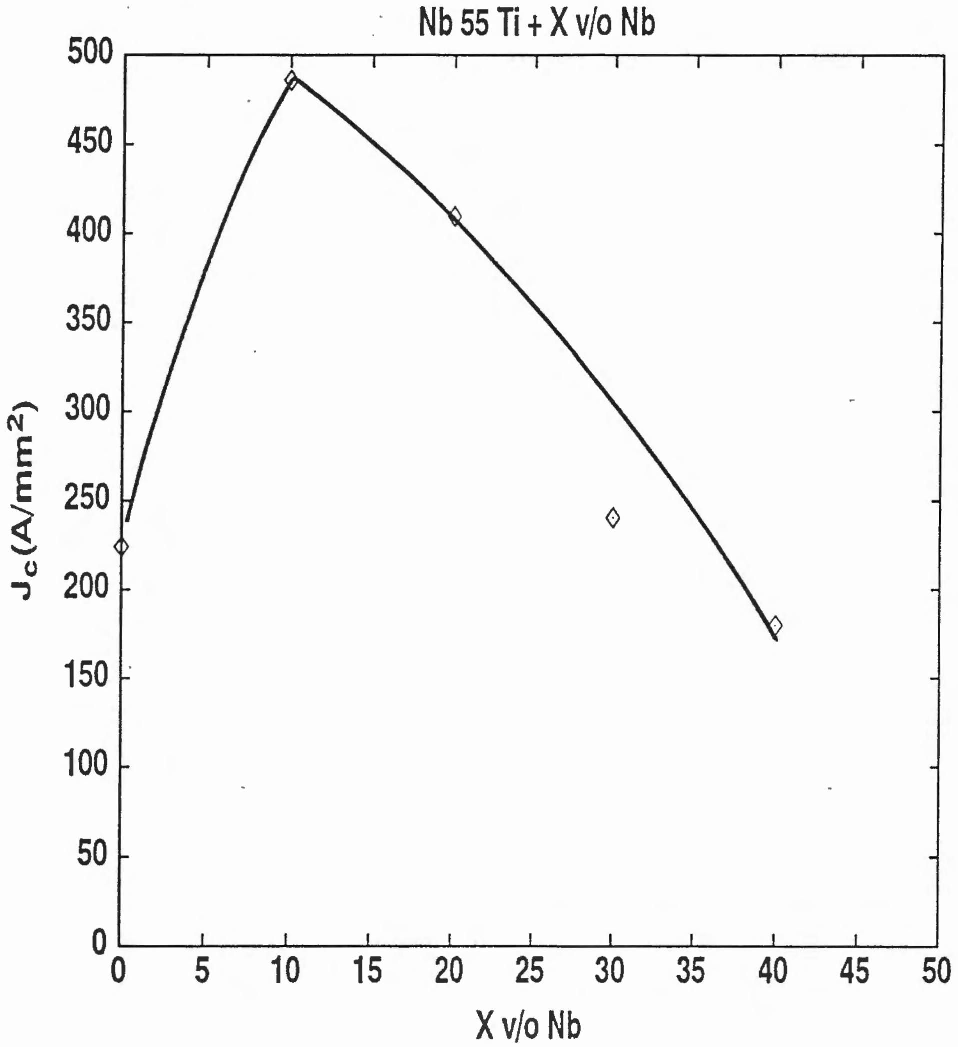

Figure 6.28: Peak J_c(8T) vs. volume percent Nb added to Nb-55wt%Ti is shown.

Table 6.7: Peak measured J_c values for Fields of 1-8T.

Field (T)	vol%Nb added	Peak $J_c(A/mm^2)$
1	40	15,700
2	40	8,482
3	40	5,030
4	30	3,230
5	30	2,030
6	20	1,320
7	20	840
8	10	490

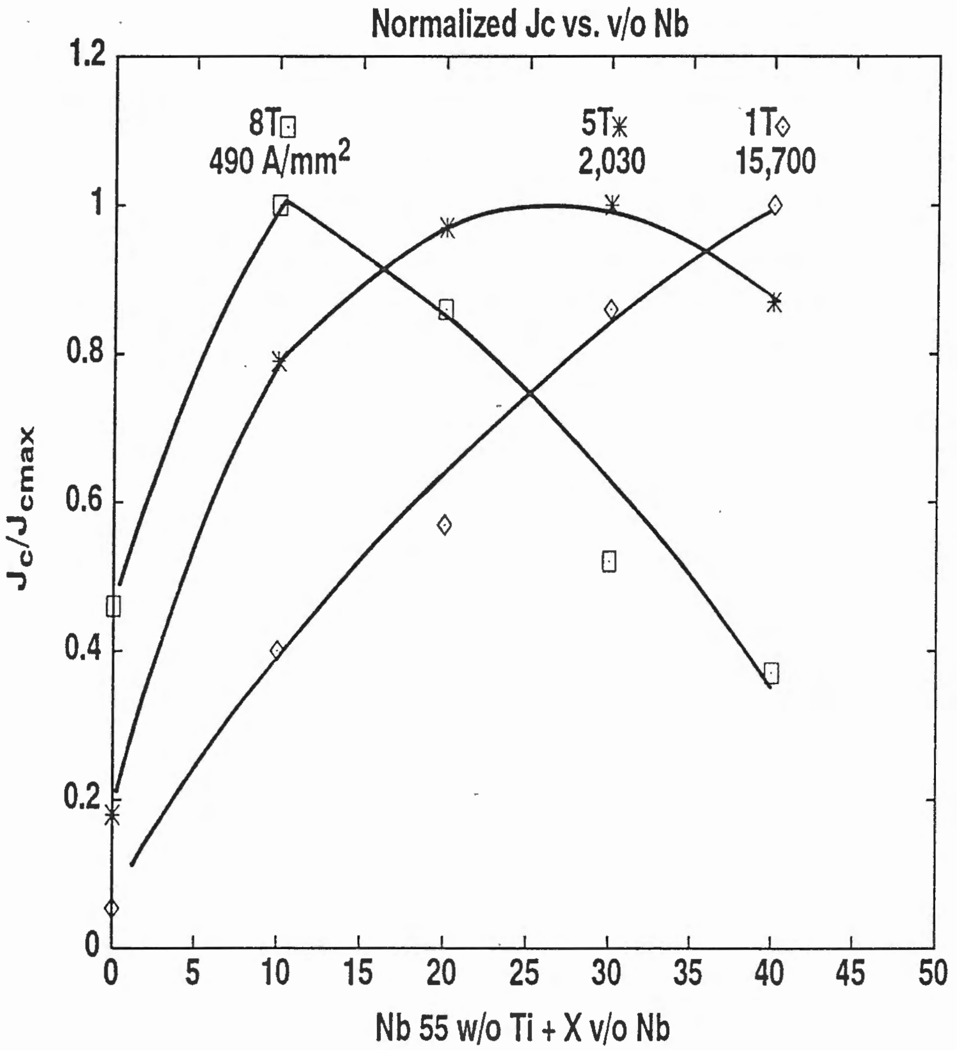

Figure 6.29: Normalized J_c at 1, 5, and 8T vs. vol% Nb added. The maximum values observed are given in the figure.

Table 6.8: Extrapolated B_{c_2} (for peak F_p(5T)) and Predicted B_{c_2} [83] and T_c [83] Based on the Overall Composition of the Conductors.

vol%Nb	Overall Composition	T_c(K)	B_{c_2}(T)	B_{c_2}(T) from F_p curves
0	Nb-55wt%Ti	8.3	9.7	9.5
10	Nb-47.0wt%Ti	8.6	10.7	9.8
20	Nb-39.9wt%Ti	9.1	10.7	9.3
30	Nb-33.3wt%Ti	9.3	9.9	9.0
40	Nb-27.3wt%Ti	9.7	8.7	8.4

densities at 1, 5, and 8T vs. vol% Nb in Figure 6.29. Again we see that while the 1T J_c values show a monotonic increase with additions of Nb through 40vol%, the 5T results peak between 20-30vol% and the 8T values fall off when more than ~10vol% Nb is added.

Another way to consider these results is to look at the F_p vs. B results having the best F_p(5T) for each of the volume percentages (Figure 6.30). Here we see that the general trend is one of increasing F_p with increasing volume percent Nb added with an attendant shift in $F_{p_{max}}$ towards lower fields. Also note the decreasing B_{c_2} which is predicted from considerations of the overall compositions as they become increasingly Nb-rich (Table 6.8).

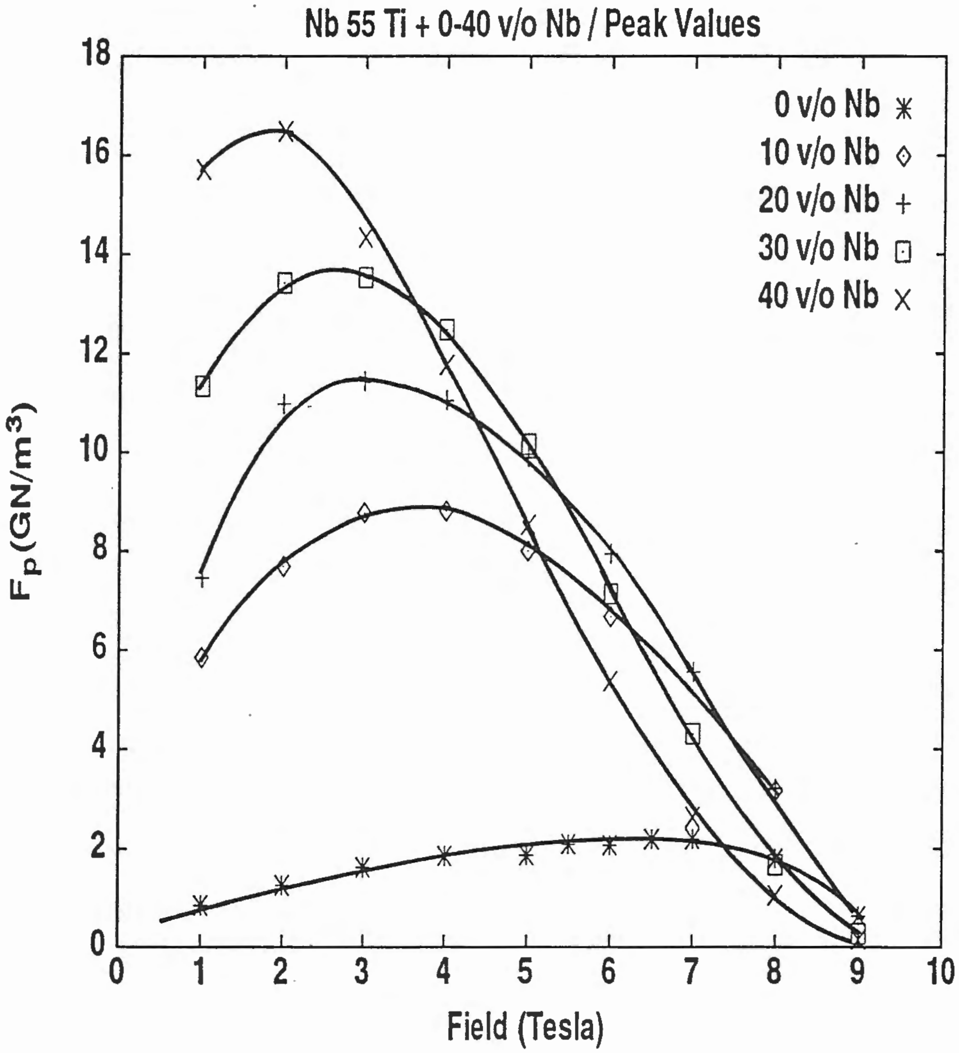

Figure 6.30: Pinning force curves for the wires having maximum values of J_c(5T).

It is interesting to examine the F_p performances of the conductors before the maximum J_c(5T) is reached, i.e., pre-peak. In Figure 6.31 we show a comparison of the 10-40vol%Nb conductors when the t_{Nb} is ~50nm (the estimated thicknesses are given in the figure). What we observe is that the 10vol%Nb conductor has the lowest F_p up to ~8T, while the 30vol%Nb conductor has the highest F_p up to ~7T. F_p for all the conductors peaks at very low fields, i.e., $F_{p_{max}}$ occurs between 1-2T.

The post-peak $F_p(B)$ curves are also worthy of examination. Figure 6.32 compares the 10-40vol%Nb conductors when t_{Nb}~5-17nm. We observe an important evolution in the shape of the $F_p(B)$ curve at these higher strains. $F_{p_{max}}$ for the 40vol%Nb is highest below 2T, 30vol%Nb peaks at about 3T, 20vol%Nb peaks at ~4T, and 10vol%Nb peaks at ~5T.

The movement of $F_{p_{max}}$ to higher fields is a pronounced function of strain, as shown in Figures 6.33 through 6.36. The general trend is for $F_{p_{max}}$ to shift to higher fields as t_{Nb} is refined. In the 10vol%Nb conductor, F_p increases at all fields and $F_{p_{max}}$ moves from ~1T to ~3-4T as t_{Nb} diminishes to ~14nm (Figure 6.33). With further refinement of t_{Nb}, $F_{p_{max}}$ moves to ~5T and F_p falls for fields below ~6T. In the 20vol%Nb conductor, F_p increases at all fields and $F_{p_{max}}$ moves from ~1T to ~3T with refinement of t_{Nb} to ~30nm (Figure 6.34). Further refinement of t_{Nb} shifts $F_{p_{max}}$ to ~4-5T, but at the expense of low field F_p (i.e., low field F_p decreases). In the 30 and 40vol%-

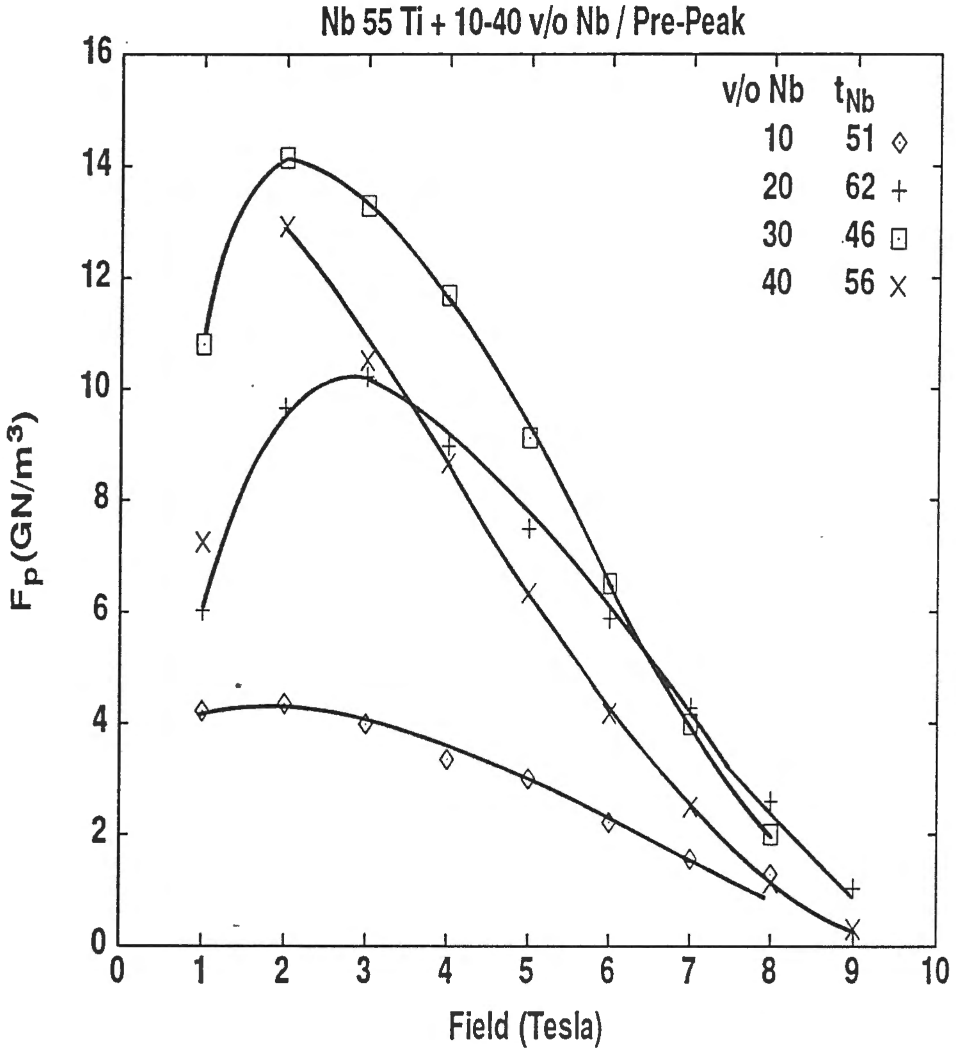

Figure 6.31: $F_p(B)$ for the various conductors when t_{Nb}~50nm.

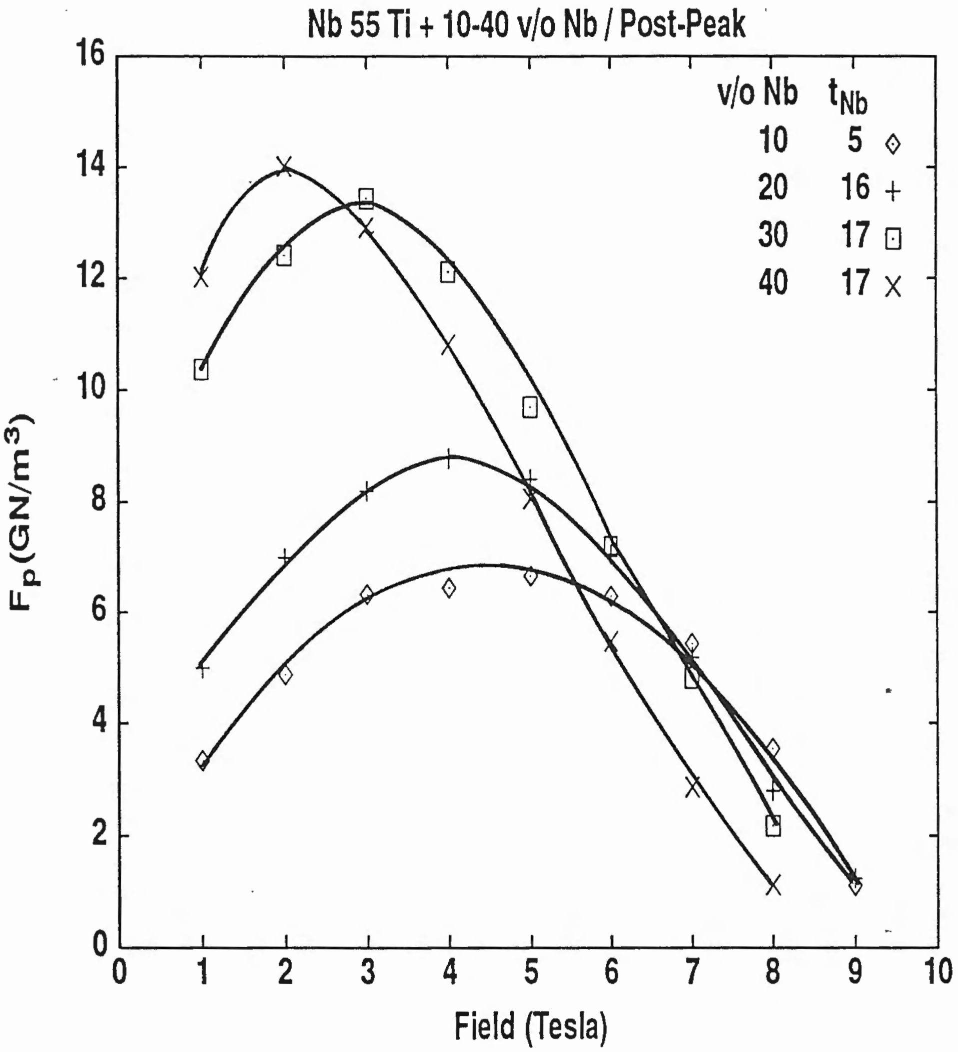

Figure 6.32: $F_p(B)$ for the various conductors when t_{Nb}~5-15nm.

Nb conductors, F_p increases at all fields and $F_{p_{max}}$ moves only from ~1T to ~2T with refinement of t_{Nb} to 28nm (30vol%Nb) and 23nm (40vol%Nb), see Figures 6.35 and 6.36. Further refinement of t_{Nb} only shifts $F_{p_{max}}$ slightly, if at all, while F_p falls off at low fields in these high volume percent Nb conductors.

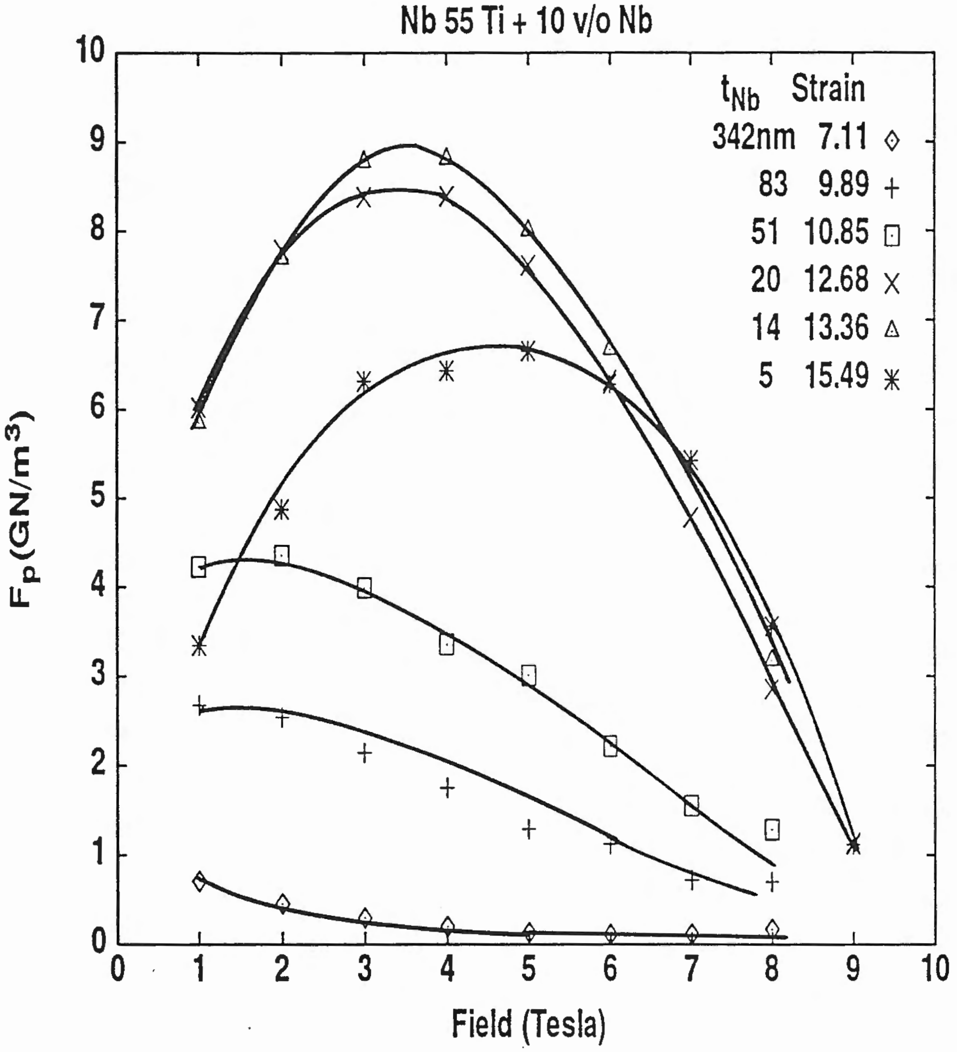

Figure 6.33: F_p vs. B for the 10vol%Nb conductor at various stages of Nb thickness refinement.

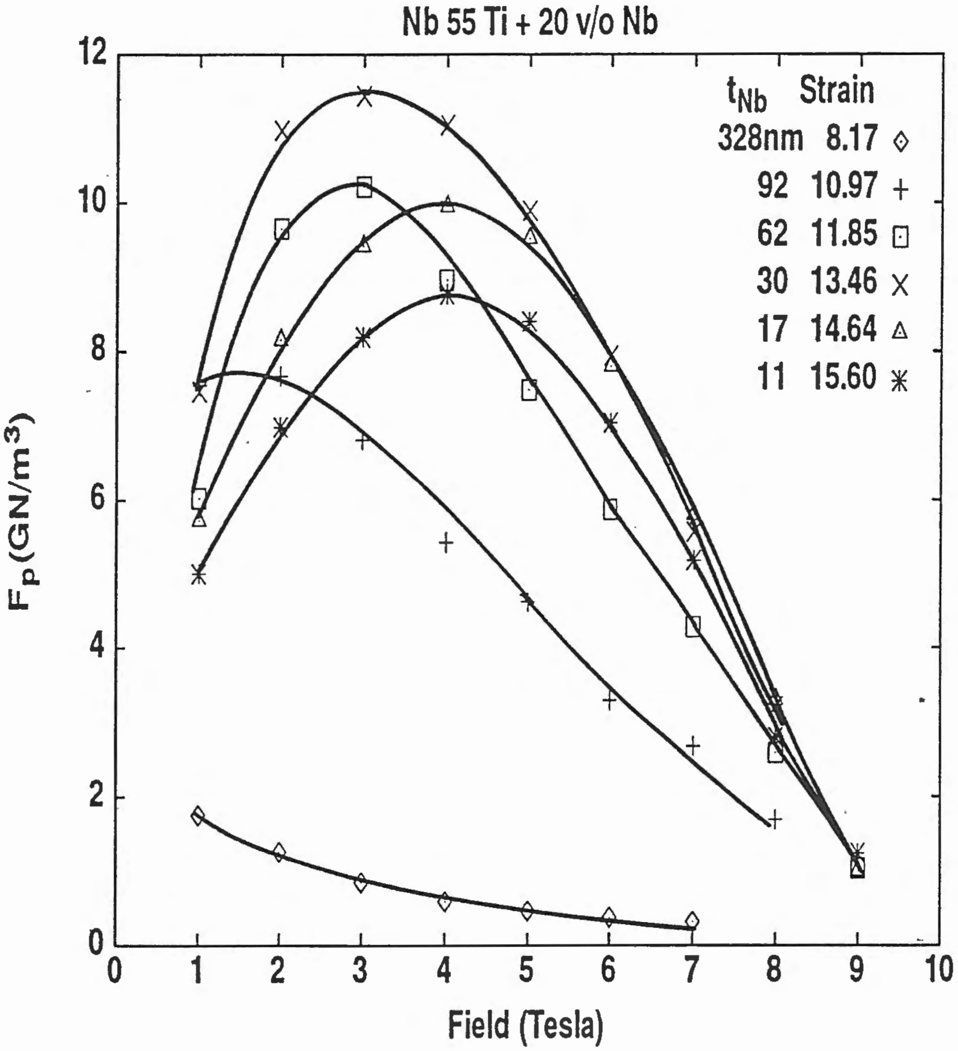

Figure 6.34: F_p vs. B for the 20vol%Nb conductor at various stages of Nb thickness refinement.

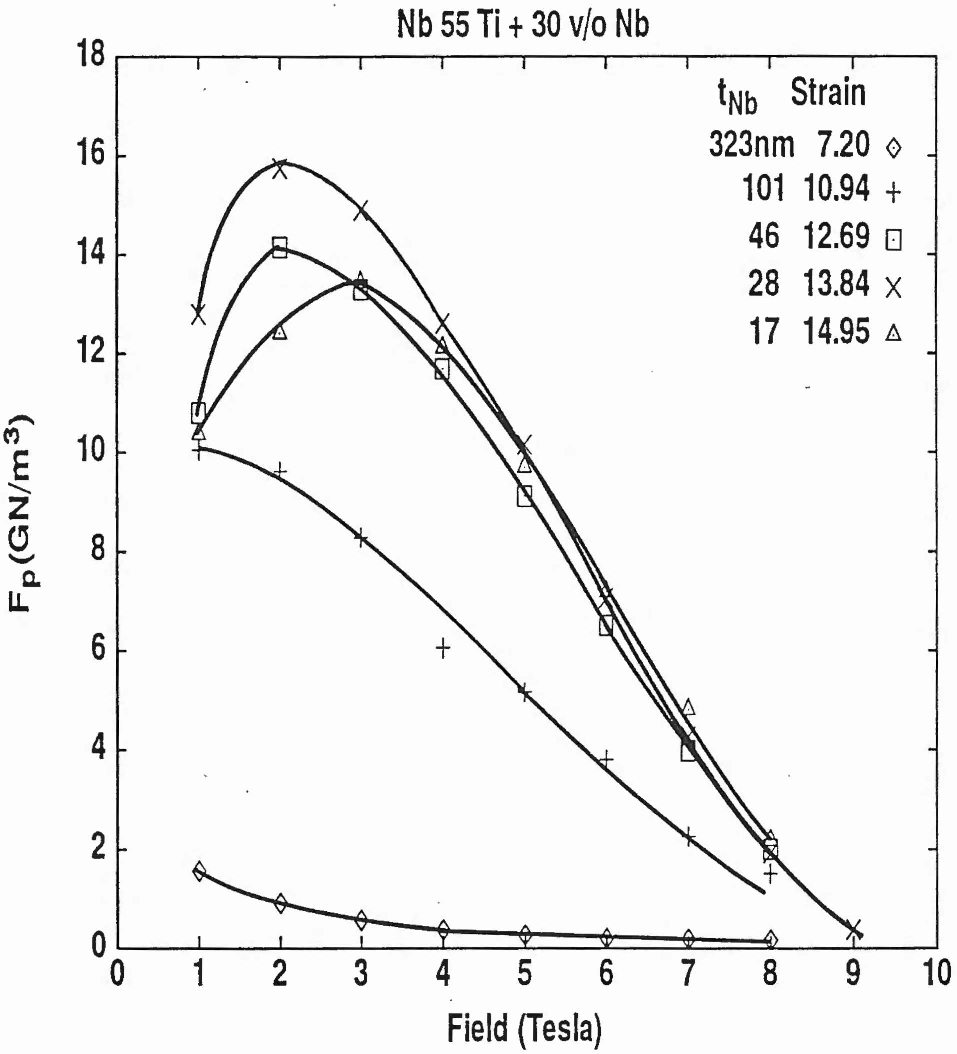

Figure 6.35: F_p vs. B for the 30vol%Nb conductor at various stages of Nb thickness refinement.

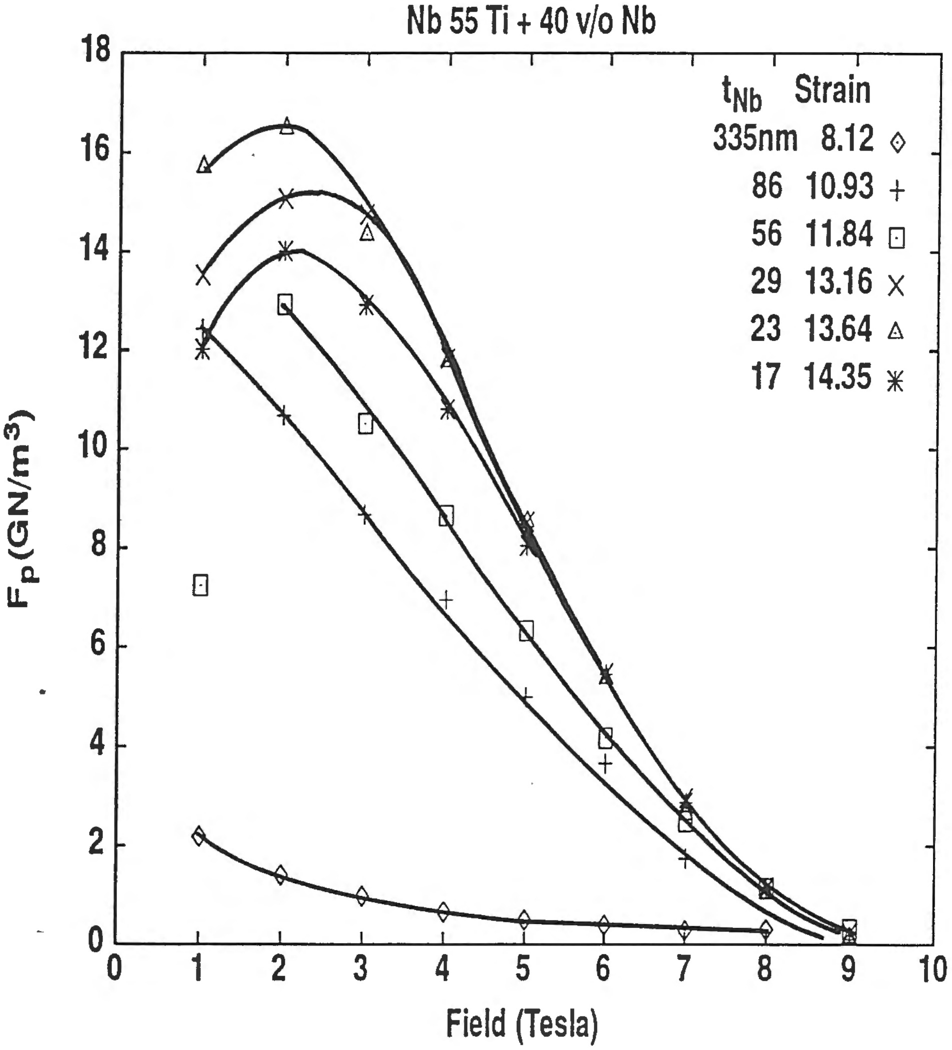

Figure 6.36: F_p vs. B for the 40vol%Nb conductor at various stages of Nb thickness refinement.

6.3 Discussion

In the preceding chapters, we discussed the process developments which permitted the fabrication of two-phase powder composites to the nanometer scale through a strain of up to ~16. This is well beyond the strain applied to *any* earlier powder composites[10, 27, 29, 51]. In Chapter 5 we discussed in detail the microstructure and property development of a 20vol%Nb conductor. We found that the low field critical current densities were substantially better than the best conventional Nb-Ti. However, the high field properties were not as good. We concluded that the flux pinning properties of the composite were largely determined by its broad distribution in t_{Nb} which meant that no one wire diameter at which there would be an optimum match between vortices and pinning centers. In this chapter we discuss a second issue of importance, namely how the flux pinning properties vary with volume fraction of pinning center.

6.3.1 Interstitial Oxygen Content and Fabricability Issues

One question of great potential concern was whether the higher than normal interstitial content of the Nb-Ti and Nb powders would lead to wire breaks at strains well below that needed to produce the desired nanostructure. As is the case for Nb-Ti alloys, oxygen was the dominant impurity. The starting powders were no different, the PREP Nb-55wt%Ti having an oxygen content of 1120ppm, while the HGD Nb powder had an oxygen content of 670ppm (Table 6.3). For Nb-47wt%Ti destined for superconductor use, the maximum oxygen content is 600ppm, while Nb-55wt%Ti used for airplane rivet applications has the higher permitted oxygen content of 1000ppm.

Assuming simple mixing would lead to oxygen contents of 1075, 1030, 985, and 940ppm in the four composites. To check for additional contamination introduced by our billet pressing, extrusion, heat treatment and other handling steps, we performed[a] interstitial chemical analysis on sections of the bundled filament assemblies at a strain of $\sim$8 (i.e., more than halfway through the fabrication). Oxygen was the dominant impurity, varying from 1430ppm (10vol%Nb)to 1060-1180ppm (20-40vol%Nb), as shown in Table 6.5. The analyzed values are indeed little greater than that expected from the initial mixtures. Although these values fall outside the limits of ingot Nb-Ti manufacture, they are not greatly higher. In any case we were able to fabricate all the composites to wire diameters as small as 80μm with Nb particle thickness of ¡10nm. Thus, while we were initially concerned that the powder APC route might not be viable due to the inherently high reactivity of the starting powders, these results clearly show that the processing precau-

---

[a] Analyses were performed at Teledyne Wah Chang.

tions outlined in Chapter 2 effectively minimized interstitial contamination and ultimately resulted in fabricable composites.

6.3.2 Microstructure

Refinement of the Nb pinning centers to thicknesses below 50nm was critical to optimizing J_c. Figure 6.37 plots t_{Nb} vs. vol% Nb at the peak J_c(5T). We found that the peak J_c was reached at t_{Nb} values of 13nm (10vol%-Nb), 30nm (20vol%Nb), 28nm (30vol%Nb) and 23nm (40vol%Nb). The t_{Nb} $+/-2\sigma$ size range was smallest for the 10vol%Nb conductor (~11-18nm), while being largest (13-58nm) for the 20vol%Nb conductor. These trends were established at larger sizes (Figures 6.5 through 6.8), as was the apparent tendency of the t_{Nb} $+/-2\sigma$ distribution to narrow at larger strains. This effect is greatest for the 10vol%Nb conductor. The underlying cause of these trends is not completely clear at this time. One factor is certainly the effective resolution of the particular characterization technique, as was discussed in detail in Chapter 5 for the 20vol%Nb conductor. Since the t_{Nb} $+/-2\sigma$ values should encompass 95% of the particles, outliers which were detected by TEM (at smaller sizes) and FESEM (at larger sizes) are ineffective in flux pinning. Given a linear summation of elementary flux pinning interaction, it is entirely appropriate to focus attention on the mean of the distribution.

A second factor playing a role in broadening the distribution is that the probability of Nb-Nb particle contacts increases as the volume percent Nb does. Such contacts will produce new, larger effective Nb particles during extrusion and drawing and such Nb-Nb particle contacts will clearly tend to the $t_{Nb} +/- 2\sigma$ value. The fact that the 10vol%Nb conductor has the smallest distribution is consistent with this hypothesis. The factor of underlying importance is of course the influence which a distribution in t_{Nb} has on the superconducting properties. No previous study of APC conductors has addressed the influence of the particle size distribution on the flux pinning properties. Indeed none has characterized the microstructure in the detail that we have. We address this matter in the next section.

6.3.3 Superconducting Properties

The present work provided an opportunity to systematically study the effect of varying the volume percent of second phase on the J_c to second phase volume fractions not achievable in conventionally processed Nb-Ti. While the 1T J_c values show a monotonically increasing critical current density through additions of 40vol%Nb (Figure 6.21), there is a gradual fall off in J_c for fields greater than ~3-4T with large additions of Nb (Figures 6.24 through 6.28). This trend is summarized in Figure 6.29 and Table 6.7. We compare conventionally processed Nb-Ti having α -Ti precipitates with these PM APC conductors in Figure 6.38. In the conventional conductors, J_c at

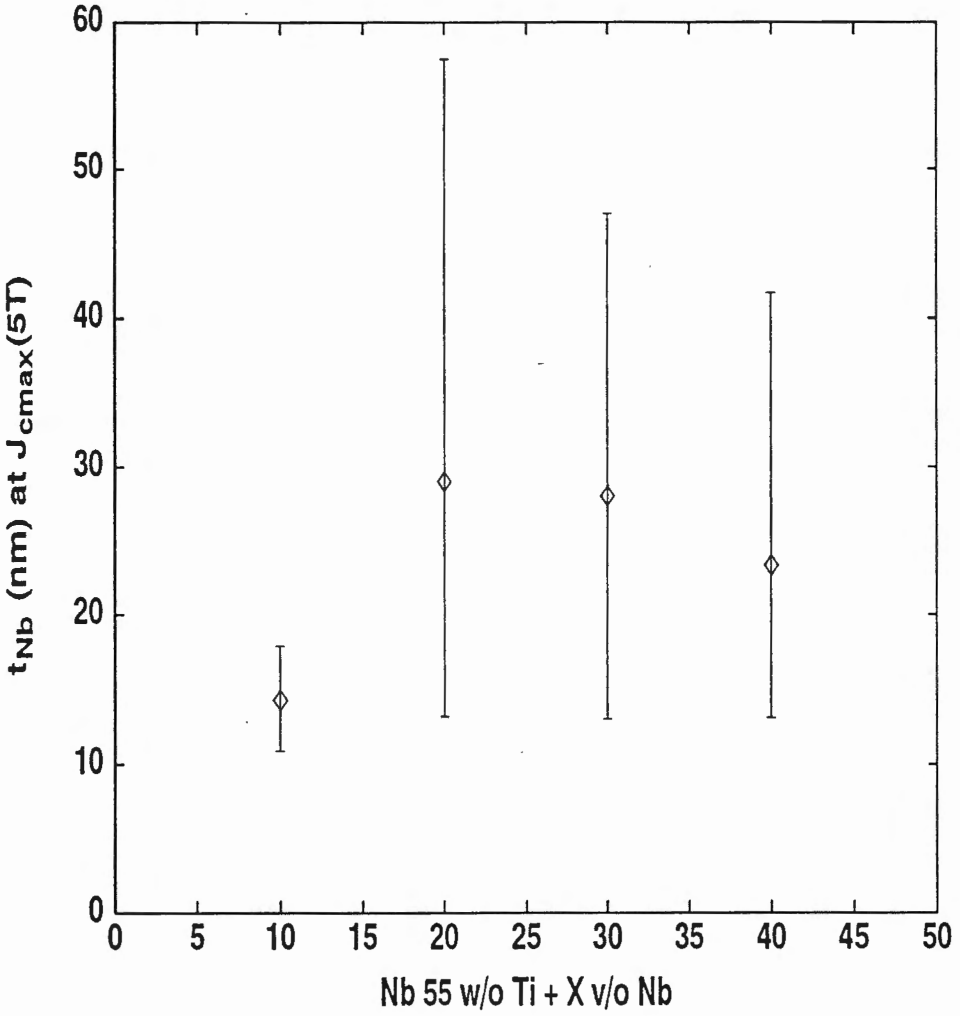

Figure 6.37: t_{Nb} vs. vol%Nb pinning center at the peak J_c(5T) size. The limits of the error bars mark the t_{Nb} +/− 2σ values.

5 and 8T increases linearly up to the maximum ~20vol%α -Ti attained. However J_c at 8T in the PM APC conductors is seen to fall for additions of more than ~10vol%Nb. J_c at both 5 and 8T is also observed to be lower than conventional Nb-Ti.

As we have shown, there is a significant increase in $J_c(B)$ for the conductors as the t_{Nb} is refined (see Figures 6.11 through 6.14). The effect is particularly strong in the strain range of 10-13 where t_{Nb} typically ranges from ~150 to 50nm as seen, for example, in Figures 6.17 through 6.20 which show J_c(5T) vs. strain. However, upon nearing the peak J_c, the slope of the J_c-ϵ curve markedly diminishes, producing a broad maximum $\Delta\epsilon$~1 wide. A similar broad maximum was observed for conventional Nb-46.5wt%Ti made from ingot by Larbalestier and West[57] (Figure 6.39). They observed that the inhomogeneous alloy had a significantly broader J_c-ϵ peak and a significantly lower maximum J_c which occurred at a smaller strain vis-a-vis the comparable high homogeneity alloy. These authors supposed that the large chemical inhomogeneity of the starting ingot (coring produced local composition variations of +/−5wt%Ti) produced a wide variation in α -Ti precipitate sizes (3 to 500nm)[119]. This range is similar to the range of t_{Nb} measured on our 20vol%Nb PM APC conductor at ϵ~12.8 (t_{Nb}~1 to 400nm). This range is large compared to that measured in high homogeneity conventional Nb-Ti at ϵ~3.9[68] ($t_{\alpha-Ti}$ ~1-12nm). Thus there is direct evidence from conven-

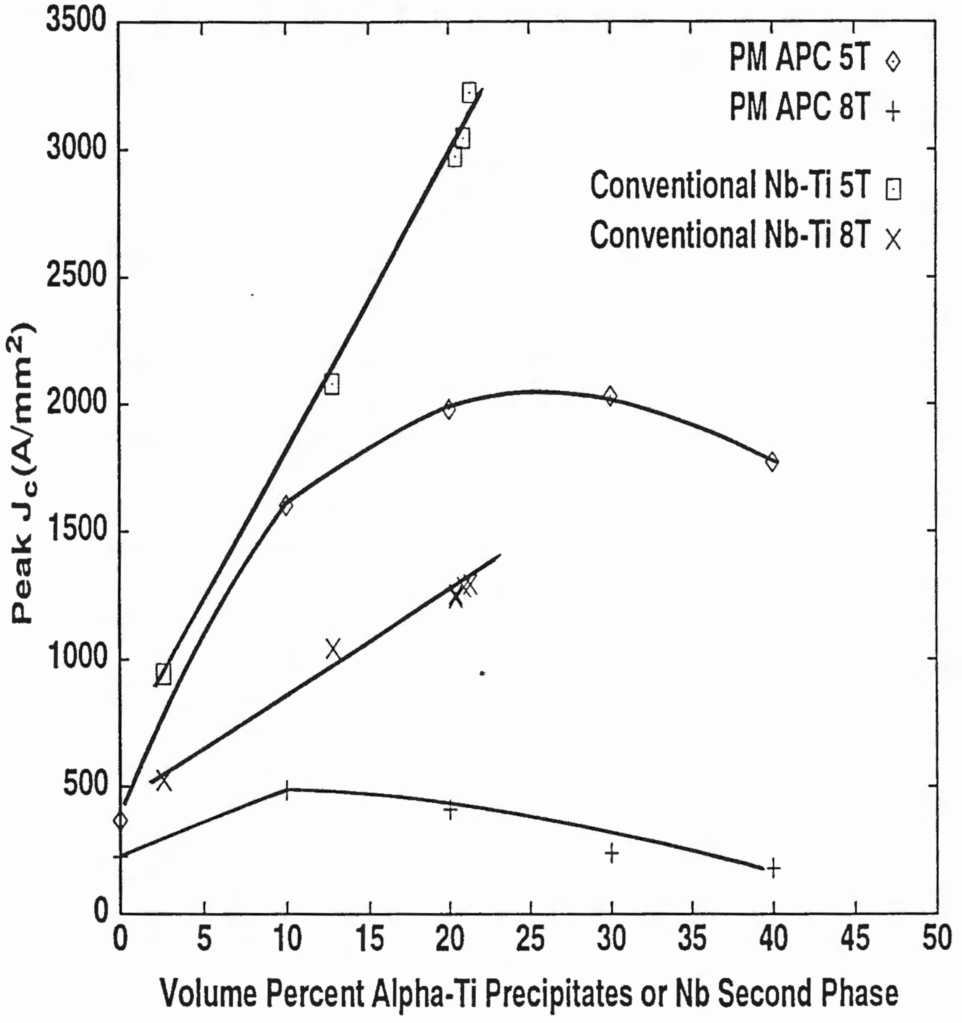

Figure 6.38: J_c vs. volume fraction of Nb (PM APC's from this study) or Ti (data from Lee et al.[66]).

tional Nb-Ti that a large range of t_{Nb} produces a broad J_c-ϵ characteristic having a diminished J_c. It is highly likely that the broad size distribution found in these billets is similarly reducing J_c below the potential values of which the microstructure is capable. In conventional Nb-Ti the difference in J_c(5T) is at least 50%, the best high homogeneity alloys achieving J_c values up to $3700A/mm^2$, while comparably optimize inhomogeneous alloys would have difficulty reaching $2000A/mm^2$. If such an increase of 1.5-1.8 were applied to the PM APC data of Figure 6.38, the 5T values of conventional and PM APC composites would be very similar. At 8T the lower B_{c_2} of the PM APC conductors renders the comparison invalid.

A second difference between conventional Nb-Ti and these PM APC conductors is demonstrated by comparing the F_p curves in Figures 6.33 through 6.36 to those in Figure 6.40. In conventional Nb-Ti Meingast et al.[84] observed that F_p increases and $F_{p_{max}}$ shifts to higher fields as the precipitates are refined. Thus the high field F_p increases but not at the expense of low field F_p. In this conductor (which is one of the best conventional Nb-Ti conductors ever made) the α -Ti ribbons were rather uniform in size ($t_{\alpha-Ti}$ $\sim$2nm) although some clustering was reported by the authors. Based on the fact that the F_p curve changed shape markedly as the temperature was raised towards T_c, it was deduced that the clusters acted as pinning centers at higher temperatures when the fluxon core diameter was comparable to the

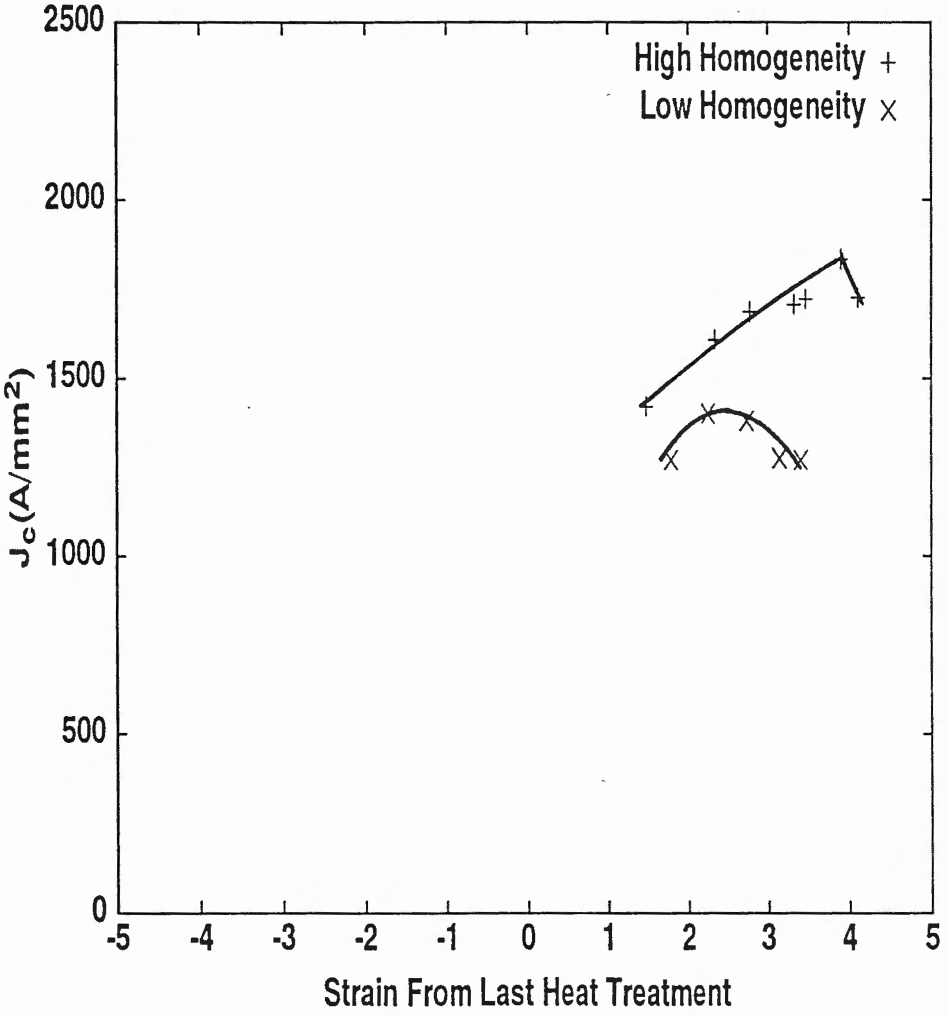

Figure 6.39: J_c vs. Strain as two conventional Nb-Ti conductors are refined, one having a broad distribution in α -Ti size (Low Homogeneity) and the other a more narrow distribution in α -Ti size (High Homogeneity). Data taken from [57].

cluster size, effectively broadening the α -Ti pinning center size distribution. This is consistent with $F_{p_{max}}$ shifting from B/B_{c_2} ~0.5 to ~0.25 at higher temperatures. This interpretation received additional support from the numerical simulations of Cooley et al.[20]. Thus both experiment and theory show $F_{p_{max}}$ shifting to lower fields with a broadening size distribution.

As seen in Figures 6.5 through 6.8 the t_{Nb} size distributions of all the conductors tend to narrow as the composites are drawn. This is reasonable since the smallest particles will eventually "refine away" mechanically alloying with the matrix. As a result, the t_{Nb} size distribution eventually becomes narrower. Thus $F_{p_{max}}$ for all the conductors should shift to higher fields at larger strains, just as is observed in Figures 6.33 through 6.36.

There were two main goals that sustained this research. The first of these was the development of a nanometer scale strong pinning two phase structure in a low strain process. After much effort, a process was developed and refined (ref. [49] and Chapters 2 through 4) which produced a two-phase strong pinning nanostructure composite in copper clad conductors within the strains of 13-14, which are characteristic of the conventional Nb-Ti fabrication process. The second goal was to explore the promising trend of increasing J_c with increasing amounts of second phase to ~20 volume percent, as shown in Figure 6.38, and extended by calculations to ~40-50 volume percent second phase by Stejic et al.[106, 107]. In this effort we were partially successful.

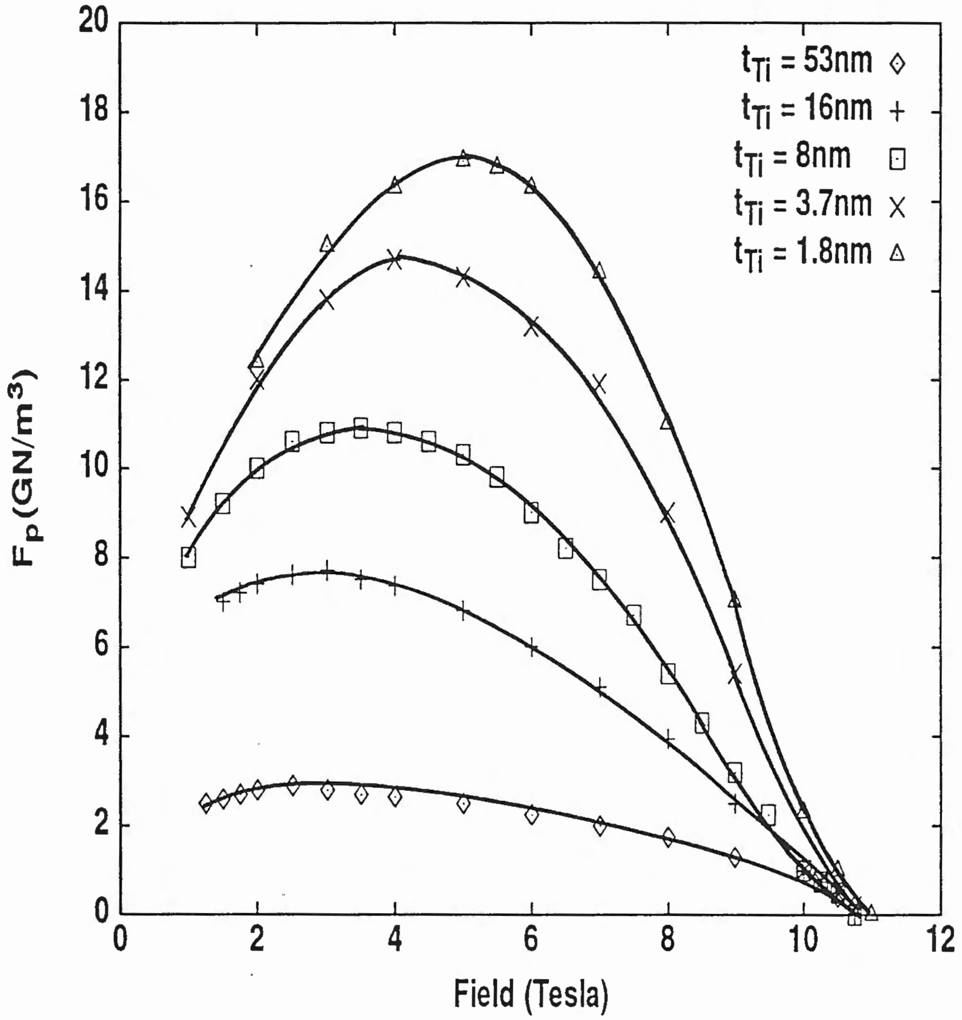

Figure 6.40: F_p vs. B for a conventional Nb-Ti conductor as the microstructure is refined (data taken from Meingast et al.[84]).

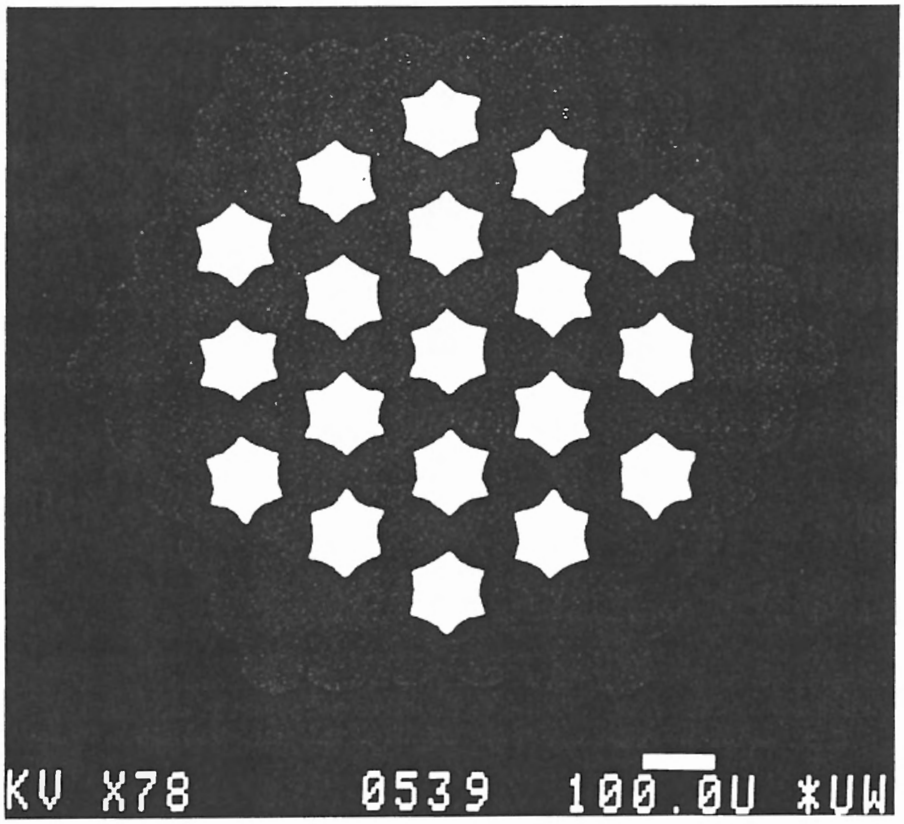

Figure 6.41: Transverse cross-section SEM backscatter micrograph showing a bundled filament superconducting composite fabricated by bundling rods of Nb-Ti (dark grey) and Nb (light) and extruding to form a two phase composite with a narrow t_{Nb}. The composite shown has about 21 volume percent second phase.

We observed monotonically increasing J_c for fields of 1-3T through 40vol%-Nb (Figures 6.21 through 6.23). This result is new. For fields higher than 3T there is a down-turn in J_c for additions of Nb of less than the maximum 40vol%. We believe that this down-turn is at least partially a consequence of the broad distribution in t_{Nb}. This may be inherent to a process which randomly distributes the second phase. We have begun experiments[39] to avoid the broad distribution in t_{Nb} by uniformly distributing the Nb second phase (Figure 6.41). However this process is not a low strain process and requires further development before the properties can be fully realized. Thus the full evaluation of the flux pinning potential of high volume fractions of second phase awaits fabrication of new more ideal composites.

6.4 Summary

A series of powder metallurgy based Nb-Ti conductors were fabricated to form nanometer scale two-phase structures within a true strain of less than 14. There are several features which indicate that a broad distribution of t_{Nb} exists at final size. First, microstructural characterization of the 20-vol%Nb conductor showed that t_{Nb} ranged from ~1 to 400nm at $\epsilon \sim 12.8$ (versus the final size $\epsilon \sim 13.5$). Second, *none* of the conductors developed the B_{c_2} of the overall composition even when deformed well past final size, in direct contrast to other APC composites. In addition, the flux pinning curves tended to be peaked at low fields at optimum size, a result which is consistent with a broad distribution in pinning center strengths. This broad t_{Nb} size distribution appeared to reduce the high field flux pinning, although it did not appear to negatively impact the low field results. Nonetheless, the critical current densities were good, especially at low fields where we observed J_c(1T) ~15,000A/mm^2 and J_c(3T) ~5000A/mm^2. The higher field values, while not record values, are quite large when taken in view of the broad range in t_{Nb} and in view of comparable conventional Nb-Ti which also had a broad distribution of pinning center sizes. The size distribution is likely due to the less than favorable combination of larger spherical, single crystal PREP Nb-55wt%Ti with the smaller angular HGD Nb powders. Further improvements in F_p (or J_c) could likely be obtained by using clean, fine grain HGD Nb-Ti and Nb powders.

Bibliography

[1] A. Abrikosov, *Soviet Physics JETP*, **5**, 1174 (1957).

[2] B. Avitzur, *Trans. ASME Eng. for Ind.*, **90**, 79 (1968).

[3] B. Avitzur and P. Blum, Modern Developments in Powder Metallurgy Volume 7, Henry H. Hausner and Walter E. Smith, ed., MPIF APMI (1973).

[4] B. Avitzur, Handbook of Metal-Forming Processes, John Wiley & Sons (1983).

[5] B. Avitzur, R. Wu, S. Talbert and Y. T. Chou, *Trans. ASME Eng. for Ind.*,-**108**, 133 (1986).

[6] B. Avitzur and W. Pachla *Trans. ASME Eng. for Ind.*, **108**, 295 (1986).

[7] B. Avitzur and W. Pachla *Trans. ASME Eng. for Ind.*, **108**, 307 (1986).

[8] J. Bardeen, L. Cooper and J. Schrieffer, *Phys. Rev.*, **108**, 1175 (1957).

[9] L. J. Barnard, *Cleaning of Metal Powders* ASM Metals Handbook Vol 7 Powder Metallurgy

[10] R. Bormann, L. Schultz, and H. C. Freyhardt, *Appl. Phys. Lett.* **32** 79 (1978).

[11] P. W. Bridgman, Physics of High Pressure, G. Bell & Sons, London (1949).

[12] A. Campbell and J. Evetts, *Adv. Phys.*, **21**, 199 (1972).

[13] R. M. Caddell and A. G. Atkins, *Trans. ASME J. Eng. Ind.*, **90**, 411 (1968).

[14] P. J. M. Chare and T. Sheppard, *Powder Met*, **16**, 437 (1973).

[15] E. W. Collings, Applied Superconductivity, Metallurgy and Physics of Titanium Alloys, Plenum Press, NY (1986).

[16] L. C. Cooley, P. D. Jablonski, P. J. Lee and D. C. Larbalestier, *Appl. Phys. Lett.*, **58**, 2984 (1991).

[17] L.D. Cooley, Ph.D. Thesis, University of Wisconsin-Madison (1993).

[18] L.D. Cooley, P.J. Lee, P. O'Leary and D.C. Larbalestier, *Appl. Phys. Lett.*, **64**, 1298 (1994).

[19] L.D. Cooley and P.D. Jablonski, Unpublished Work, University of Wisconsin-Madison (1991).

[20] L.D. Cooley, G. Stejic and D.C. Larbalestier, *Phys Rev B*, **46**, 2964 (1992).

[21] D. Dew-Hughes, *Phil. Mag.*, **30**, 293 (1974).

[22] G. E. Dieter, Mechanical Metallurgy, 3rd ed., McGraw-Hill NY, NY (1986).

[23] G. L. Dorofejev, E. Y. Klimenko, S. V. Frolov, E. V. Nikulenkov, E. I. Plashkin, N. I. Salunin and V. Y. Filkin, in Proc. of 9th Inter. Conf. on Magnet Technology, C. Marinucci and P. Weymuth, ed., 564 (1985).

[24] J. Duszczyk, *J. Mater. Shaping Technol.*, **9**, 103 (1991).

[25] H.E. Exner, *Reviews Powder Met. Phys. Ceram.,* **1**, 7 (1979).

[26] W. Fietz and W. Webb, *Phys. Rev.*, **178**, 657 (1969).

[27] R. Flükiger, R. Akihama, S. Foner, E. J. Mcniff, Jr., and B. B. Schwartz, *Appl. Phys. Lett.* **35** (1979).

[28] G. Frommeyer and G. Wassermann, *Acta Met.*, **23**, 1353 (1975).

[29] P. D. Funkenbush and T. H. Courtney, and D. G. Kubisch *Scripta Metall.* **18** 1099 (1984).

[30] R. M. German, Powder Metallurgy Science, Metal Powder Industries Federation, Princeton, New Jersey (1984).

[31] V. Ginzburg and L. Landau, *Zh. Eksperim. i Thor. Fiz.*, **20**, 1064 (1950).

[32] E. Gregory, *Cryogenics*, **27**, 290 (1987).

[33] E. Gregory, Work presented at the Nb-Ti workshop, Berkeley, CA, Feb. 1992.

[34] R. Hampshire and M. Taylor, *J. Phys. F*, **2**, 89 (1972).

[35] D. Hawksworth and D. C. Larbalestier, *Adv. Cryo. Eng.*, **26**, 429 (1980).

[36] Handbook of Chemistry and Physics – 63rd ed, CRC Press Inc, Boca Raton, FL, pp D48-51 and pp F52-60 (1983).

[37] D. Hawksworth, Ph.D. Thesis, University of Wisconsin-Madison (1981).

[38] R. W. Heussner, P. D. Jablonski, P. J. Lee and D. C. Larbalestier, *Adv. Cryo. Eng.*, **40** (1994).

[39] R. W. Heussner, P. D. Jablonski and D. C. Larbalestier, Presented at the Low Temperature Workshop, (1994).

[40] Y.E. High, P.J. Lee, J.C. McKinnell and D.C. Larbalestier, *Adv. Cryo. Eng.* (1992).

[41] H. Hillmann and K. J. Best, *IEEE Trans. Mag.*, **13**, 1568 (1977).

[42] J. H. Hollomon, *Trans. AIME,* **162**, 268 (1945).

[43] W. F. Hosford Jr., *Trans. AIME*, **12**, 12 (1964).

[44] J. K. Hulm and R. D. Blaugher, *Phys. Rev.*, **123**, 1569 (1961).

[45] P. D. Jablonski, Unpublished Research, University of Wisconsin-Madison (1989).

[46] P. D. Jablonski, Unpublished Research, University of Wisconsin-Madison (1990).

[47] P. D. Jablonski, Unpublished Research, University of Wisconsin-Madison (1991).

[48] P. D. Jablonski and L. D. Cooley, Unpublished Research, University of Wisconsin-Madison (1990).

[49] P. D. Jablonski and D. C. Larbalestier, U.S. Patent No. 5,226,947, July 13, 1993.

[50] P. D. Jablonski, P. J. Lee and D. C. Larbalestier, *Appl. Phys. Lett.* (1994).

[51] G. A. Jerman, I. E. Anderson, and J. D. Verhoven, *Met. Trans.* **24A** 35 (1993).

[52] R. W. Johnson and G. W. Rowe, *J. Inst. Met.*, **96**, 105 (1968).

[53] A. R. Kaufmann, U.S. Patent No. 3,099,041, July 30, 1963.

[54] A. R. Kaufmann, U.S. Patent No. 3,802,816, April 9, 1974.

[55] D. C. Larbalestier, Superconductor Materials Science, S. Foner and B. B. Schwartz, ed., Plenum Press, NY, 133 (1981).

[56] D.C. Larbalestier, Proposal to Dept. of Energy - High Energy Physics Division, December 1987.

[57] D. C. Larbalestier and A. West, *Acta Met.*, **32**, 1871 (1984).

[58] D. C. Larbalestier, A. West, W. Starch, W. Warnes, P. Lee, W. McDonald, P. O'Larey, K. Hemachalam, B. Zeitlen, R. Scanlan and C. Taylor, *IEEE Trans. Mag.*, **MAG21**, 269 (1985).

[59] D. C. Larbalestier, P. Lee and R. Samuel, *Adv. Cryo. Eng.*, **32**, 715 (1986).

[60] P. Lee and D. C. Larbalestier, *Acta Met.*, **35**, 2533 (1987).

[61] P. Lee and D. C. Larbalestier, *J. Mat. Sci.*, **23**, 781 (1988).

[62] P. Lee, *Proc. of EMSA 45*, 358 (1987).

[63] P. Lee, D. C. Larbalestier and J. McKinnell, *Adv. Cryo. Eng*, **34**, 967 (1988).

[64] P. Lee, J. McKinnell and D. C. Larbalestier, *IEEE Trans. Mag.*, **25**, 1918 (1989).

[65] P. Lee, J. McKinnell and D. C. Larbalestier, *Proc. Int. Sym. New Dev. in Superconductivity*, Y. Murakami, ed., 357 (1989).

[66] P. J. Lee, J. C. McKinnell and D. C. Larbalestier. *Adv. Cryo. Eng.*, **36**, 287 (1989).

[67] P. J. Lee and D. C. Larbalestier, *IEEE Trans. Appl. Sup.* **3**, 833 (1993).

[68] P. J. Lee, P. D. Jablonski and D. C. Larbalestier, Data presented at the Low Temperature Workshop, (1994).

[69] C. Li and D. C. Larbalestier, *Cryogenics*, **27**, 171 (1987).

[70] H. Liu and W. H. Warnes, *Adv In Cryo Eng, Mat.*, **38B**, 797 (1992).

[71] F. London and H. London, *Proc. Roy. Soc.* (London), **A149**, 71 (1935).

[72] J. C. Malzahn-Kampe and T. H. Courtney, *Scripta Met.*, **23**, 141 (1989).

[73] Y. Masuda and R. Wantabe, *Sintering Processing,* G. C. Kuczynski, ed., Plenum Press, New York, NY, 3 (1980).

[74] M. Mathur, M. Ashkin and D. Deis, *J. Appl. Phys.*, **45**, 3627 (1974).

[75] K. Matsumoto, Y. Tanaka, K. Yamafuji, K. Funaki, M. Iwakuma and T. Matsushita, *IEEE Trans. Appl. Super.,* **3**, 1362 (1993).

[76] K. Matsumoto, H. Takewaki, Y. Tanaka, O. Miura, K. Yamafuji, K. Funaki, M. Iwakuma and T. Matsushita, *Appl. Phys. Lett.*, **64**, 115 (1994).

[77] T. Matsushita and H. Küpfer, *J. Appl. Phys.*, **63**, 5048 (1988).

[78] J. McKinnell, P. Lee, R. Remsbottom, D. C. Larbalestier, W. McDonald and P. O'Leary, *Adv. Cryo. Eng.*, **34**, 1001 (1988).

[79] J. McKinnell, P. Lee and D. C. Larbalestier, *IEEE Trans. Mag.*, **25**, 1930 (1989).

[80] J. C. McKinnell, Ph.D. Thesis, University of Wisconsin-Madison (1990).

[81] C. Meingast, M. Daeumling, P. Lee and D. C. Larbalestier, *Appl. Phys. Lett.*, **51**, 688 (1987).

[82] C. Meingast, Ph.D. Thesis, University of Wisconsin-Madison (1988).

[83] C. Meingast, P. Lee and D. C. Larbalestier, *J. Appl. Phys.*, **66**, 5962 (1989).

[84] C. Meingast and D. C. Larbalestier, *J. Appl. Phys.*, **66**, 5971 (1989).

[85] H. F. Merrick, *Met Trans A*, **7A**, 505 (1976).

[86] D. Moffat, Ph.D. Thesis, University of Wisconsin-Madison (1986).

[87] D. Moffat and D. C. Larbalestier, *Met. Trans.*, **19A**, 1677 (1988).

[88] D. Moffat, D. C. Larbalestier, *Met. Trans.*, **19A**, 1687 (1988).

[89] H. Muller, Ph.D. Thesis, University of Wisconsin-Madison (1989).

[90] D. Neal, A. Barber, A. Woolcock and J. Gidley, *Acta Met.*, **19**, 143 (1971).

[91] R. D. Parkinson and T. Sheppard, *Powder Met*, **29**, 135 (1986).

[92] J. A. Parrell, P. J. Lee and D. C. Larbalestier, *IEEE Trans. Appl. Super.*, **3**, 734 (1993).

[93] I. Pfeiffer and H. Hillmann, *Acta Met.*, **16**, 1429 (1968).

[94] P. R. Roberts and B. L. Ferguson, *Int Mat Rev*, **63**, 62 (1991).

[95] J. Robertson, U.S. Patent No. 524,504, Aug. 14, 1894.

[96] J. C. Russ, Computer-Assisted Microscopy The Measurement and Analysis of Images, Plenum Press, NY, NY, pp175-218 (1990).

[97] S. Saito, K. Ikeda, S. Ikeda, A. Nagata and K. Noto, Proc. of 11th Inter. Conf. on Magnet Technology, (1989)

[98] J. M. Seuntjens and D. C. Larbalestier, *IEEE MAG* (1990).

[99] R. M. Scanlan, A. Lietzke, J. Royet, A. Wandesforde, C. E. Taylor, J. Wong and M. K. Rudziak, To appear in Proc. of 13th Inter. Conf. on Magnet Technology (1993).

[100] T. Sheppard and P. J. M. Chare, *Powder Met*, **15**, 17 (1972).

[101] T. Sheppard and D. Raybould, *J Inst Met*, **101**, 33 (1973).

[102] T. Sheppard and P. J. M. Chare, *Powder Met*, **18**, 1 (1975).

[103] T. Sheppard and H. McShane, *Powder Met*, **19**, 121 (1976).

[104] D. Smathers, Private Communication, February 1994.

[105] Smithells Metals Reference Book, E. A. Brandes and G. B. Brook, ed., Butterworth and Heinemann Boston Ltd (1992).

[106] G. Stejic, L. D. Cooley, R. Joynt and D. C. Larbalestier, *Supercond. Sci. Tech.*, **5**, S176 (1992).

[107] G. Stejic, Private Communication, September 1991.

[108] M.Suenaga and R. M. Ralls, *J. Appl. Phys.*, **40**, 4457 (1969).

[109] W. A. Spitzig, C. L. Trybus and F. C. Laabs, *Mat. Sci. and Eng. A*, **145**, 197 (1991).

[110] G. H. Tan and T. Sheppard, *Mat. Sci. and Techn.*, **2**, 1233 (1986).

[111] G. Taylor and J. W. Christian, *Phil. Mag.*, **15**, 873 (1967).

[112] G. Taylor and J. W. Christian, *Phil. Mag.*, **15**, 893 (1967).

[113] J. Vetrano and R. Boom, *J. Appl. Phys.*, **36**, 1179, (1965).

[114] N. Walsoe de Reca and C. Libanati, *Acta Met.*, **16**, 1297 (1968).

[115] W. H. Warnes and D. C. Larbalestier, *Cryogenics*, **26**, 643 (1986).

[116] W. H. Warnes and D. C. Larbalestier, Unpublished Research, University of Wisconsin-Madison (1986).

[117] W. Warnes, *J. Appl. Phys.*, **63**, 1651 (1988).

[118] A. West and D. C. Larbalestier, *Adv. Cryo. Eng.*, **26**, 471 (1980).

[119] A. West and D. C. Larbalestier, *Met. Trans. A*, **15A**, 843 (1984).

[120] J. Willbrand and W. Schlump, *Z. Metallkunde*, **66**, 714 (1975).

[121] J. G. Wistreich, *Proc. Inst. Mech Eng. (London)*, **169**, 654 (1955).

[122] R. N. Wright, *Wire Technology*, **4** 57 (1976).

[123] K. Yamafuji, N. Harada, Y. Mawatari, K. Funaki, T. Matsushita, K. Matsumoto, O. Miura and Y. Tanaka, *Cryogenics*, **31**, 431 (1991).

[124] B. Zeitlin, M. Walker and L. Motowidlo, U.S. Patent No. 4,803,310 (1989).

[125] J. Zhou and J. Duszczyk, *J.Mater.Shaping Technol.*, **6**, 241 (1989).

Appendix A

Second Phase Selection

Second phase selection is an important first step because of the stringent ductility requirements of the process. Another critical requirement is that processing, especially the thermal treatments, not destroy the two phase nature of the composite. Thus it is useful to briefly review the extensive summary of the Nb-M and Ti-M binary phase diagrams (where M is a metal) recently completed by Seuntjens and Larbalestier [98]. Their aim was to identify elements which might be used to produce APC microstructures by a casting technique. These investigators point out that only selected rare earth metals are both insoluble in, and form no intermetallics with, either Nb or Ti. Phase diagrams address thermodynamic equilibrium (which is easily attained in the melt because of rapid diffusion); however, they give no information on reaction kinetics which may actually mitigate thermodynamic limitations, allowing a kinetically stable structure to be formed. Thus their bleak observations may be a bit pessimistic.

The initial scoping experiments were restricted to Nb and Ti since these offered the closest overall compatibility to a Nb46.5wt%Ti matrix powder. Both elements are ductile and the principle concern then was the kinetic stability of the second phase throughout the processing (e.g., it must not alloy substantially with the matrix during heat-treatment). With this in mind, diffusion distances have been estimated using the simple expression: $x = \sqrt{Dt}$, with D taken from the data compiled by Moffat [86]. The use of this expression ignores the point contact nature of a pressed powder mass and also assumes volume diffusion. However, as will be seen, it serves well as a first approximation. For successful sintering (i.e., to bond the powders), a target diffusion distance between the matrix powders (Nb46.5wt%Ti) of at least $1\mu m$ was chosen. Calculations predict that this could be achieved by sintering Nb-46.5wt%Ti at 1000C for 1h. However, pure titanium diffused about $30\mu m$ into the matrix, thus substantial alloying could be expected from a mixture of Nb46.5wt%Ti and Ti powder particles. Indeed, this was observed in practice. It was found that the sintering temperature had to be reduced to 700C in order to prevent significant alloying of the Ti with the matrix (estimated Ti diffusion distance $\sim 4\mu m$ for 1h/700C). However, the matrix diffusion distance was estimated to be about 30nm and in fact the composite was not strong enough to be worked into wire. Pure Nb pinning centers were then considered. It was calculated that the Nb diffusion distance into the matrix was about 40nm for a 1175C/1h treatment, while the intermatrix diffusion distance was about $4\mu m$. Experiments have shown that even with multiple sintering/heat-treatments the Nb particles remain intact (a 1175C/3h sintering was used for the billets in this thesis), thus supporting the basic validity of the calculation.

Other considerations for the selection of a second phase material are the mechanical and chemical compatibility (the avoidance of brittle intermetallic formation) of the second phase with the matrix. Niobium fits these criteria well. Several other BCC elements are also likely candidates; these include W, Ta, and V. It is possible that Ti, Zr, and Hf may also be viable candidates (with the proper processing modifications). However, Nb was selected as the second phase material for the composites made for this thesis.

Appendix B

Image Analysis Results

The following is a compilation of image analysis results on the Nb-55-wt%Ti + 10-40vol%Nb conductors.

Table B.1: Image Analysis Results on the Nb-55wt%Ti + 10vol%Nb Composite.

d(mm)	vol%Nb	$t_{Nb}(\mu m)$	$t_{Nb}-2\sigma(\mu m)$	$t_{Nb}+2\sigma(\mu m)$
2.311	3.68	2.36	0.661	8.46
2.311	7.47	3.24	1.27	8.28
1.32	12.4	1.27	0.388	4.17
0.939	12.9	0.988	0.367	2.66
0.331	9.45	0.290	0.140	0.603
0.331	21.5	0.247	0.113	0.542
0.254	15.0	0.245	0.117	0.511
0.208	12.7	0.235	0.115	0.479
0.129	16.2	0.181	0.0904	0.361

Table B.2: Image Analysis Results on the Nb-55wt%Ti + 20vol%Nb Composite.

d(mm)	vol%Nb	$t_{Nb}(\mu m)$	$t_{Nb}-2\sigma(\mu m)$	$t_{Nb}+2\sigma(\mu m)$
2.413	18.8	3.32	1.183	9.31
1.293	26.9	1.771	0.843	3.72
0.9525	28.0	1.159	0.500	2.69
0.3251	28.5	0.740	0.0891	6.14
0.2516	48.9	0.238	0.215	0.704
0.2516	15.75	0.313	0.126	0.777
0.2516	35.1	0.447	0.282	0.709
0.2035	41.9	0.218	0.0965	0.494
0.1283	30.98	0.275	0.159	0.475
0.02016	20.5	0.0656	0.0343	0.140
0.02016	12.1	0.134	0.064	0.383

Table B.3: Image Analysis Results on the Nb-55wt%Ti + 30vol%Nb Composite.

d(mm)	vol%Nb	$t_{Nb}(\mu m)$	t_{Nb} $-2\sigma(\mu m)$	$t_{Nb}-2\sigma(\mu m)$
2.36	37.7	2.88	0.969	8.59
1.28	41.5	1.80	0.759	4.28
0.947	41.9	1.63	0.595	4.47
0.323	38.5	0.530	0.287	0.978
0.244	45.5	0.360	0.0867	0.918
0.161	46.9	0.290	0.114	0.740
0.125	35.1	0.242	0.125	0.468

Table B.4: Image Analysis Results on the Nb-55wt%Ti + 40vol%Nb Composite.

d(mm)	vol%Nb	$t_{Nb}(\mu m)$	$t_{Nb}-2\sigma(\mu m)$	$t_{Nb}+2\sigma(\mu m)$
2.362	48.9	3.73	0.812	17.1
1.29	44.9	1.86	0.422	8.25
0.953	52.8	2.04	0.725	5.72
1.29	49.6	1.85	0.514	6.64
0.325	51.3	0.476	0.171	1.32
0.325	62.2	0.434	0.151	1.25
0.246	45.6	0.338	0.117	0.986
0.181	40.0	0.269	0.101	0.717
0.126	45.8	0.302	0.102	0.888